



National Library
of Canada

Acquisitions and
Bibliographic Services Branch

395 Wellington Street
Ottawa, Ontario
K1A 0N4

Bibliothèque nationale
du Canada

Direction des acquisitions et
des services bibliographiques

395, rue Wellington
Ottawa (Ontario)
K1A 0N4

Your file *Votre référence*

Our file *Notre référence*

NOTICE

The quality of this microform is heavily dependent upon the quality of the original thesis submitted for microfilming. Every effort has been made to ensure the highest quality of reproduction possible.

If pages are missing, contact the university which granted the degree.

Some pages may have indistinct print especially if the original pages were typed with a poor typewriter ribbon or if the university sent us an inferior photocopy.

Reproduction in full or in part of this microform is governed by the Canadian Copyright Act, R.S.C. 1970, c. C-30, and subsequent amendments.

AVIS

La qualité de cette microforme dépend grandement de la qualité de la thèse soumise au microfilmage. Nous avons tout fait pour assurer une qualité supérieure de reproduction.

S'il manque des pages, veuillez communiquer avec l'université qui a conféré le grade.

La qualité d'impression de certaines pages peut laisser à désirer, surtout si les pages originales ont été dactylographiées à l'aide d'un ruban usé ou si l'université nous a fait parvenir une photocopie de qualité inférieure.

La reproduction, même partielle, de cette microforme est soumise à la Loi canadienne sur le droit d'auteur, SRC 1970, c. C-30, et ses amendements subséquents.

University of Alberta

Flow Liquefaction Analysis of a Slope Failure in Coal Ash Tailings

By

©Sean Taylor Reilly



A thesis submitted to the Faculty of Graduate Studies and Research

in partial fulfillment of the requirements for

the degree of Master of Science

Department of Civil Engineering

Edmonton, Alberta

Fall, 1995



National Library
of Canada

Bibliothèque nationale
du Canada

Acquisitions and
Bibliographic Services Branch

Direction des acquisitions et
des services bibliographiques

395 Wellington Street
Ottawa, Ontario
K1A 0N4

395, rue Wellington
Ottawa (Ontario)
K1A 0N4

Your file *Votre référence*

Our file *Notre référence*

THE AUTHOR HAS GRANTED AN IRREVOCABLE NON-EXCLUSIVE LICENCE ALLOWING THE NATIONAL LIBRARY OF CANADA TO REPRODUCE, LOAN, DISTRIBUTE OR SELL COPIES OF HIS/HER THESIS BY ANY MEANS AND IN ANY FORM OR FORMAT, MAKING THIS THESIS AVAILABLE TO INTERESTED PERSONS.

L'AUTEUR A ACCORDE UNE LICENCE IRREVOCABLE ET NON EXCLUSIVE PERMETTANT A LA BIBLIOTHEQUE NATIONALE DU CANADA DE REPRODUIRE, PRETER, DISTRIBUER OU VENDRE DES COPIES DE SA THESE DE QUELQUE MANIERE ET SOUS QUELQUE FORME QUE CE SOIT POUR METTRE DES EXEMPLAIRES DE CETTE THESE A LA DISPOSITION DES PERSONNE INTERESSEES.

THE AUTHOR RETAINS OWNERSHIP OF THE COPYRIGHT IN HIS/HER THESIS. NEITHER THE THESIS NOR SUBSTANTIAL EXTRACTS FROM IT MAY BE PRINTED OR OTHERWISE REPRODUCED WITHOUT HIS/HER PERMISSION.

L'AUTEUR CONSERVE LA PROPRIETE DU DROIT D'AUTEUR QUI PROTEGE SA THESE. NI LA THESE NI DES EXTRAITS SUBSTANTIELS DE CELLE-CI NE DOIVENT ETRE IMPRIMES OU AUTREMENT REPRODUITS SANS SON AUTORISATION.

ISBN 0-612-06529-4

Canada

I, _____ (hereinafter called the "purchaser")

_____ (address and telephone in full) 132 712

hereby order from Her Majesty the Queen in right of Alberta as represented by the Minister of Forestry, Lands and Wildlife (hereinafter called the "Minister") the following:

- FILM COPIES** **DIGITAL MAP DATA** **DIGITAL SURVEY DATA** **SURVEY DATA LISTING**

QUANTITY	DESCRIPTION	UNIT COST	TOTAL COST FOR UNITS
1	AS 1212 - 268	87.50	87.50
1	AS 3909 - 107	87.50	87.50
			<u>175.00</u>
			+ GST

CONDITIONS OF SALE

- The supplied data will be used solely by the purchaser for the sole purposes of reproduction in thesis and for article in technical journal to be completed by Sept 1995
- A credit line will be shown on any product(s) identified in condition 1 above which contain any of the supplied data. The credit line will clearly identify what data was supplied by the Land Information Services Division and the date it was supplied.
- In view of the dated nature of the data, it is the responsibility of the purchaser of the data: (1) to confirm with the Land Information Services Division whether later versions are available before making use of the data; and (2) if the Minister permits the purchaser to provide the data to other users, to advise users of the age and status of the data.
- Redistribution or resale of supplied data in whole or in part, is not permitted, without prior written authorization of the Minister.
- The purchaser agrees that (1) the data and each part thereof, and any formatting or presentation thereof, any storage media on which it is provided, and any communication of any kind, incidental or in relation thereto, is provided to the purchaser by the Minister and the Crown without warranty or representation as to any matter including but not limited to whether the data and storage media is correct, accurate or free from error, defect, danger, or hazard, and whether it is otherwise useful or suitable for any use the purchaser may make of it; and (2) the Crown and the Minister provide the data, any related communication and any storage media without liability to the Crown, the Minister, or their employees for any loss of any kind the purchaser may sustain for any reason
- The purchaser releases and discharges, and grants a waiver to, the Crown, the Minister and its and his employees for any and all claims, obligations, loss, actions, rights of action, and damages, (including any damages that are direct, consequential or otherwise) including any arising from any negligence of the Crown, the Minister, or its or his employees or agents that the purchaser may sustain from or in connection with the preparation of, or provision to and receipt by the purchaser of, the data or any storage media, and other activity or occurrence in respect of the data or storage media.
- (1) The purchaser further covenants and agrees that the Minister has, and shall continue to have, the absolute right, privilege and entitlement to make any such other use, disclosure to any person, application or retention, or any other handling of or dealing with the data as the Minister sees fit and in any format and storage media as the Minister sees fit, and nothing in or arising from this Agreement shall in any way limit, restrict or impinge upon the aforesaid right, privilege and entitlement of the Minister.
(2) Nothing in this Agreement shall reduce or diminish the Minister's ownership of or copyright in the data or its compilation or arrangement. Any analyses, programs, systems, software and formatting in the data or on the storage media shall be the property of the Minister

MINISTER OF FORESTRY,
LANDS AND WILDLIFE

Per: [Signature]
for Land Information Services Division

Date: May 21 1995

Purchaser: [Signature]
(Print name)

Signed: [Signature]

Print Name of signatory: [Signature]

Position: LAND INFORMATION SERVICES DIV.

Date Signed: May 21 1995

University of Alberta

Library Release Form

Name of Author: Sean Taylor Reilly

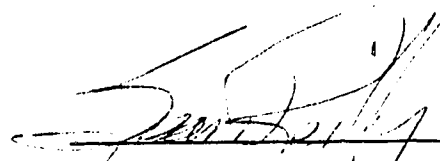
Title of Thesis: Flow Liquefaction Analysis of a Slope Failure in Coal Ash Tailings

Degree: Master of Science

Year this Degree Granted: 1995

Permission is hereby granted to the University of Alberta Library to reproduce single copies of this thesis and to lend or sell such copies for private, scholarly or scientific research purposes only.

The author reserves all other publication and other rights in association with the copyright of the thesis, and except as hereinbefore provided, neither the thesis nor any substantial portion thereof may be printed or otherwise reproduced in any material form whatever without the author's prior written permission.



Sean Taylor Reilly

60 Elmdale Boulevard
Brandon, Manitoba
R7B 1B7

Dated: July 28, 1995

University of Alberta

Faculty of Graduate Studies and Research

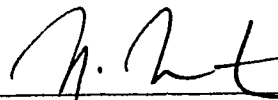
The undersigned certify that they have read, and recommend to the Faculty of Graduate Studies and Research for acceptance, a thesis entitled Flow Liquefaction Analysis of a Slope Failure in Coal Ash Tailings submitted by Sean Taylor Reilly in partial fulfillment of the requirements for the degree of Master of Science.



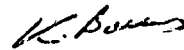
Dr. P. K. Robertson (supervisor)



Dr. D. C. Segou (co-supervisor)



Dr. N. R. Morgenstern



Dr. K. Barron

Dated: July 21, 1995

To my parents

for all their encouragement and help throughout my education.

To my friends

for all the good times we had along the way.

Abstract

In March of 1994, a slope failure, which this research presumes to be a flow liquefaction event, occurred in the coal ash tailing facility at the TransAlta Wabamun generating station. In-situ testing carried out in the ash deposits indicate the ash is a weak, highly compressible granular material that may be weakly cemented. Laboratory testing of reconstituted samples defined state boundaries and the relationship between shear wave velocity, void ratio and effective confining stress. The method described by Cunning (1994), predicts the in-situ response of the material to be strain hardening. This inconsistency with the proposed failure mechanism is discussed. As experience given in the literature with lightly cemented carbonate sands indicates that cementation can cause material to become brittle and strain softening, this report concludes there is a need for further work to understand cementation in granular materials and the possible role of cementation in the Wabamun ash deposits.

Acknowledgments

The research undertaken in the production of this thesis could not have been completed without the generous assistance of a number of individuals and companies. I would like to thank all of them for their time and effort.

I wish especially to thank Dr. Robertson for his guidance throughout this work, and for his patience in the face of my confusion and ignorance. Without his help, this work would never have reached completion. With his assistance, this has been a valuable learning experience.

I would like to recognize all the individuals in the Department of Geotechnical Engineering at the University of Alberta who assisted me in various ways. Thank you to Gerry Cyre, Barb Hofmann, Richard Stahl, Ross Corrigan and Chris Gräpel for your assistance in conducting field investigations. Thanks especially to Richard Stahl for his efforts in analyzing field data, and summarizing it in a form that was meaningful to me. Thank you to Steve Gamble, Gerry Cyre, Anajirao Chillarige and Amin Touhidi for your assistance and guidance in the laboratory. Without your guidance I might still be in the lab trying to produce meaningful results. Thank you also to Sally Petaske, Dr. Sego, and Dr. Morgenstern for your assistance along the way.

I would like to thank Dr. Joshi from the University of Calgary, and Jorma Havukainen from the Geotechnical Department of the City of Helsinki for their assistance in providing me with research materials, some of which could not be obtained from any other source.

A number of companies were involved in my research in various ways. I would like to thank Luscar for their generous financial support in the form of the Luscar scholarship. I would like to thank TransAlta Utilities for allowing me access to the Wabamun site, and for providing me with information and records for my research. I would also like to thank site contractors Fording Coal Ltd., Carl Schnell Construction and Monenco Agra Ltd. for their assistance in providing me with information. Finally, I would like to thank ConeTec Investigations Ltd. for providing much of the field equipment used in the site investigation.

Table of Contents

1. Introduction	1
1.1. Object of this Research	1
1.2. Organization of the Thesis	1
2. Site History	3
2.1. Ash Lagoon Construction	3
2.2. Description of Failure	4
2.2. Discussion of Failure	5
Figures	7
3. Background Research	11
3.1. Literature Review	11
3.1.1. Critical State Soil Mechanics (CSSM)	11
3.1.2. Evaluation of Flow Liquefaction Potential	12
3.1.3. The Nature of Coal Ash Material	13
3.1.4. Behavior of Compressible Granular Materials	15
3.1.5. Effects of Aging on Soils	17
3.2. Review of Available Site Records	18
3.2.1. Aerial Photograph Records	18
3.2.2. Review of Site Survey Data	19
3.2.3. Review of Post-Failure Video	19
Table	22
Figures	23
4. Site Investigation and Material Characterization	39
4.1. Preliminary Site review	39
4.2. Bulk Grab Sampling	40
4.3. In-Situ Sampling	41
4.4. Scanning Electron Micrographs	41
4.5. Piezometric Cone Penetrometer Testing (CPTU)	43
4.5.1. Piezometric Cone Testing Procedure	43
4.5.2. Interpretation of Cone Data	44
4.6. Spectral Analysis of Surface Wave (SASW) Testing	46
4.6.1. SASW Testing Procedure	46

4.6.2. Interpretation of SASW Data	46
Tables	48
Figures	50
5. Triaxial Testing With Shear Wave Velocity Measurement	79
5.1. Triaxial Testing Procedure	79
5.1.1. Testing Equipment	79
5.1.2. Sample Preparation	79
5.1.3. Calculation of Void Ratio	80
5.1.4. Shear Wave Velocity Measurement	81
5.2. Material Tested	82
Table	83
Figures	84
6. Test Results	88
6.1. Consolidation	88
6.2. Shear Loading Results	89
6.3. Shear Wave Velocity Measurement	90
6.3.1. Laboratory Shear Wave Velocity Measurements	92
6.3.2. Determination of $e-p'-V_s$ Relation By Extrapolation	92
Table	95
Figures	96
7. Analysis of Test Data	106
7.1. Large Strain Consolidation Results	106
7.2. Classification Based on In-situ Testing	107
7.3. Prediction of Liquefaction Potential From Laboratory and Field Testing	110
Figures	113
8. Summary and Conclusions	123
9. Suggestions for Further Research	125
Bibliography	127
Appendix A	130

List of Tables

Table 3.1: Typical Mineralogy for Coal Fly Ash. _____	22
Table 4.1: Index Properties for Bulk Samples From the Wabamun Plant and from Locations B1 through B5. _____	48
Table 4.2: Index Properties for In-situ Samples from Location 11. _____	49
Table 5.1: Index Properties for Triaxial Test Samples. _____	83
Table 6.1: Summary of Triaxial Test Data. _____	95

List of Figures

Figure 2.1: Aerial photograph overview of the Wabamun site. (Maps Alberta Airphoto #4212-208)	7
Figure 2.2: Aerial photograph of the 1977 ash lagoon with cell numbers indicated. (TransAlta Utilities)	8
Figure 2.3: Cross section of the cell 3 dike a) showing full section with relative CPT test locations indicated by triangles and b) showing the cell 3 dike with the slip surface and erosion limit indicated.	9
Figure 2.4: Slope/w analysis of the cell 3 dike for the worst case conditions immediately preceding failure. Factor of safety is for Bishops method with $\phi' = 30^\circ$, $c' = 0$ and a total unit weight of 13 kN/m^3 .	10
Figure 3.1: Schematic of the three dimensional CSSM framework for soil state, after Sasitharan (1994).	23
Figure 3.2: Definitions of the USS parameters in a) e against $\log p'$ space and b) normalized stress path space (Cunning, 1994).	24
Figure 3.3: Schematic behavior of cohesionless soil in response to loading, after Robertson (1994).	25
Figure 3.4: Void ratio against effective stress for Sacramento River sand (Lee and Seed, 1967).	26
Figure 3.5: Void ratio against effective stress for Kingfish sand and Halibut sand (Airey et al., 1988).	27
Figure 3.6: Schematic of the limiting state line for cohesionless soils (Semple, 1988).	28
Figure 3.7: Schematic of the limiting consolidation curve for cohesionless soils in a) e - $\log p'$ space, and b) $\log e$ - $\log p'$ space (Pestana and Whittle, 1995).	29
Figure 3.8: Schematic behavior of ideal and structured soils (Leroueil, 1992).	30
Figure 3.9: Plate settlement against load for a plate load test on dry quartz sand (Schmertmann, 1991).	31
Figure 3.10: The effect of aging on normalized shear wave velocity for sands (Robertson et al, 1995).	32
Figure 3.11: Classification chart to evaluate soil behavior type (Robertson et al, 1995).	33
Figure 3.12: Aerial photograph of the 1977 ash lagoon taken September 03, 1989. (Maps Alberta Airphoto #3909-107)	34
Figure 3.13: Aerial photograph of the 1977 ash lagoon taken September 25, 1991. (Maps Alberta Airphoto #4212-208)	35
Figure 3.14: Aerial photograph of the 1977 ash lagoon taken July, 1992. (TransAlta Utilities)	36

Figure 3.15: Aerial photograph of the 1977 ash lagoon taken August, 1993. (TransAlta Utilities)	37
Figure 3.16: Aerial photograph of the 1977 ash lagoon taken November, 1994. (TransAlta Utilities)	38
Figure 4.1: November, 1994 aerial photograph of the 1977 ash lagoon with sampling and testing locations indicated.	50
Figure 4.2: Grain size distributions for bulk samples taken from the Wabamun plant and from sample locations B1 through B5.	51
Figure 4.3: Grain size distributions for piston samples taken at location I1.	52
Figure 4.4: SEM photograph and qualitative mineralogy for black, vitreous and blocky sand grain. Analysis shows grain to be predominantly carbon.	53
Figure 4.5: SEM photograph and qualitative mineralogy for white, glossy sand grain. Analysis shows grain to be predominantly silica, aluminum and calcium.	54
Figure 4.6: SEM photograph and qualitative mineralogy for white, porous sand grain. Analysis shows grain to be predominantly silica, aluminum and calcium.	55
Figure 4.7: SEM photograph and qualitative mineralogy for white, blocky sand grain. Analysis shows grain to be predominantly silica.	56
Figure 4.8: SEM photograph and qualitative mineralogy of I1 @ 1.8m. Overview analysis shows material to be predominantly silica, aluminum and calcium.	57
Figure 4.9: SEM photograph and qualitative mineralogy of B2. Overview analysis shows material to be predominantly silica, aluminum and calcium.	58
Figure 4.10: SEM photograph and qualitative mineralogy of bottom ash plant feed. Material is predominantly carbon (the large grain) with silica, aluminum and calcium making up the smaller grains.	59
Figure 4.11: SEM photograph and qualitative mineralogy of fly ash plant feed. Overview analysis shows material to be predominantly silica, aluminum and calcium.	60
Figure 4.12: SEM photographs at 100 times magnification of a) I1 @ 1.8 m b) I1 @ 1.3 m c) B3 and d) B2.	61
Figure 4.13: CPT data for test location I1 showing bearing resistance, friction resistance, pore pressure and friction ratio against depth.	62
Figure 4.14: CPT data for test location I2 showing bearing resistance, friction resistance, pore pressure and friction ratio against depth.	63
Figure 4.15: CPT data for test location I3 showing bearing resistance, friction resistance, pore pressure and friction ratio against depth.	64

Figure 4.16:	CPT data for test location I4 showing bearing resistance, friction resistance, pore pressure and friction ratio against depth. _____	65
Figure 4.17:	CPT data for test location I1 showing normalized cone resistance, normalized friction ratio and pore pressure ratio against depth. _____	66
Figure 4.18:	CPT data for test location I2 showing normalized cone resistance, normalized friction ratio and pore pressure ratio against depth. _____	67
Figure 4.19:	CPT data for test location I3 showing normalized cone resistance, normalized friction ratio and pore pressure ratio against depth. _____	68
Figure 4.20:	CPT data for test location I4 showing normalized cone resistance, normalized friction ratio and pore pressure ratio against depth. _____	69
Figure 4.21:	Classification based on CPT data for test location I1 showing normalized cone resistance against normalized friction ratio and normalized cone resistance against pore pressure ratio. _____	70
Figure 4.22:	Classification based on CPT data for test location I2 showing normalized cone resistance against normalized friction ratio and normalized cone resistance against pore pressure ratio. _____	71
Figure 4.23:	Classification based on CPT data for test location I3 showing normalized cone resistance against normalized friction ratio and normalized cone resistance against pore pressure ratio. _____	72
Figure 4.24:	Classification based on CPT data for test location I4 showing normalized cone resistance against normalized friction ratio and normalized cone resistance against pore pressure ratio. _____	73
Figure 4.25:	Schematic of Spectral Analysis of Surface Waves (SASW) testing and data interpretation (Stahl, 1995b). _____	74
Figure 4.26:	SASW data for test location I1 showing Rayleigh velocity against wavelength and shear wave velocity against depth. _____	75
Figure 4.27:	SASW data for test location I2 showing Rayleigh velocity against wavelength and shear wave velocity against depth. _____	76
Figure 4.28:	SASW data for test location I3 showing Rayleigh velocity against wavelength and shear wave velocity against depth. _____	77
Figure 4.29:	SASW data for test location I4 showing Rayleigh velocity against wavelength and shear wave velocity against depth. _____	78
Figure 5.1:	Schematic diagram of triaxial testing apparatus with shear wave velocity measurement, after Cunning (1994). _____	84
Figure 5.2:	Schematic diagram of protruding bender element system in triaxial head and base, after Sasitharan (1994). _____	85
Figure 5.3:	Typical plot of laboratory shear wave during consolidation in triaxial test apparatus. _____	86

Figure 5.4:	Grain size distribution of material prepared for triaxial test program.	87
Figure 6.1:	Summary of material states in e against $\log p'$ space during consolidation and triaxial testing, showing proposed bilinear USSL.	96
Figure 6.2:	Grain size distribution of test samples following consolidation and triaxial testing.	97
Figure 6.3:	Summary of q against percent strain for all tests.	98
Figure 6.4:	Summary of pore pressure against percent strain for undrained tests.	99
Figure 6.5:	Summary of volume change against percent strain for drained test.	100
Figure 6.6:	Summary of q/p'_{uss} against p'/p'_{uss} (normalized stress space) for all tests.	101
Figure 6.7:	q_{uss} against p'_{uss} for all drained tests with best-fit line of slope M shown.	102
Figure 6.8:	Summary of normalized shear wave velocity against void ratio after Skirrow(1995).	103
Figure 6.9:	Summary of normalized shear wave velocity against void ratio with the addition of Wabamun sand, after Skirrow (1995).	104
Figure 6.10:	Contours of V_s in e against $\log p'$ space proposed by this research with the contours proposed by Skirrow (1995) and the bi-linear USSL for Wabamun sand shown for comparison.	105
Figure 7.1:	Consolidation data for Wabamun sand showing the LSL (Semple, 1988) and the LCC (Pestana and Whittle, 1995) in a) e - $\log p'$ and b) $\log e$ - $\log p'$.	113
Figure 7.2:	Summary of consolidation data for sands showing the LSL (Semple, 1988) and the LCC (Pestana and Whittle, 1995) in e - $\log p'$.	114
Figure 7.3:	Summary of consolidation data for sands showing the LSL (Semple, 1988) and the LCC (Pestana and Whittle, 1995) in $\log e$ - $\log p'$.	115
Figure 7.4:	Classification based on normalized cone resistance and normalized small strain shear modulus for in-situ test site I2 with the assumption of no crust in the analysis of SASW data.	116
Figure 7.5:	Classification based on normalized cone resistance and normalized small strain shear modulus for in-situ test site I2 with the assumption of a stiff crust in the analysis of SASW data.	117
Figure 7.6:	Classification based on normalized cone resistance and normalized friction ratio for in-situ test site I2 with the scale altered to include 93.7 % of the data points.	118
Figure 7.7:	Prediction of in-situ state based on estimated in-situ stresses for $K_0 = 0.4$ and field measured shear wave velocities for the assumption of no crust.	119
Figure 7.8:	Prediction of in-situ state based on estimated in-situ stresses for $K_0 = 1.0$ and field measured shear wave velocities for the assumption of no crust.	120

Figure 7.9: Prediction of in-situ state based on estimated in-situ stresses for $K_0 = 0.4$ and field measured shear wave velocities for the assumption of a stiff crust. 121

Figure 7.10: Prediction of in-situ state based on estimated in-situ stresses for $K_0 = 0.4$ and field measured shear wave velocities for the assumption of a stiff crust. _____ 122

List of Symbols and Abbreviations

B1 - B5	Bulk sampling locations as defined in figure 4.1
BAW	Beach material deposited above water
BBW	Beach material deposited below water
B_q	Pore pressure ratio
C_c	Compression index
CD	Consolidated drained triaxial test
CPT	Cone penetration test
CPTU	Cone penetration test with pore pressure measurement
CS	Critical state or steady state
CSSM	Critical state soil mechanics
CU	Consolidated undrained triaxial test
Δt	Travel time of shear wave
ΔV_{consol}	Calculated volume change during consolidation
$\Delta V_{\text{mem.corr.}}$	Calculated volume change due to membrane penetration
ΔV_{sat}	Calculated volume change during saturation
e	Void ratio
ϵ_a	Axial strain
e_{max}	Maximum void ratio (ASTM D4253-83)
e_{min}	Minimum void ratio (ASTM D4254-83)
ϵ_v	Volumetric strain
ϕ'	Mobilized friction angle
ϕ_{cv}	Constant volume friction angle
F_R	Normalized friction ratio
f_s	Sleeve friction measured in CPT sounding
Γ	The intercept of the USSL at $p' = 1$ kpa in $e-\ln p'$
G_0	Small strain shear modulus
G_s	Specific gravity of solids
I1 - I4	In-situ test locations as defined in figure 4.1
K_0	Ratio of horizontal effective stress to vertical effective stress
LCC	Limiting compression curve
λ_{in}	The slope of the USSL in $e-\ln p'$
LSL	Limiting state line
LSS	Limited strain softening response with ultimate strain hardening
M	$q_{\text{uss}}/p'_{\text{uss}}$
μ	Poisson's ratio
M_s	Mass of solids
p'	First invariant of the stress tensor
p'_c	Effective consolidation stress

p'_{uss}	The value of p' at ultimate steady state
q	Second invariant of the stress tensor
q_c	Cone resistance measured in CPT sounding
Q_t	Normalized cone resistance
q_t	Area corrected cone resistance
q_{uss}	The value of q at ultimate steady state
ρ	Density
ρ_b	Bulk density
ρ_w	Density of water
s	Slope of the collapse surface through the USS point
σ_1'	Major principal effective stress
σ_3'	Minor principal effective stress
SASW	Spectral analysis of surface waves
SCPT	Cone penetration test with shear wave velocity measurement
SH	Strain hardening
σ_H'	Horizontal effective stress
SS	Strain softening
σ_v'	Effective overburden stress
σ_{vo}	Total overburden stress
σ_{vo}'	Effective overburden stress
T1-T10	Test number
u	Pore pressure measured between tip and friction sleeve in CPT sounding
u_0	Equilibrium pore pressure
USS	Ultimate steady state
USSL	Ultimate steady state line
V_{init}	Volume after sample preparation
V_s	Shear wave velocity
V_{sl}	Normalized shear wave velocity
WS	Wabamun Sand

1. Introduction

1.1. Object of this Research

In March of 1994, a slope failure of a cell dike occurred in the coal ash tailings facility at the TransAlta Utilities generating station in Wabamun, Alberta. Eyewitness accounts of the failure led researchers at the University of Alberta to believe that this failure was a liquefaction flow slide. Recent work at the University of Alberta (Cunning, 1994) led to the development of a procedure for evaluating flow liquefaction potential based on in-situ testing. The failure at the Wabamun coal ash tailings lagoon presented an opportunity to apply the method proposed by Cunning (1994) to a deposit that was known to liquefy.

The method of flow liquefaction analysis proposed by Cunning (1994) makes use of field measurements of shear wave velocity combined with a program of laboratory triaxial testing with shear wave velocity measurements to predict the flow liquefaction potential of in-situ deposits. In this research, a program of field investigations including sampling and in-situ testing using cone penetrometer (CPT) and spectral analysis of surface waves (SASW) was undertaken in the summer and fall of 1994. This was combined with laboratory index and triaxial testing to characterize the Wabamun coal ash deposits with respect to flow liquefaction.

1.2. Organization of the Thesis

Chapter 2 of this thesis gives a brief history of the coal ash storage lagoons on the Wabamun site, and gives a brief outline of the failure event. Included in the outline is the eyewitness account of the failure.

Chapter 3 of this thesis summarizes the literature review, including relevant topics and available site records. Literature review included investigation of critical state soil mechanics concepts, the nature of coal ash material, the behavior of compressible granular materials, the effects of aging on soils, and the method of flow liquefaction

evaluation used in this research. Records obtained from TransAlta Utilities and other sources include aerial photographs of the ash lagoons and surrounding area, as-built survey data for cell 3 in the 1977 ash lagoon, and a copy of a video taken during a post-failure tour of the site.

Chapter 4 details the site investigation and material characterization undertaken in the summer and fall of 1994. Site investigation included bulk and in-situ sampling, CPT testing, and in-situ shear wave velocity measurement using SASW.

Chapter 5 outlines the program of triaxial testing with shear wave velocity measurement.

Chapter 6 details the results of the triaxial test program. Ultimate steady state parameters were determined, and a relationship between void ratio, effective stress and shear wave velocity proposed for this material.

Chapter 7 discusses the analysis of the test results. This analysis includes large strain consolidation characteristics of the coal ash, the classification of the soil based on the in-situ testing program, and the prediction of liquefaction potential for the ash deposits based on the laboratory and field testing.

Chapter 8 presents a summary and conclusion for the work.

Chapter 9 proposes further research into the behavior of coal ash.

Appendix A gives a detailed description of sample preparation for triaxial testing.

2. Site History

The TransAlta Utilities Wabamun Generating Station is located approximately 70 km west of Edmonton. The facility consists of the Whitewood open pit coal mine, the Wabamun Plant, and four ash disposal lagoons. Figure 2.1 shows an aerial view of the site taken in September of 1991. The Wabamun Plant is a 4 unit, 590 MWe coal fired electric generating station that burns pulverized sub-bituminous and bituminous coal from the Whitewood mine. As a byproduct it produces coal ash as bottom ash and fly ash. Bottom ash, the portion of the burned coal that falls to the floor of the power units, has traditionally had no commercial value and is therefore disposed of on site by slurry pumping to ash tailings lagoons. Fly ash, which is collected by scrubbers in the chimneys is either sold as a concrete additive, or when supply exceeds demand, disposed of by trucking back to the mine or by mixing with the slurry feed to the ash lagoons.

Statistics compiled by the International Energy Agency Coal Research Project for 1992 (Maude et al., 1994) indicate that the four burner units at the Wabamun plant consume 2.61 million tons per year of coal with an average ash content of 17.3% by weight. This corresponds to an annual ash production of 451,530 tons. Given that bottom ash represents about 20 to 30 percent of the total ash (Joshi, 1981) and has an average dry density of 13.5 kN/m^3 at 95 % proctor (Geotechnical Department of Helsinki, 1983), annual production of bottom ash is in the order of $100,000 \text{ m}^3$.

2.1. Ash Lagoon Construction

The Wabamun site contains four ash disposal lagoons -- the fully reclaimed East Ash Lagoons, the inactive West Ash Lagoon, the dormant 1971 Ash Lagoon, and the presently active 1977 Ash Lagoon. The Lagoons consist of engineered retaining dikes ranging in height from a few meters up to approximately 15m. Operation of the lagoons originally consisted of feeding the ash slurry into the ponds from a single discharge point, with the pond water elevation kept constant, until the ponds were filled to capacity.

These ash lagoons were intended to have sufficient capacity to store all the ash produced until the projected closure of the plant in the year 2003 (Maude et al., 1994). However, since the late 1980's, the combined demands of diminishing storage space and increased environmental concern brought about the improvement of the ash lagoon system by the implementation of cell construction. This would serve to increase both ash storage capacity and decant water retention time in the system. In total three cells were constructed on top of the existing beach in the 1977 Ash Lagoon. Figure 2.2 shows an enlargement of the August, 1993 aerial view with the 1977 Ash Lagoon cells identified. Cell walls were constructed of random borrow material from the original ash deposits, placed in lifts and compacted by scrapers and bulldozers. Most of the cell walls were constructed of ash beach deposits placed above water (Beach Above Water, or BAW) material and founded on BAW. However, the west wall of cell 3 was constructed along the waterline of the existing beach, and may overlap in some locations onto ash deposited below water (Beach Below Water, or BBW). Cells were lined with minus 75 mm (-3") gravel as an erosion control measure, and the same material was used to cap the roadway on top of the cell walls. No erosion control measures were considered necessary for the downstream face of the cell walls. Operation of the ash cells was similar to that of the ash lagoons, with slurry being fed into the ponds while the decant water level was held constant.

Increasing environmental demands require that producers of coal waste material must pursue new uses of power plant ash. By implementing the construction of ash cells on the BAW slope, one new stage of pond operation could be implemented. After the ash cells are full and the material has fully drained, the ash can be removed from the cells by truck and loader and sold. Market uses for the material include aggregate for subbase course, aggregate in bitumen, underdrain material, and lightweight concrete aggregate (Tripodi and Cheremisinoff, 1980).

2.2. Description of Failure

In Mid-March of 1994, during a routine night shift inspection of the 1977 ash lagoon cells, it was noted that water was overtopping the dike midway along the west

wall of cell 3. An equipment operator was called to the area to attempt remedial work, and the following account of the failure is based on his description.

On arrival, the contractor noted that water was flowing over the dike in a stream about one meter wide and less than a 30 centimeters deep. While the road bed was sufficient to stop downcutting by the water, he noted significant erosion of the unprotected downstream toe of the dike. He immediately instructed his assistant to get a front end loader and attempt to find material competent enough to stop the overflow. Meanwhile he went to the plant to try to get the slurry feed to the cell stopped, and to get a truckload of coarse material brought to the dike. He then returned with a D-6 cat to assist in trying to stop the erosion. By this time, he estimated that as much as one third of the dike width at the toe of the dike had been eroded away. At no time did the toe erosion encroach back to the top of the dike. He could not provide a reliable estimate of the length of dike affected by the erosion. Before any significant remedial work could be done, he felt the ground shift, and immediately moved back from the area. As he was doing so, the eroded section of dike failed and flowed away. This was followed over the course of a few minutes by sections of dike on either side of the failure 'opening like floodgates' until some 275 m of dike had flowed up to 75 m out into the lagoon. The resulting wave in the lagoon cleared almost all the ice off the lagoon, and downed a nearby powerline.

It is unclear from this account exactly why the dike was overtopped. It is possible that the decant pipe was dammed by ice, and that the pond subsequently overfilled. It is also possible that excessive settlement may have occurred in a section of the dike resulting in a loss of freeboard. While one employee of TransAlta utilities stated that there had been previous problems with excessive settlement in the west wall of cell 3, this could not be reliably confirmed.

2.3. Discussion of Failure

Figure 2.3a shows a cross section through cell 3 and the 1977 ash lagoon. This section makes use of site survey data (section 3.2.2) and observations made on site of the

BAW and BBW slopes (section 4.1). Figure 2.3b shows an enlargement of the cell 3 dike, along with the erosion limit described in the eyewitness account (section 2.2) and the failure surface inferred from the site video (section 3.2.3).

Figure 2.3 leads to the inference of two possible mechanisms for the failure. In one possible mechanism, the toe erosion reduced support of the dike, water pressure behind the dike overcame frictional resistance along the failure surface, and the dike was pushed out. Figure 2.4 shows a Slope/W slope stability analysis for this case. The material was assigned a total unit weight of 13 kN/m^3 , a ϕ of 30° and no cohesion, and the specified slip surface analysed using Bishop's method. The cross section represents the condition of the eroded portion of the dike at the time the failure occurred. This analysis gives a factor of safety for this type of failure as 2.474, which strongly suggests that this mechanism was not responsible for the failure.

The second mechanism considered is a liquefaction failure. In this mechanism, the toe erosion caused an increase in shear stresses along the failure surface, triggering liquefaction of the soil and the failure of the dike. This is the mechanism that this thesis attempts to analyse.

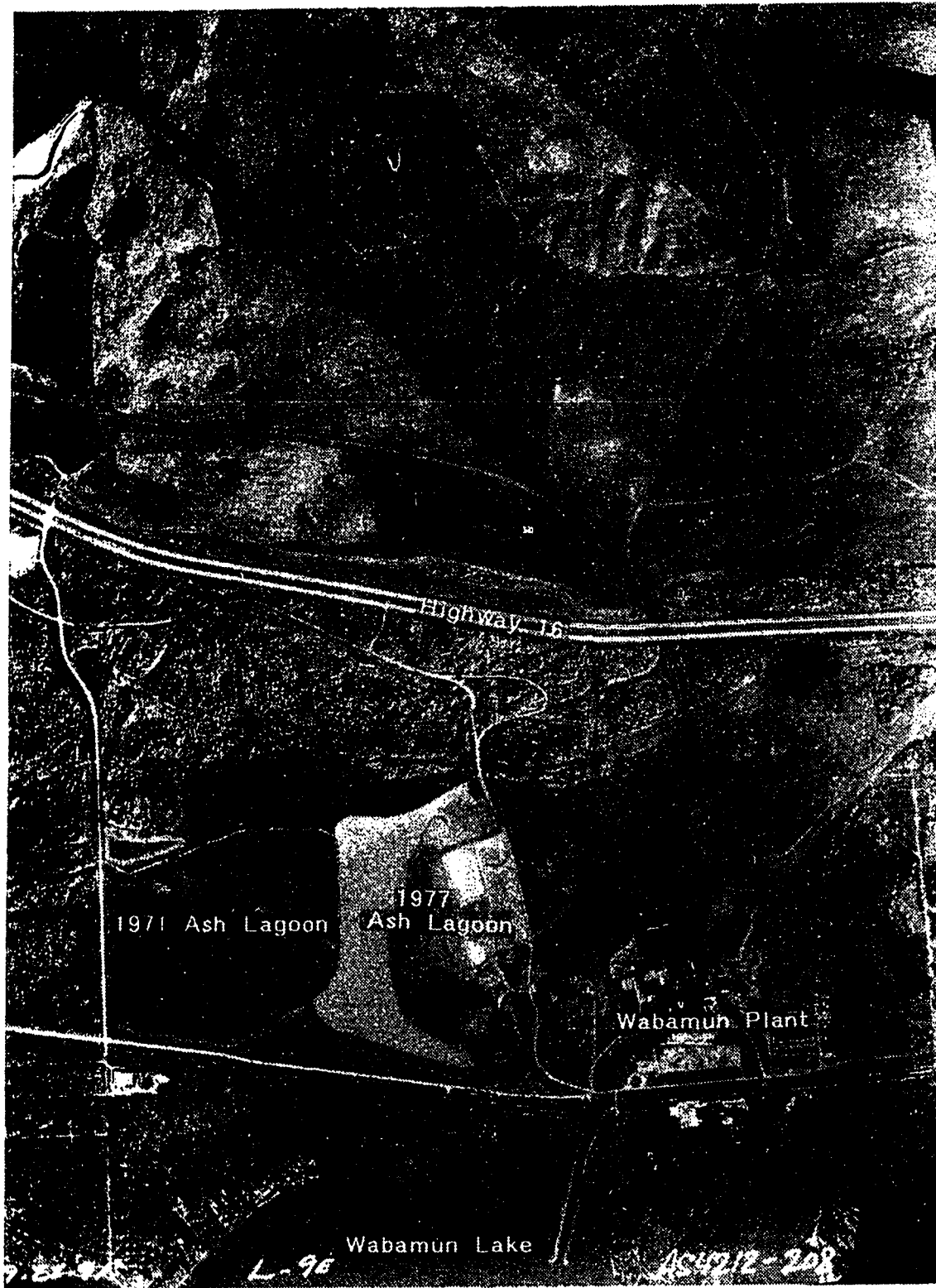


Figure 2.1: Aerial photograph overview of the Wabamun site. (Maps Alberta Airphoto #4212-208)

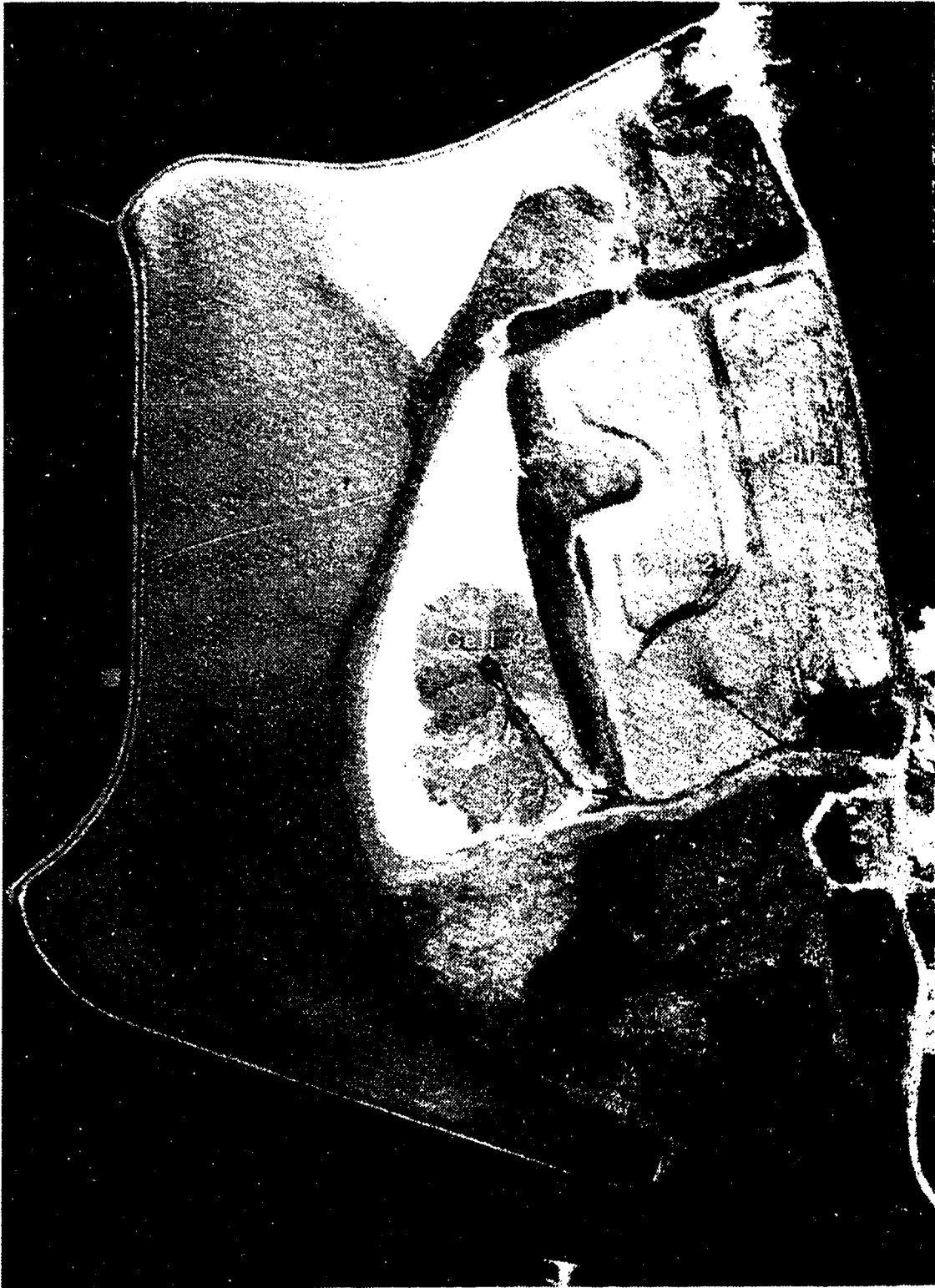


Figure 2.2: Aerial photograph of the 1977 ash lagoon with cell numbers indicated. (TransAlta Utilities)

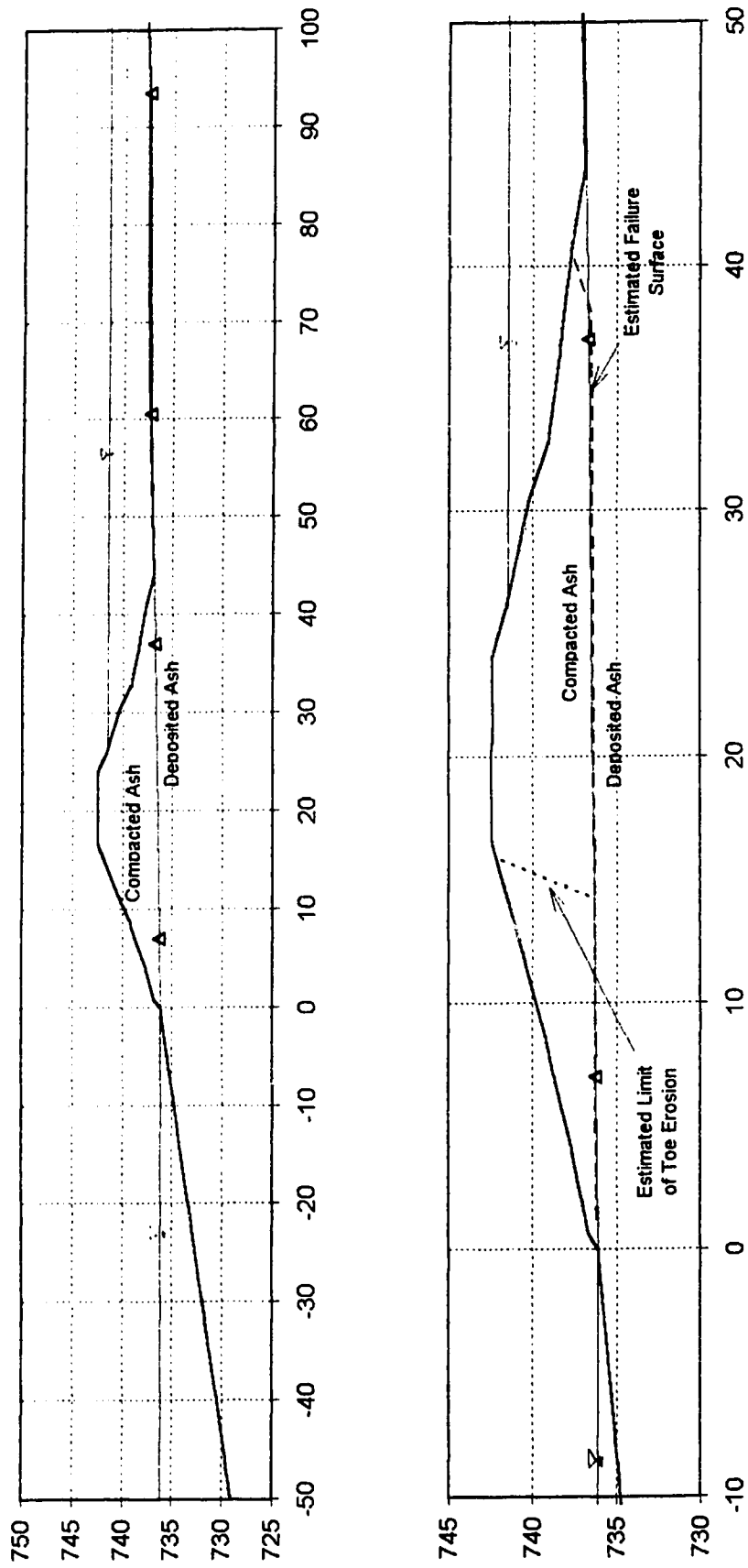


Figure 2.3: Cross section of the cell 3 dike a) showing full section with relative CPT test locations indicated by triangles and b) showing the cell 3 dike with the slip surface and erosion limit indicated.

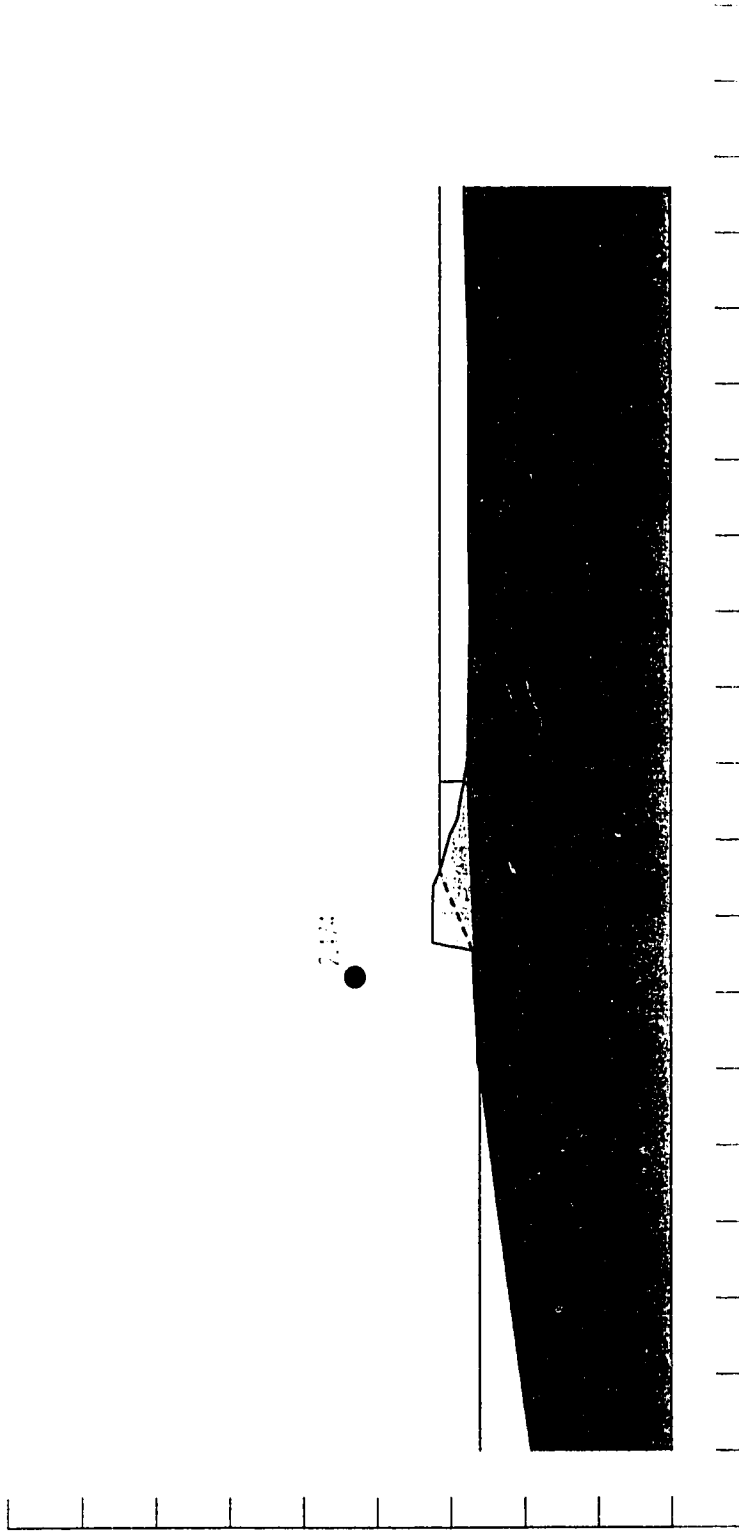


Figure 2.4: Slope/w analysis of the cell 3 dike for the worst case conditions immediately preceding failure. Factor of safety is for Bishops method with $\phi' = 30'$, $c' = 0$ and a total unit weight of 13 kN/m^3 .

3. Background Research

3.1. Literature Review

Literature reviewed included investigation of critical state soil mechanics concepts, the nature of coal ash material, the behavior of compressible granular materials, and the effects of aging on soils.

3.1.1. Critical State Soil Mechanics (CSSM)

CSSM will be used as a framework to describe the results of the triaxial testing program, and to model the cohesionless soils investigated. CSSM states that a soil exists in a void ratio and stress state such that it is either loose or dense of critical or steady state (CS). We can define in void ratio (e), mean normal effective stress (p') and deviator stress (q) space boundaries that separate states in which a soil can exist from those at which they cannot. These are referred to as state boundaries. We can also define in the same space an ultimate steady state line (USSL) toward which soil conditions will ultimately move under conditions of shear loading. Finally, Sasitharan (1994) defined a collapse surface in this space which describes a triggering condition for collapse, regardless of stress path. Figure 3.1 shows a schematic plot of this general three dimensional space. For the triaxial tests described here, the following definitions will apply:

$$p' = \frac{\sigma_1' + (2\sigma_3')}{3} \quad [1]$$

$$q = (\sigma_1' - \sigma_3') \quad [2]$$

where: σ_1' = Major principal effective stress
 σ_3' = Minor principal effective stress
 p' = First invariant of the stress tensor
 q = Second invariant of the stress tensor

This three dimensional space is often displayed on two planes, as shown in figure 3.2. Figure 3.2a shows the e versus $\log p'$ plane, used to show consolidation data and the USSL. Figure 3.2b shows the normalized stress path plane q/p'_{uss} versus p'/p'_{uss} . This normalization, described by Sladen and Oswell (1989) removes the effect of void ratio, allowing the USSL to be seen as a point and the collapse surface as a line.

Figure 3.2 also defines the CSSM parameters for describing a soil. If the USSL is assumed to be a straight line in e - $\log p'$ space over a specified stress range, the following parameters can be used:

- Γ = The intercept of the USSL at $p' = 1$ kPa in e versus $\ln p'$
- λ_{ln} = The slope of the USSL in e versus $\ln p'$
- M = q_{uss}/p'_{uss}
- s = Slope of the collapse surface in the stress path plot through the USS point (Sasitharan, 1994)

The parameter M is further defined as the slope of the constant volume friction angle line (ϕ_{cv} line). In the plot of q/p'_{uss} versus p'/p'_{uss} , figure 3.2b, this line passes from the origin through the USS point. The parameter M is further related to the mobilized friction angle ϕ by the equation:

$$M = \frac{6 \sin(\phi')}{3 - \sin(\phi')} \quad [3]$$

Within this framework, Robertson (1994) defines the behavior of individual triaxial tests as strain softening (SS), strain hardening (SH) or limited strain softening (LSS). These terms are defined in terms of q versus p' and q versus shear strain space in figure 3.3.

3.1.2. Evaluation of Flow Liquefaction Potential

Cunning (1994) suggested a procedure for evaluating the potential for flow liquefaction based on the laboratory determined e - p' - V_s relationship and USS parameters and field measured values of shear wave velocity (V_s) against depth. The depth can be

converted into vertical effective stress (σ_v') using the bulk density of the soil and the depth of the water table. Vertical effective stress can then be converted to p' according to:

$$p' = \frac{\sigma_v'}{3} (1 + 2K_0) \quad [4]$$

where: K_0 = The ratio of horizontal effective stress to vertical effective stress

These data points of coordinates V_s and p' can be plotted along contours of V_s in e - p' space. The USSL can also be plotted in e - p' space.

The location of the in-situ V_s points relative to the USSL gives an estimate of the large strain behavior of the material. Data points which plot above the boundary have the potential for flow liquefaction if the material is strain softening. The potential for strain softening must be determined in the laboratory using samples of the material consolidated to similar values of p' and V_s . Data points which fall below the USSL should exhibit a dilative response, and the potential for flow liquefaction does not exist. The problem of cyclic liquefaction under cyclic loading may still exist, and should be investigated by other methods (Robertson et al., 1992).

3.1.3. The Nature of Coal Ash Material

Coal ash forms due to the presence of non-combustible mineral constituents in the coal. Specifically, it is the residue of these mineral constituents after they have been heat treated in the coal furnace (Joshi, 1981). The Geotechnical Department of Helsinki (1983) describes three main types of coal ash:

- I Fly ash: The portion of ash which is separated and recovered from flue gasses. This is subdivided according to the type of furnace:
 - Ia - Fly ash from a power plant burning pulverized coal. This accounts for 70% to 90% of the total weight of ash. It is light gray to blackish gray in color, and of silt size. It will generally harden when compressed using a suitable amount of water.

- Ib - Fly ash from a power plant burning crushed coal. This accounts for less than half the total weight of ash produced. It is most often black in color, and of fine sand size. It does not harden when compressed, but rather behaves similarly to a sand of corresponding grain size.

- II Bottom ash: The portion which is collected from the bottom of a pulverized coal furnace. It accounts for 10% to 30% of the total weight of ash. It is light gray to brownish to blackish gray in color, and of medium coarse to coarse sand in size. Grains can be either jagged with a porous surface, or sintered with a vitreous surface. Fine portions will contain fly ash particles to some extent.

- III Bottom Slag: The portion which is collected from the bottom of a crushed coal furnace. It accounts for greater than half of the total weight of ash produced. It is dark brown to blackish gray in color, and of fine to medium-coarse gravel in size. Grains can be either jagged with a porous surface, or sintered with a vitreous surface. Its behavior is similar to an aggregate of corresponding grain size.

Joshi (1981) describes the formation of ash within a suspension fired furnace. A typical Alberta coal contains waste that is about 60% clay in the form of kaolinite or montmorillonite, 15% to 20% pyrite and calcite, and up to 5% trace minerals. These minerals melt in the flame zone in the furnace, and as a result undergo physical and chemical changes in the presence of excess air. Pyrite forms iron oxides, clay forms glass spheres of complex silicates as well as some quartz, and calcite forms calcium oxide, calcium hydroxide, calcium silicate and calcium sulfate. Gasses may be trapped in the particles, giving rise to cenospheres. The exact nature of the products from this process depend in large part on the type and composition of the source coal, the gradation of the pulverized coal, and the particle retention time within the hot zone of the furnace (Joshi and Rosauer, 1973). The fly ash particles are quenched as they leave the hot zone of the furnace, producing a heterogeneous mixture of highly vitreous spherical particles, crystalline matter and unburned coal. Fly ash may be further altered by chemicals in either the collection or stabilization process. Bottom ash is produced by sintering of

particles. Sintered and molten ash particles are too heavy to be carried by the flue gasses, and fall to the bottom of the furnace.

Many studies document properties of ashes from specific sources. Due to the variation in these properties both between different sources and between different samples from the same source, Tripodi and Cheremisinoff (1980) present a range of major constituents of coal ash. This data is shown in Table 3.1. Note that this range does not distinguish between either ash type or furnace type. For comparison, analysis of the Wabamun fly ash (Joshi and Marsh, 1987) is also presented in table 3.1.

3.1.4. Behavior of Compressible Granular Materials

The porous, angular and friable nature of coal ash suggested by the Geotechnical Department of Helsinki (1983) and observed in the Wabamun ash material (section 4.2) suggests that compressible behavior similar to that of a carbonate sand may be observed.

Semple (1988) identifies three important features of carbonate soils that effect their primary engineering characteristics: highly angular and weak grains, variable cementation between particles, and variability in particle type and size distribution.

Highly angular and weak grains result in few interparticle contact points, and high intergranular contact stresses at relatively low confining stresses. According to Demars (1982) this causes grain chipping at contact points, and subsequently interparticle slippage and large volumetric strains as particles move toward a more stable alignment. With respect to the Wabamun coal ash material, the highly angular and weak nature of the grains is seen both in hand samples (sections 4.2 and 4.3) and in the scanning electron micrograph (section 4.4).

Variable cementation, related to the variation in particle type and size distribution, is common in carbonate soils. Semple (1988) suggests that this cementation can vary from essentially none to intense, creating a range of materials from individual grains to rock. Light cementation can be detrimental, as it can serve to preserve a loose, brittle structure in the soil, even under loading by subsequent deposition. Conversely, heavy cementation produces a geotechnically competent rock-like material. The presence of

cementation in the Wabamun coal ash is expected, first from the known pozzalanic nature of the material, and second from the observation of coherent response of the material (section 4.1).

Finally, carbonate materials can vary greatly in particle type and size distribution, as well as in degree of cementation. This variation means that strength, compressibility and permeability can vary erratically throughout a deposit. While the formation of the Wabamun coal ash deposits bears no resemblance to the formation of a natural carbonate sand deposit, this variability is never the less observed in the coal ash deposits. This can be attributed in part to the variability in the formation of the coal ash, as discussed earlier, and in part to the depositional environment.

Research into the compressibility of silica based sands (Terzaghi and Peck, 1948, Roberts and deSouza, 1958, Lee and Seed, 1967, and Vesic and Clough, 1968) indicate that sands are relatively incompressible at low stresses, but can exhibit considerable volume change due to grain crushing at high stresses. Figure 3.4 illustrates this behavior through confining pressure - void ratio relationships established by Lee and Seed (1967) for a silicate sand. Tests by Airey et al. (1988), summarized in Figure 3.5, show similar behavior for carbonate sands. The key difference to note is the larger initial void ratios and smaller yield stresses observed in the carbonate sands. Semple (1988) considered both of these results and noted that at large strains, the sands tend toward the same "virgin compression" line, for which the compression index (C_c) is approximately 0.5. This virgin compression line can be described as a limiting state line. He also noted that the volumetric strain for a given stress increment, the compression index at a common applied stress below the virgin compression range, and the yield stress are all a function of the initial void ratio. Based on this, he suggests that there exists a continuity of response of bioclastic and silicate soils with initial void ratio as the controlling factor. This relationship can be seen in figure 3.6. Pestana and Whittle (1995) recognized that such a relationship predicts negative void ratios at high stress levels, and modified the limiting state line to a limiting compression curve (Figure 3.7). This curve predicts a decreasing rate of change of void ratio with increasing effective stress, with void ratio

going to zero at extremely high stresses. Through the constitutive model for compressive behavior that they develop, they further propose that the limiting compression curve will be a straight line in log void ratio against log effective stress space.

3.1.5. Effects of Aging on Soils

Schmertmann (1991) in his Terzaghi lecture discusses the effects of aging on soils. He defines “pure aging” as the changes that take place within a soil involving only the passage of time, independent of external horizontal or vertical stress changes, ground water fluctuations, swelling or desiccation, cycles of freeze and thaw, biological attack, organic decay, leaching, precipitation, ground movement or chemical weathering. Leroueil (1992), schematically presented (figure 3.8) the difference in behavior between ideal soil, which has a normal consolidation line in the case of clays, or a limiting state line (figure 3.6) in the case of sands, and natural, structured soils. As an example of this effect in sand, Schmertmann (1991) details a plate bearing load test on the surface of an unaged, clean commercial sand. Figure 3.9 shows the plate settlement versus load for the test, including an 844 minute interval of rest at a load of approximately 325 lb. on the plate. Following this holding period, a distinct aging effect can be observed, similar to that described by Leroueil (1992).

Based on a comparison between predicted and measured void ratios for undisturbed samples obtained using ground freezing, Robertson et al. (1995) suggest a relationship between normalized shear wave velocity and age. This relationship, shown in figure 3.10 suggests that aging will increase normalized shear wave velocity. They further suggest modifications to the Gillespie (1988) soil behavior type chart to include the effects of both aging and cementation. This chart, shown in figure 3.11 takes into account the increase in cone resistance and small strain shear modulus (G_0) with both aging and cementation and estimates the regions where aged and cemented materials should fall. The small strain shear modulus is related to the shear wave velocity by the bulk unit weight (ρ) of the material according to:

$$G_0 = \rho(V_s^2) \quad [5]$$

3.2. Review of Available Site Records

Records obtained from TransAlta Utilities and other sources include aerial photographs of the ash lagoons and surrounding area, as-built survey data for cell 3 in the 1977 ash lagoon, and a copy of a video taken during a post-failure tour of the site.

3.2.1. Aerial Photograph Records

Five aerial photographs of the 1977 Ash Lagoon were obtained to trace the cell construction from the appearance of BAW material in the lagoon prior to September of 1989 through to the failure of cell three in March of 1994. These photographs include Maps Alberta photos 3909-107 taken September 03, 1989 and photo 4212-208 taken September 25, 1991, and TransAlta Utilities commissioned site photos taken July 1992, August 19, 1993 and November, 1994.

The September 1989 photo (Figure 3.12) shows a portion of the 1971 ash lagoon in its inactive and partially reclaimed state, and the 1977 ash lagoon with the original single discharge point and BAW slope, as well as the early stage construction of cell #1. Note that as part of the decant and water clarification process, water from the 1977 lagoon is discharged through the 1971 ash lagoon.

The September 1991 photo (figure 3.13) shows both the 1977 ash lagoon with cells 1 and 2 completed, with cell 1 inactive and awaiting reclamation, and cell 2 active. While the remainder of the original BAW material in the 1977 ash lagoon has been treated to prevent erosion, construction on cell 3 is not apparent in this photo. Note that while both cells 1 and 2 discharge to the north end of the cell, there is some evidence of seepage and surface runoff from the southwest corner of cell 2, possibly from a decant facility.

The July 1992 photo (figure 3.14) shows the completion of the retaining dikes for cell 3, with cell 1 still inactive and awaiting reclamation, and cell 2 still active, but nearly full. Cell 3 is as yet inactive in this photo. The western margin of the cell 3 dike has been constructed along the beach front on BAW material.

The August 1993 photo (figure 3.15) shows cell 1 still inactive, and cells 2 and 3 active. It appears that cell 2 has either been emptied of a portion of its ash content, or the cell 2 dikes have been raised to increase capacity. It is unclear exactly which is the case. Note that the discharge point for cell 3 is also at the north, or narrow end of cell 3

The Autumn, 1994 photo (figure 3.16) shows the 1977 ash lagoon after the failure of cell 3. The approximate location of the dike prior to the failure is shown, and the present waterline represents the approximate location of the upstream toe of the dike. Note that the water level in the 1977 ash lagoon was lower than its normal operating level immediately following the failure, and the failure surface was temporarily exposed. Note also that ash material is now being discharged in the 1977 Ash Lagoon onto the original BAW material to the south of cell 3.

3.2.2. Review of Site Survey Data

TransAlta Utilities made available as-built survey records dated July 30, 1992 and August 02, 1992 for cell 3 in the 1977 Ash Lagoon, originally intended for storage volume calculations. These records include 18 east-west sections across cell 3, 2 dike sections from 1977 ash lagoon waterline to cell 3 centerline, and a survey plan view of cell 3. According to this record, the elevation of the top of dike was approximately 742 m, with an outlet at approximately 741 m. Cell 3 had a calculated storage capacity of 91960 cubic meters, or approximately 1 year of ash production.

3.2.3. Review of Post-Failure Video

On March 21st, 1994, in the week following the failure, a group was taken on a tour of the 1977 Ash Lagoon. The tour was videotaped with a running narration, as well as an account of the failure by one TransAlta employee. While it should be noted that much of the information contained in the narration and second-hand account of the failure has been shown by other sources to be inaccurate, it is never the less a useful record.

The following is an excerpt from a transcript of the video, in which a TransAlta Utilities employee describes the failure event.

What we're looking at here is one of the ash lagoons cells that was constructed last summer to hold a half year's production of bottom ash from the Wabamun plant. The purpose of the cells was to increase the retention time of the water going through the system in order to reach environmental limits. the cells were filled and the extra retention time with the overflows on the top of the dikes allowed us to meet the regulations. The ash dikes themselves are made from bottom ash excavated from the cell itself and piled up on top of the ash lagoon.

A week ago on a routine inspection we noticed a crack forming on the north end of the dike on the far side of where we're standing and we had a contractor come in to inspect and do some repairs on the dike. Approximately four hours after the crack was discovered the contractor thought he heard water running. He moved his equipment off the dike and he thought while he was moving it he felt the dike itself move and about 30 seconds after that the dike, from where we're standing here, sheared off. The entire structure moved off to the west about 75 to 100 feet. At that point in time we had about 100,000 cubic meters of water in the dike - in the cell itself - plus there was probably about 60,000 cubic meters of ash that was built within the dike and that shifted over a period of a couple of seconds, according to the contractor that saw the dike fail.

{portion deleted}

When the dike failed it created a wave within the existing ash lagoon. Around the periphery the ice was shot out from the surface of the water and in some places it shot out over 100 feet with the wave that came through the system. we saw very little water anywhere within the system that overflowed the dikes after, but we saw the ice sitting in some places just about 100 feet away from the dike. But no indication of water so it looks like it just shot the ice out. You can still see some of the ice.

This account does not agree exactly with that of the contractor who witnessed the event. Key in the discrepancies is the nature and location of the original crack that was noticed and caused the contractor to be brought on site, and the exact nature of the failure event. While this account describes a crack at the north end of the dike, the contractors account makes no mention of cracking, but rather describes a problem of overtopping at the midpoint of the dike. Second, this account suggests a single, catastrophic failure event, while the contractor describes the event as a chain reaction triggered by a small section of dike failing. It is unclear why these discrepancies exist, or what significance they hold.

Note also that there are other discrepancies between the information provided in the video and information documented by other sources. While the account suggests that cell 3 “was constructed last summer {summer 1993} to hold a half year’s production of bottom ash from the Wabamun plant,” the review of aerial photograph records and site survey data show that it was completed in the summer of 1992, and calculations suggest that the 100,000 cubic meter capacity of this cell represents one full years production of bottom ash. While these errors are not significant of themselves, they cast certain doubt on this account of events. A review of the erosion patterns viewed in the video offers further support to the contractors account of the failure. If the dike had let go in one large section, with cracks at the north and south ends, one might expect the erosion from the outlet of water, and the deposition of stored ash, to be concentrated in these locations. However, what is observed in the video is deposition of material in the mid-section of the dike, with clean cracks at either end, suggesting a failure that initiated at the center. This is further supported by the location of the failed material in the post-failure aerial photograph, figure 3.16.

When the failure occurred, it caused a temporary lowering of the water table within the 1977 ash lagoon due to the displacement of the ice. While the failure surface is presently below the pond level, it appears to be exposed at the time of the video. Where it has not been obscured by the deposition of material in the mid-section of the dike, the failure plane appears to originate in a backscarp 1 to 2 meters high in the upstream toe of the dike, and extends at a very shallow slope into the pond.

	Triptodi and Cheremisinoff (1980)		Joshi and Marsh (1987) Wabamun Fly Ash (Wt. %)
	Minimum (Wt. %)	Maximum (Wt. %)	
Silica, SiO ₂	6	68	59.2
Aluminum, Al ₂ O ₃	4	44	22.3
Iron, Fe ₂ O ₃	1	44	2.9
Calcium, CaO	0.2	52	9.9
Magnesium, MgO	0.1	14	2.1
Sulphur, SO ₃	0.1	32	0.9
Sodium, Na ₂ O	0.09	28	0.3
Potassium, K ₂ O	0.1	4	0.2
Titanium, TiO ₂	0.4	4.17	<1.6
Loss on Ignition	0.1	20	0.4

Table 3.1: Typical Mineralogy for Coal Fly Ash.

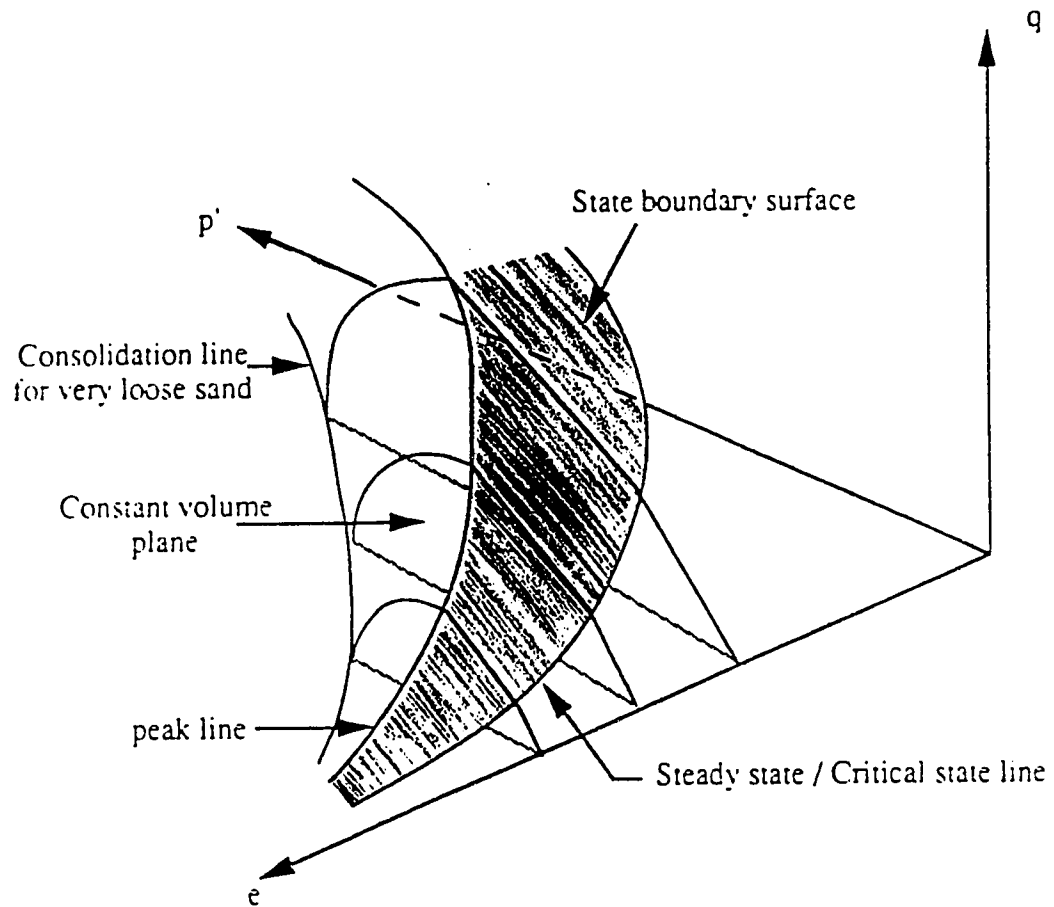


Figure 3.1: Schematic of the three dimensional CSSM framework for soil state, after Sasitharan (1994).

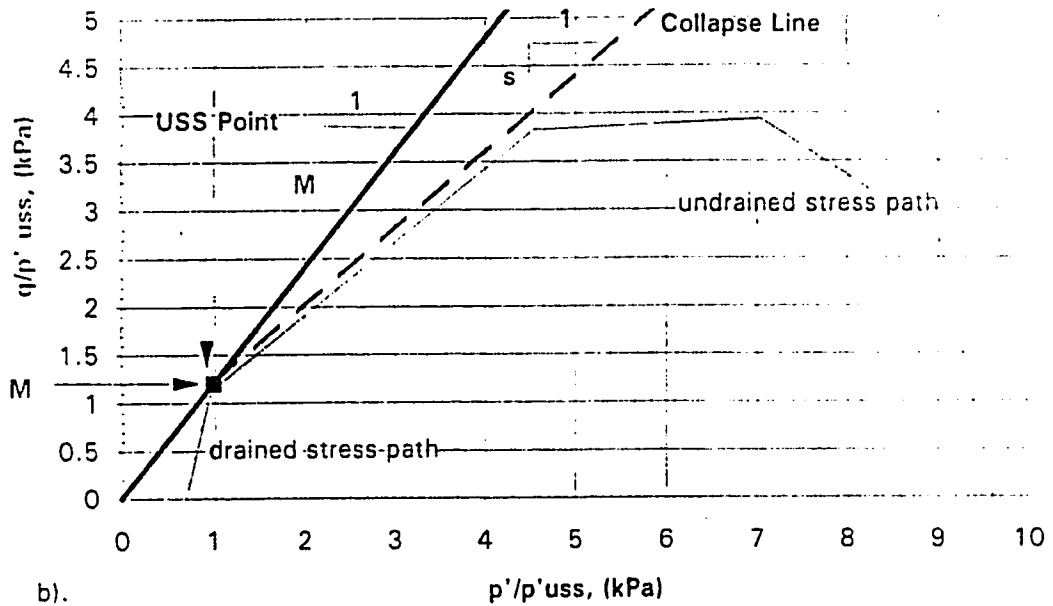
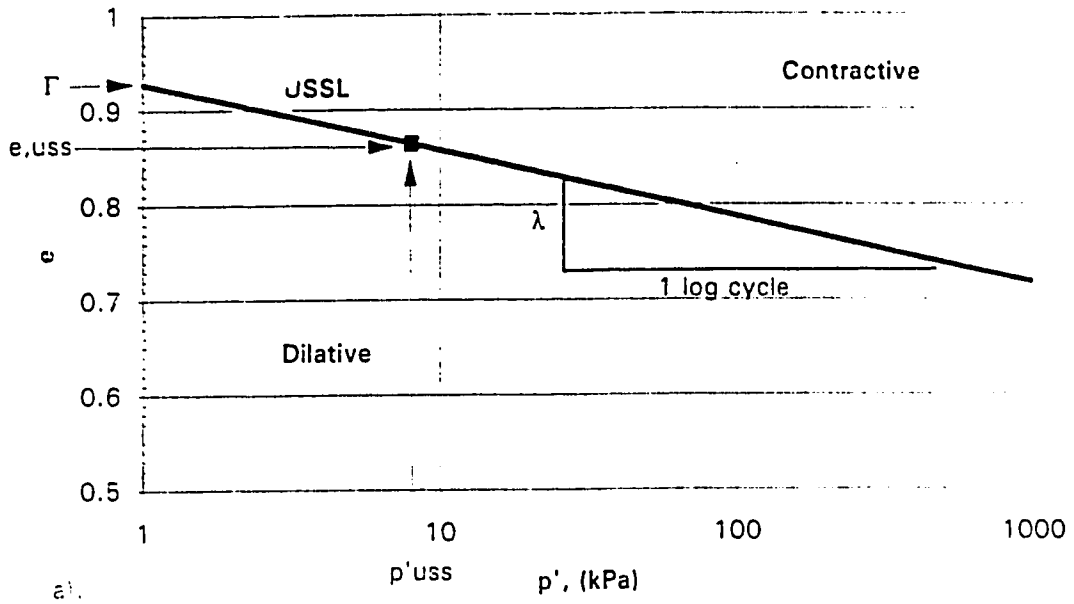


Figure 3.2: Definitions of the USS parameters in a) e against $\log p'$ space and b) normalized stress path space (Cunning, 1994).

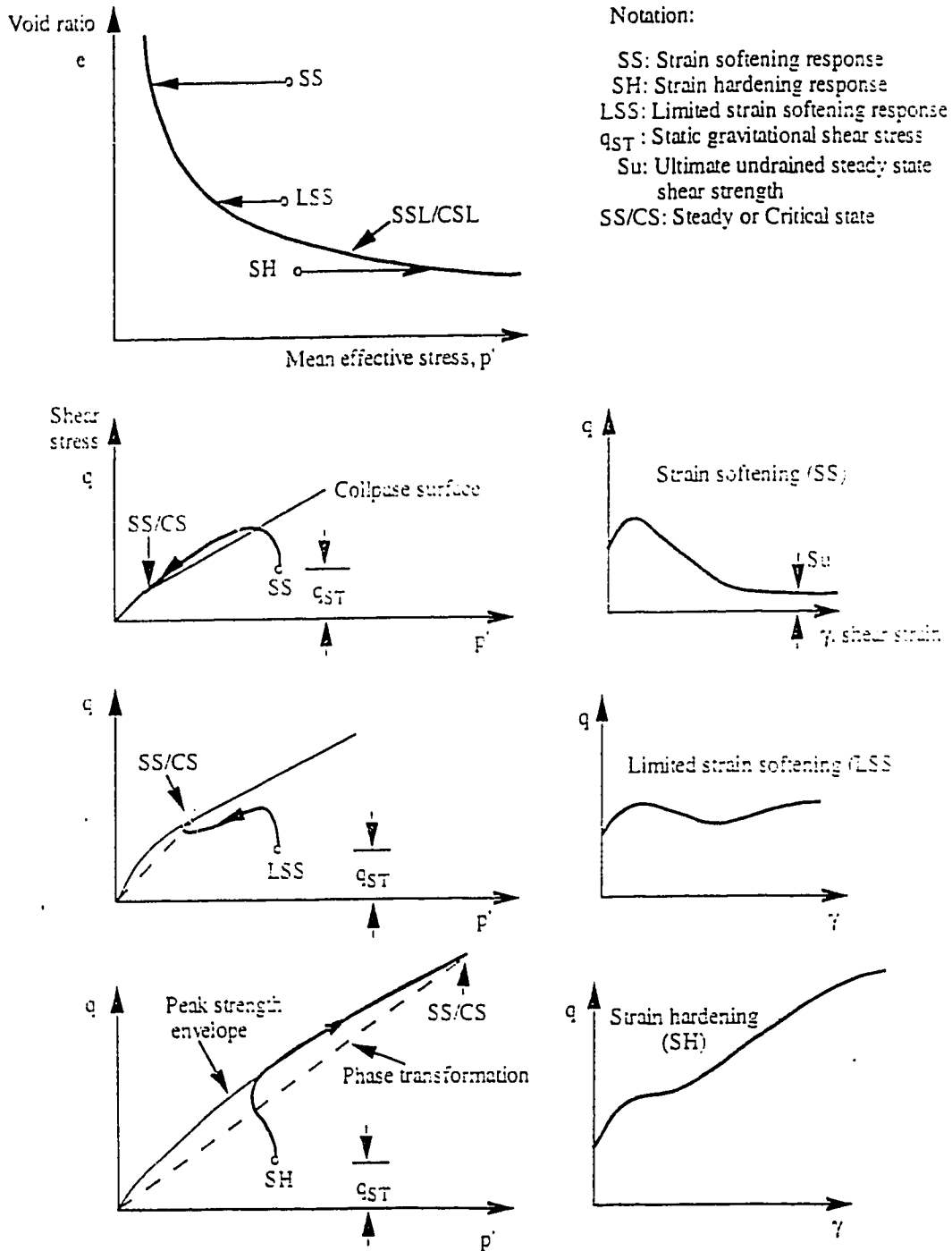


Figure 3.3: Schematic behavior of cohesionless soil in response to loading, after Robertson (1994).

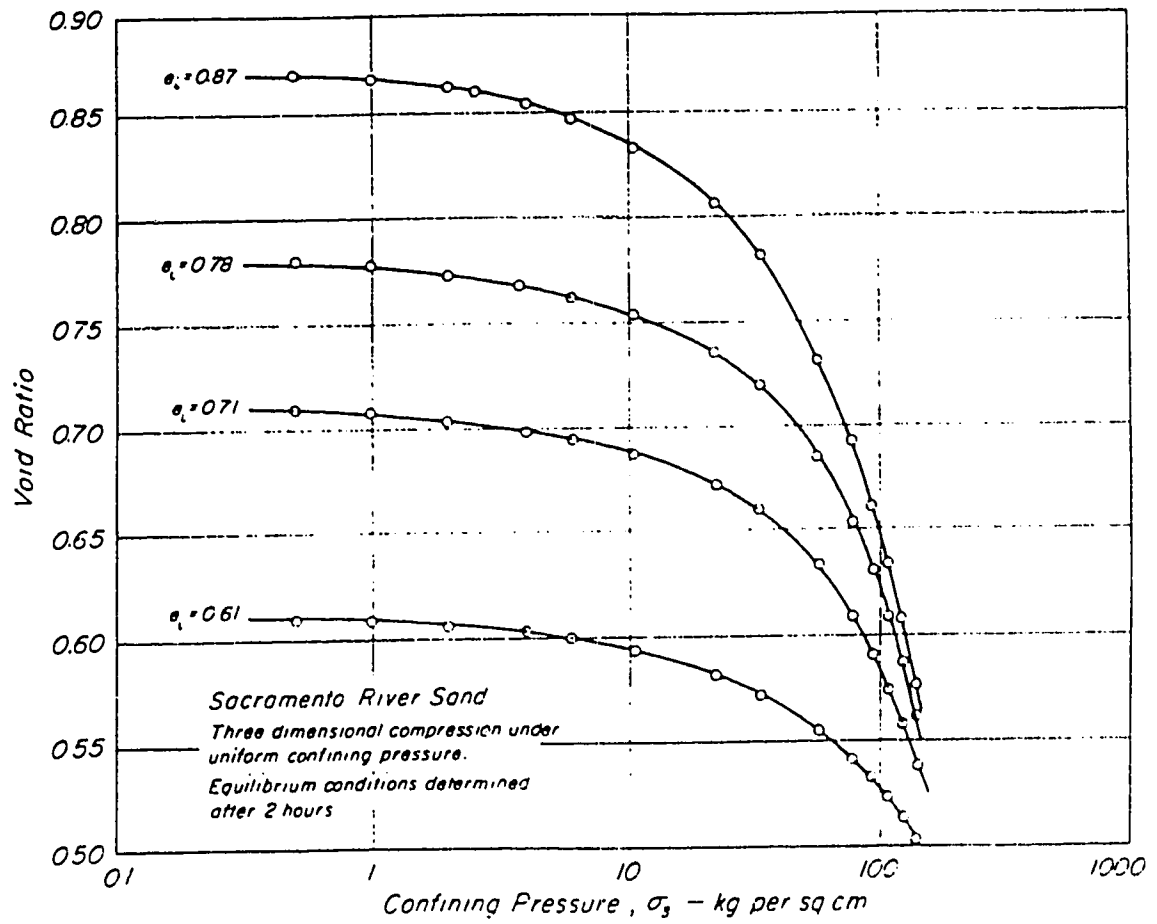


Figure 3.4: Void ratio against effective stress for Sacramento River sand (Lee and Seed, 1967).

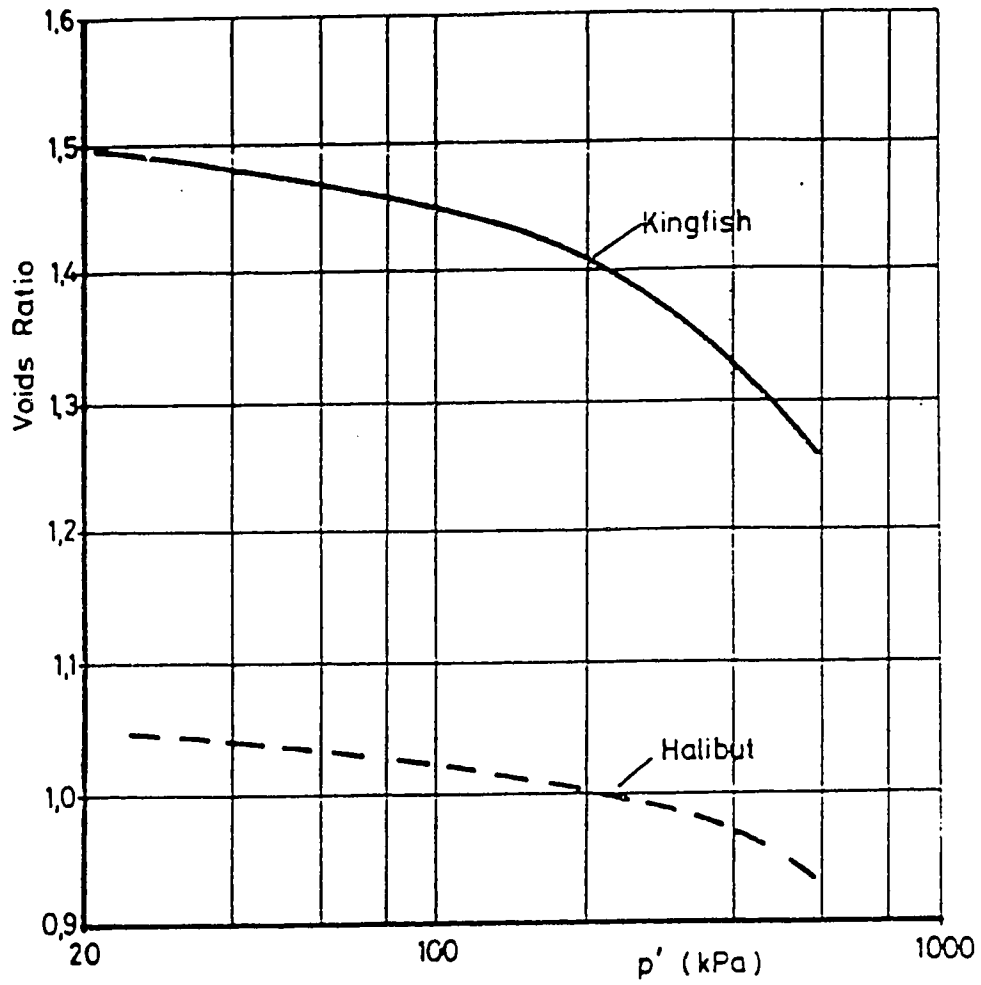


Figure 3.5: Void ratio against effective stress for Kingfish sand and Halibut sand (Airey et al., 1988).

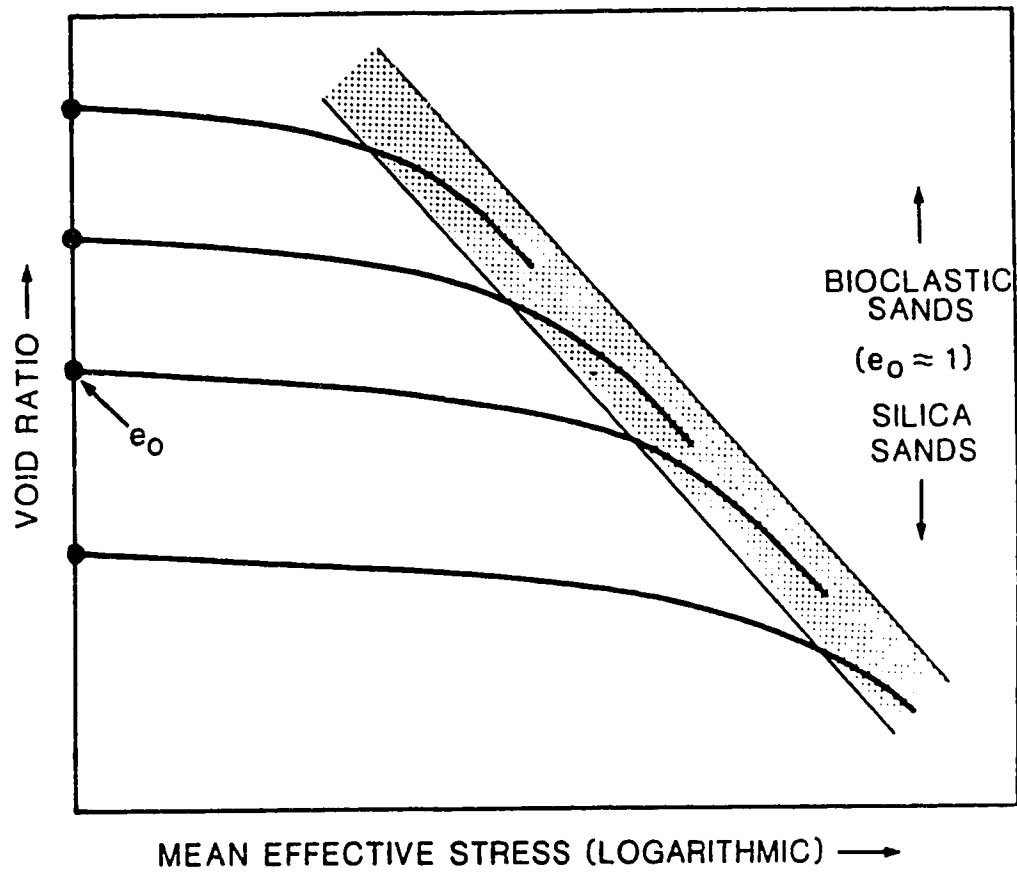


Figure 3.6: Schematic of the limiting state line for cohesionless soils (Sempke, 1988).

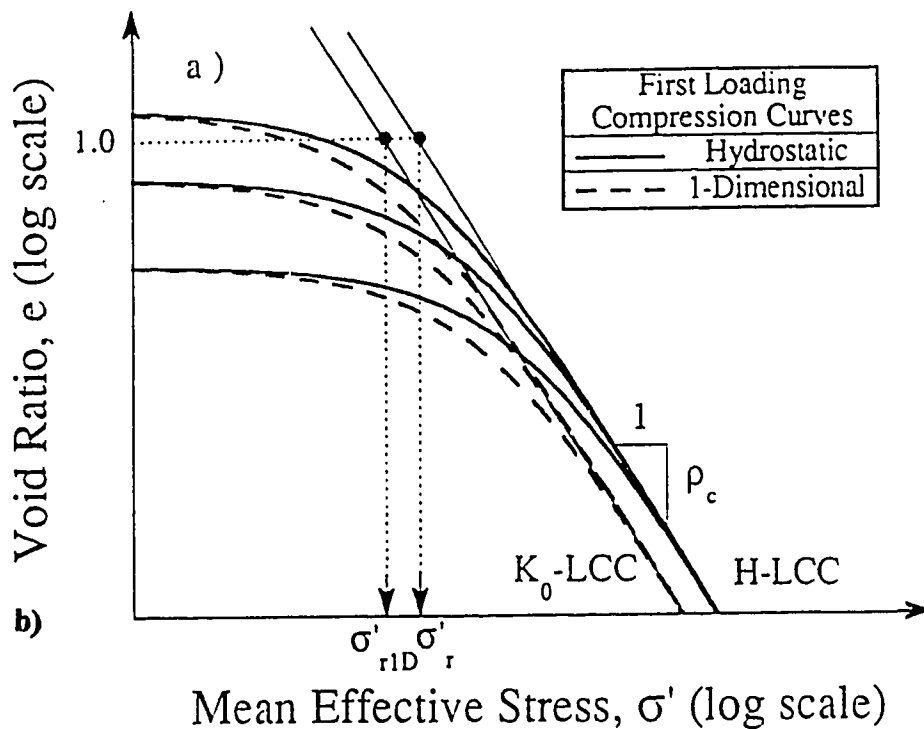
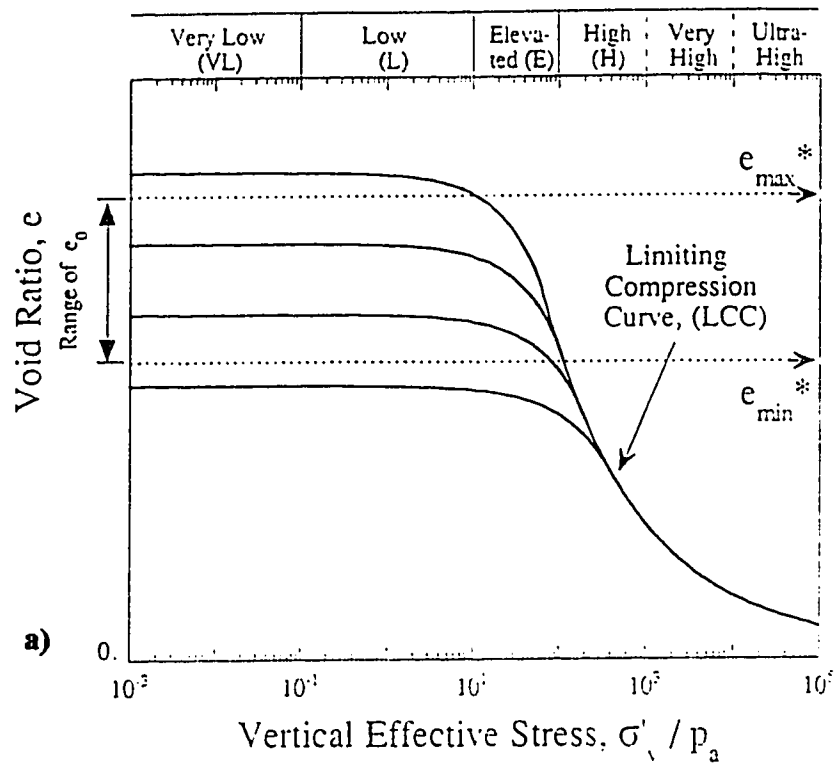


Figure 3.7: Schematic of the limiting consolidation curve for cohesionless soils in a) e - $\log p'$ space, and b) $\log e$ - $\log p'$ space (Pestana and Whittle, 1995).

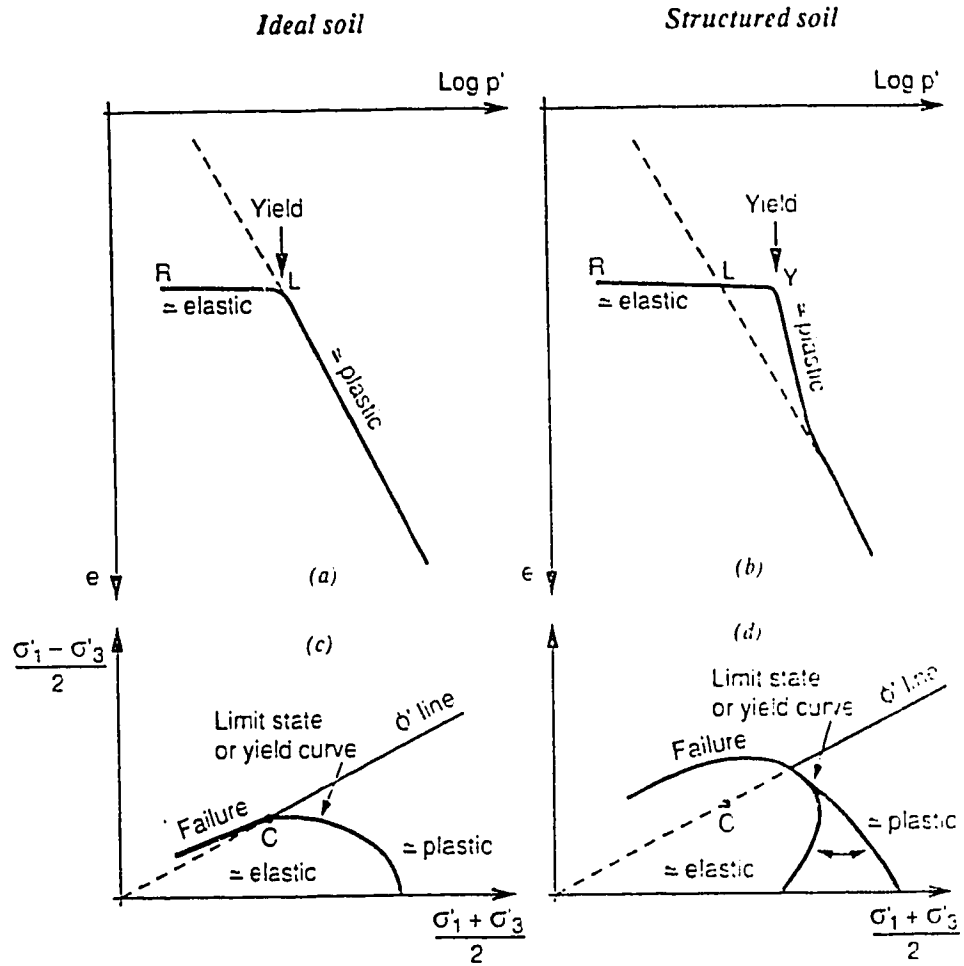


Figure 3.8: Schematic behavior of ideal and structured soils (Leroueil, 1992).

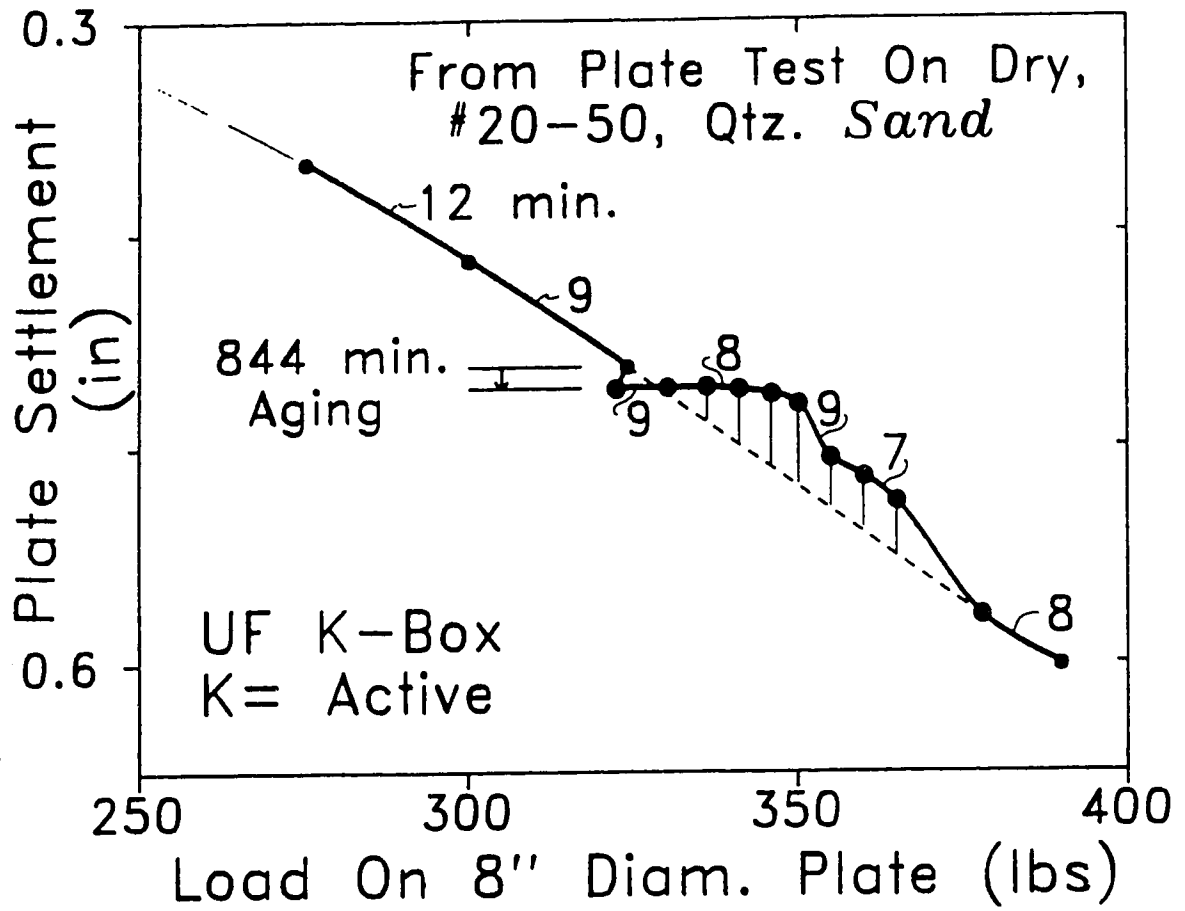


Figure 3.9: Plate settlement against load for a plate load test on dry quartz sand (Schmertmann, 1991).

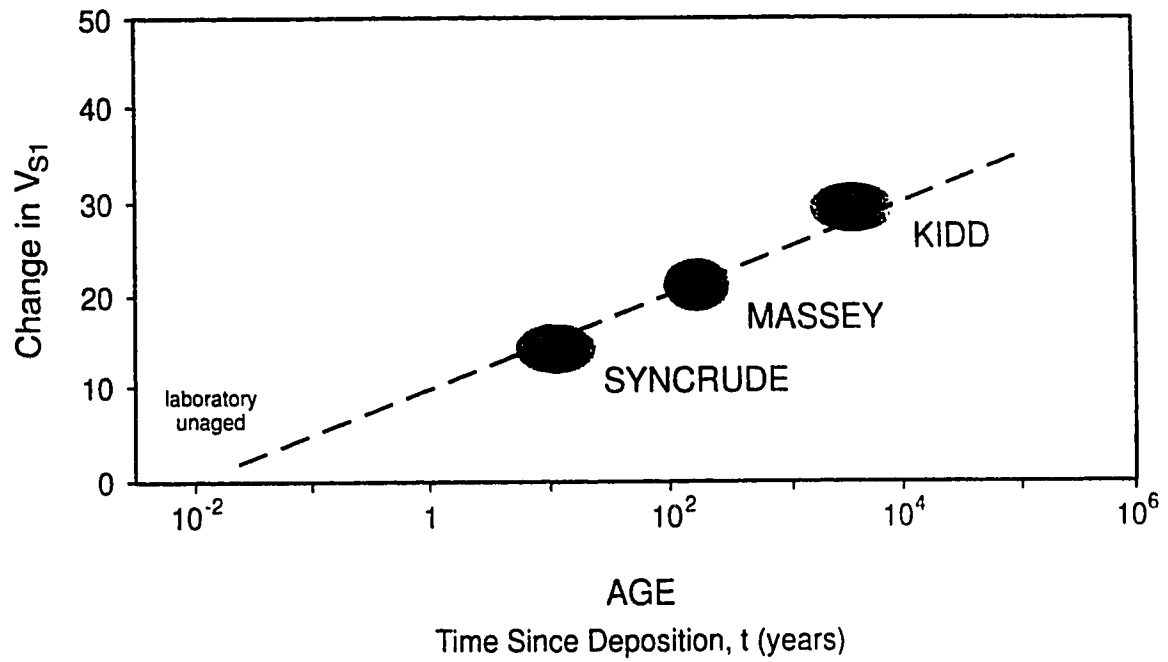


Figure 3.10: The effect of aging on normalized shear wave velocity for sands (Robertson et al, 1995).

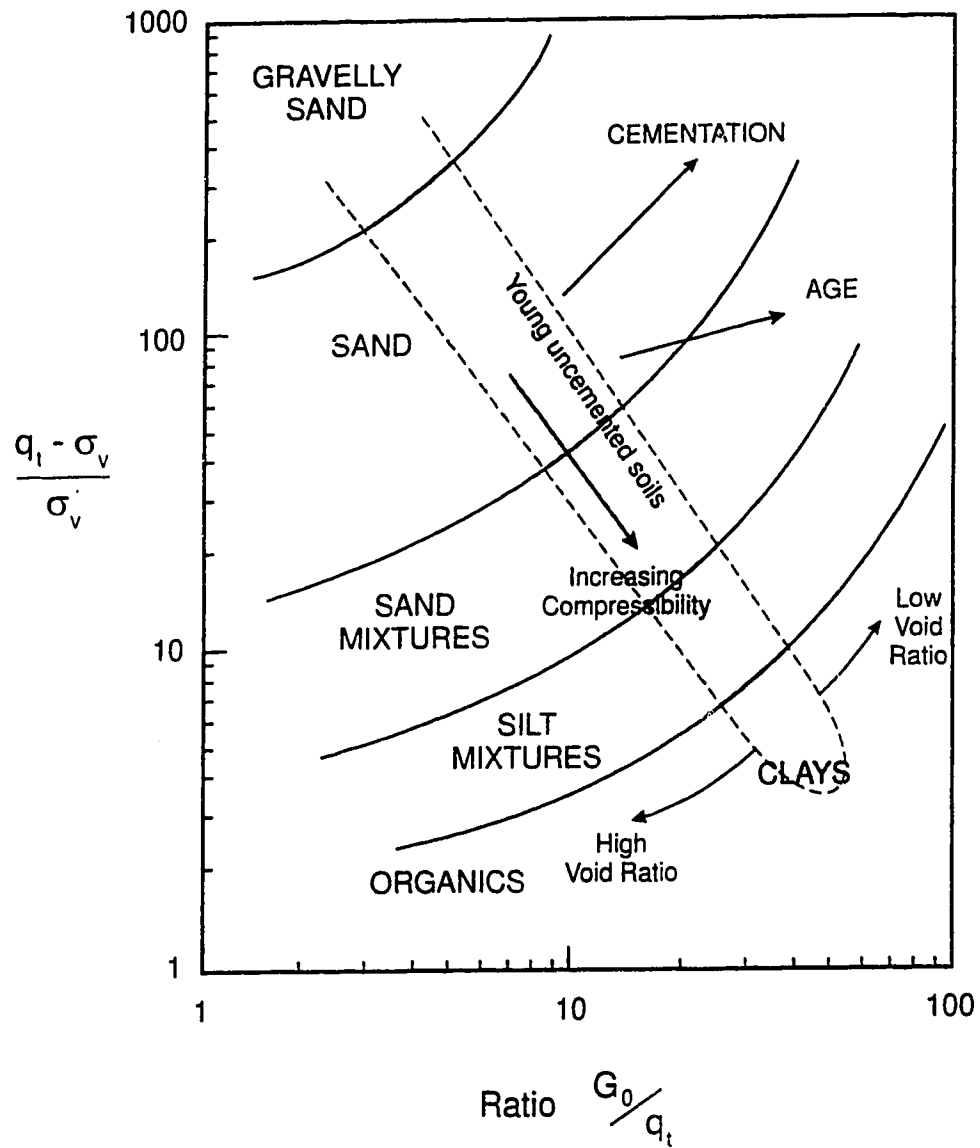
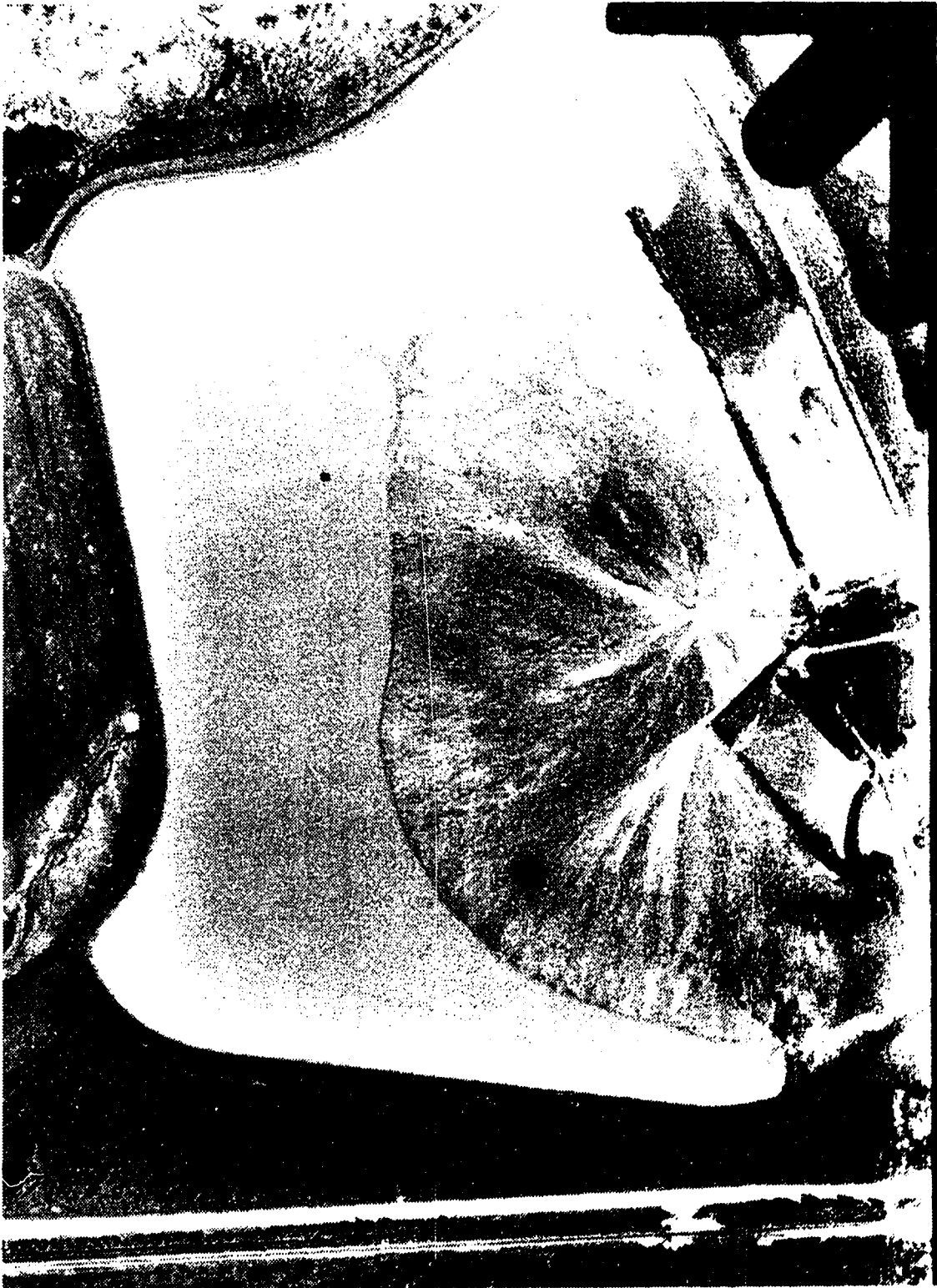


Figure 3.11: Classification chart to evaluate soil behavior type (Robertson et al, 1995).



**Figure 3.12: Aerial photograph of the 1977 ash lagoon taken September 03, 1989.
(Maps Alberta Airphoto #3909-107)**



Figure 3.14: Aerial photograph of the 1977 ash lagoon taken July, 1992. (TransAlta Utilities)

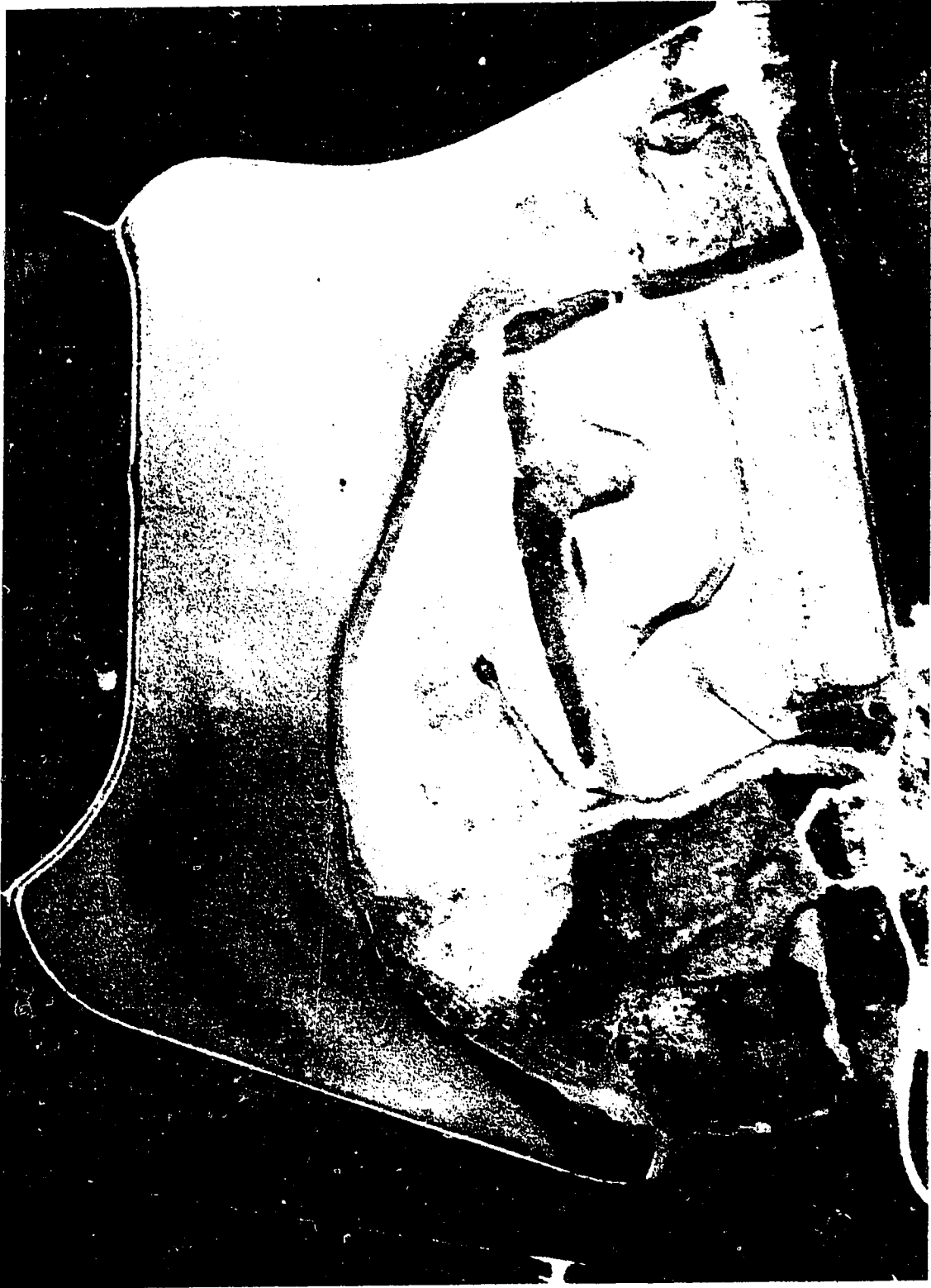


Figure 3.15: Aerial photograph of the 1977 ash lagoon taken August, 1993.
(TransAlta Utilities)



Figure 3.16: Aerial photograph of the 1977 ash lagoon taken November, 1994.
(TransAlta Utilities)

4. Site Investigation and Material Characterization

Field work on the site conducted in the summer and fall of 1994 included bulk sampling in order to obtain index properties, in-situ testing to characterize the site, and finally in-situ sampling to allow for site-specific interpretation of the in-situ testing. Figure 4.1, August 1994 shows the 1977 ash lagoon with the sampling and testing locations indicated. Numbers B1 through B5 denote bulk sampling locations, while I1 through I4 denote in-situ test locations. Note that while bulk samples were all taken within the failure area, all in-situ tests were conducted on beach deposits to the south of cell #3. It is intended that bulk sampling represent the material within the failure area, while the in-situ testing be used to delineate the stratigraphy of the deposits prior to the failure. In-situ test locations were selected to represent material beneath the downstream toe of the dike (I1), the centerline of the dike (I2), the upstream toe of the dike (I3) and the center of the cell (I4).

4.1. Preliminary Site review

Following the failure of cell 3, tailings pipes were relocated and ash disposal was confined to the 1977 Ash Lagoon beach south of the existing cells. The material exhibits a BAW slope of 1 to 2 degrees based on inclinometer readings taken down the beach. The BBW slope was estimated from the slope along which the failed material moved to be around 8 degrees.

Upon failing, the material moved out into the lagoon up to 75 m in 5 largely intact blocks. These blocks continued to exhibit near vertical fracture faces even some months after the failure, suggesting a cohesion in the material at least in its drained and compacted state. This agrees with the general strength characteristics reported for compacted bottom ash of $\phi = 42$ degrees and $c = 30 \text{ kN/m}^2$ suggested by the Geotechnical Department of Helsinki (1983).

4.2. Bulk Grab Sampling

In order to begin characterizing the materials on site, and in order to have sufficient sample for later laboratory determination of the collapse surface for the material, a number of bulk grab samples were taken. Samples of bottom ash and fly ash were also obtained from the plant in order to characterize the material at its source. Five samples were taken in cell 3, in locations B1 through B5 identified in Figure 4.1.

A variety of index tests were conducted on the bulk samples, including grain size, specific gravity, e_{\max} and e_{\min} , and Atterberg limits. It was recognized during index testing that due to the weak and friable nature of the material, excessive handling resulted in a degradation of grain size. Consequently, ASTM standards were followed for all tests, except in instances where it was felt that these standards would result in damage to the sample. Also, the testing program was conducted to ensure that handling of samples was minimized, and that test samples were not reused.

The results of the specific gravity tests assume that samples achieve full saturation due to the application of a vacuum. However, it is possible that micropores within the Wabamun sand do not saturate in the process. The specific gravity measured should only be considered a bulk specific gravity, and may not be an intrinsic property of the ash itself, but rather of the structured soil grains.

Table 4.1 summarizes the index properties for the bulk samples. Note the low specific gravity's (2.21 to 2.27) and the variable but high e_{\max} and e_{\min} (e_{\max} up to 2.51 and e_{\min} up to 1.93) of the materials. Figure 4.2 shows the grain size distribution curves for these samples. Note that the material that leaves the plant (the Bottom Ash: Plant Feed sample) is much coarser than that found in the storage lagoons (the bulk grab samples 1 through 5). This is likely a result of breakdown of the particles during slurry transport from the plant to the ash lagoons. Note also the variation in grain size distributions.

4.3. In-Situ Sampling

In-situ sampling was conducted in conjunction with the cone penetrometer testing (CPT) at location I1 to allow for site specific interpretation of the CPT profile. Two non-standard methods of sampling were attempted, with varying success. In one sampling method, a simple hand operated piston sampler constructed by the University of Alberta for use in soft tailings material was pushed into the ground, the cutting shoe advanced, and a sample retrieved. In the stiff crust material, where this tool could not be advanced by hand, an alternative method was used. A casing (100 mm PVC pipe) was driven into the ground to the desired depth, the casing backfilled above the sample to reduce air volume in the tube, and then capped and withdrawn to obtain a sample. It was found that this method left an open hole through the crust material through which the piston sampler could be advanced into the softer material below. In all, four samples were taken -- two in denser crust material by the casing method at depths of 0.0 and 0.5 meters, and two in the softer material by the piston sampler at depths of 1.3 and 1.8 meters. Samples were designated by location and depth as I1 @ 0.0 m, I1 @ 0.5 m, I1 @ 1.3 m, and I1 @ 1.8 m.

Table 4.2 summarizes the index properties of this material, and Figure 4.3 shows the grain size distribution. Note that unlike the bulk grab samples, there is little variation in grainsize between the piston samples.

4.4. Scanning Electron Micrographs

Scanning electron micrograph (SEM) work was conducted on six samples with three goals in mind. The goals were first to examine the ash material to determine if any differences existed between the microscopic and the macroscopic portions. This is in order to determine if the fines exhibit any characteristics that set them apart from the coarser portions. Second was to conduct qualitative mineralogical determinations on the samples to determine mineral constituents and to verify that bottom ash, the material in question, and fly ash, the material most commonly tested by other researchers, are similar in mineralogy. Third and finally was to compare the material sampled in situ, samples I1 @ 1.3 m and I1 @ 1.8 m to verify that they can reasonably be represented by bulk

samples # 2 and # 3 in later testing. In total for the six samples, 24 photographs were taken, and 11 qualitative mineralogy's conducted.

The samples viewed were bottom ash plant feed, fly ash plant feed, bulk sample #2, bulk sample #3, sample I1 @ 1.3 m and sample I1 @ 1.8 m. Samples were prepared from the passing #20 sieve portion of a representative bulk sample. Due to the extremely small size of sample used in the SEM, and the difficulty in obtaining an exactly representative sample, exact grain size distributions may not be represented in the photographs.

In order to make comparisons between the macroscopic scale, in which the grains can be identified by color as well as texture, and the domain of the SEM, where only surface contour can be identified, it was necessary to select grains according to their macroscopic description (Tables 4.1 and 4.2), and view and qualitatively identify mineralogy in the SEM. Figures 4.4 to 4.7 show photographs of the grains and their corresponding mineralogy. From this it was concluded that the gray, porous and friable grains in the hand samples corresponded to the Silicon, Aluminum and Calcium based clinker material in the SEM, and the black, vitreous, subangular material in hand sample corresponded to the blocky carbon grains in the SEM. This corresponds to the concept that the clinker originates from non-flammable minerals within the coal, and the black, vitreous material forms due to incomplete burning of the coal.

Figure 4.8, taken of sample I1 @ 1.8 m shows a grain of clinker type material, along with a piece of petrified wood, and a carbon grain. This photo shows the material at approximately 50 times magnification to be porous and highly angular, similar to the descriptions of macroscopic samples. Once again the clinker material was found in analysis to be predominantly Silica, Aluminum, and Calcium. Figure 4.9, taken of sample B2, however, shows that at sufficiently small scale, the material can be made up of agglomerated fly ash cenospheres. Thus the material exhibits no differences between the microscopic scale and the macroscopic scale up to approximately 100 times magnification. At 250 times magnification, this no longer holds true. For the purposes of

this study, however, this scale effect will be ignored in the selection of grain size distributions for triaxial test samples.

General, qualitative mineralogical analyses of SEM sample 1 - bottom ash plant feed (Figure 4.10), and SEM sample 2 - fly ash plant feed (Figure 4.11), show that these materials are similar in mineralogy, with the exception that the carbon found in the bottom ash is generally not found in the fly ash. In terms of mineral habit, these figures show that while the cenospheres that make up the fly ash are present in the bottom ash, the fly ash has none of the agglomerates seen in the bottom ash. In general, it can be concluded that mineralogical analyses based on the constituents of fly ash should not be considered equally representative of the corresponding bottom ash material.

Figure 4.12 shows bulk samples # 2 and # 3 and samples I1 @ 1.3 m and I1 @ 1.8 m, each at 100 times magnification. In light of the conclusions already noted, and the fact that the samples cannot be considered fully representative of the source materials, there appears no reason that the bulk samples should not be considered representative of the in-situ material.

4.5. Piezometric Cone Penetrometer Testing (CPTU)

Piezometric Cone penetrometer soundings were conducted at four locations in the 1977 Ash Lagoon, as indicated in Figure 4.1. These soundings were conducted on the original beach slope to the south of cell #3 in order to estimate the stratigraphy of the material beneath cell 3. Soundings were attempted on the failed material in cell 3 for comparison. These soundings met refusal at very shallow depths, likely due to the presence of the gravel scour control material.

4.5.1. Piezometric Cone Testing Procedure

Soundings were conducted using a modified vane shear frame weighted with lead weights to push an ASTM standard 2.5 ton capacity piezometric cone supplied by ConeTec Investigations Ltd. This arrangement was able to produce a penetration resistance in the order of 200 bars before refusal occurred. Data was collected and

recorded by a Hogentogger data acquisition system, also supplied by ConeTec Investigations Ltd. Soundings were completed to a depth of approximately 5.5 m at the four test locations, and designated CPT-1 through CPT-4, corresponding to in-situ test locations I1 through I4.

4.5.2. Interpretation of Cone Data

Figures 4.13 to 4.16 show cone profiles CPT-1 to CPT-4 obtained in the field investigation. The beach material appears to have an upper crust ranging in thickness from 1.0 m at I1 to 2.0 m at I4. Bearing resistance is very low for a sand, with a maximum value of about 1800 kPa occurring in the crust material in CPT-4. The low bearing resistance may be related to the compressible nature of the soil (figure 3.11). Frictional resistance is also very low, with a maximum value of 8 kPa occurring in CPT-4. The actual maximum friction is possibly even smaller, around 2 kPa, as the peak at 8 kPa may be related to a pause in the penetration of the cone. Note that even though a low capacity cone was used, readings are in the lower portion of the load cell resolution, and that some of the friction values were not large enough to even register. Zhu et al. (1995) investigated the effect of cementation on lateral stresses, and indicated that this very low friction may be related to the development of cementation in the soil.

Robertson (1990) suggests a procedure for classifying soil behavior types according to CPTU response. In this procedure, data is normalized using the following parameters:

$$Q_t = \frac{q_t - \sigma_{vo}}{\sigma_{vo}'} \quad [6]$$

$$F_R = \frac{f_s}{q_t - \sigma_{vo}} * 100\% \quad [7]$$

$$B_q = \frac{u - u_o}{q_t - \sigma_{vo}} \quad [8]$$

where: Q_t = Normalized cone resistance
 F_R = Normalized friction ratio
 B_q = Pore pressure ratio
 q_t = Total cone resistance, corrected for unequal area effects (Campanella

and Robertson, 1981)

f_s	=	Sleeve friction
u	=	Pore pressure measured between cone tip and friction sleeve
u_0	=	Equilibrium pore pressure
σ_{v0}	=	Total overburden stress
σ_{v0}'	=	Effective overburden stress

The data is then plotted on a three dimensional classification system that incorporates these three normalization parameters, and which is divided into soil behavior types based on extensive empirical experience.

For this research, the normalization procedure described above was carried out using a spreadsheet program developed by Stahl (1995a). This program accepts input of the raw cone data, as well as the cone area ratio, estimated in-situ void ratio of the soil, specific gravity of the soil, soil saturation above and below the water table, and depth to the water table. The program then uses these parameters to produce plots of normalized cone resistance, normalized friction ratio and pore pressure ratio versus depth, as well as the classification plots of normalized cone resistance versus normalized friction ratio and normalized cone resistance versus pore pressure ratio.

In order to use the program, it was necessary to select soil parameters to represent the in-situ state. A void ratio of 1.5 and specific gravity of 2.3 were selected since they represent “average” values obtained from the bulk samples, and because they correspond approximately to bulk unit weights of 1300 kg/m^3 above the water table and 1500 kg/m^3 below the water table used in the interpretation of the SASW data (section 4.6). The saturation above the water table was assumed to be 75%, the saturation below the water table was taken as 100%, and the depth to the water table was determined from inspection of the raw cone data. The cone area ratio for the ConeTec Investigations Ltd. cone, used in the correcting measured cone resistance (q_c) to total cone resistance (q_t) was 0.85.

The cone data was analyzed using these parameters. Plots of normalized cone resistance, normalized friction ratio and pore pressure ratio versus depth for CPT-1 through CPT-4 can be found in figures 4.17 to 4.20. Classification charts of normalized

cone resistance versus normalized friction ratio and normalized cone resistance versus pore pressure ratio are shown in figures 4.21 to 4.23. In general, the charts classify the soil behavior as silt mixtures, sand mixtures, sands, or gravely sands to sands, which is consistent with the samples taken on site. In general, the weaker soils below the stiff crust are identified as sand mixtures. Note however that in the plots of normalized friction ratio versus depth, many of the normalized friction ratio values fall below 0.1, which is the minimum normalized friction ratio value considered by the classification chart of normalized cone resistance versus normalized friction ratio. This suggests a need to have more accurate sleeve friction measurements, as well as a more accurate method of estimating the void ratio and specific gravity in the field.

4.6. Spectral Analysis of Surface Wave (SASW) Testing

SASW soundings were conducted at the four locations in the 1977 Ash Lagoon indicated in Figure 4.1, and designated SASW-1 through SASW-4, corresponding to in-situ test locations I1 through I4

4.6.1. SASW Testing Procedure

SASW soundings were conducted using the system and method described by Addo (1991). This system and the test method are outlined in figure 4.25 (Stahl, 1995b). A single sounding is made with the receivers on the ground equidistant from a fixed centerline. A vertical blow at a source location a distance from the near receiver equal to the receiver spacing is generated by a hammer. Blows are generated manually and recorded by the microcomputer until a set of five has been averaged. The procedure is then repeated with the source location on the opposite side of the centerline. A complete sounding at a location consists of a set of single soundings taken at different spacings.

4.6.2. Interpretation of SASW Data

As described in Figure 4.25, receivers monitor the waves generated by the source. These time domain signals are filtered by the interface control unit, transmitted to the computer, and processed into the frequency domain by the computer using a fast Fourier

transform algorithm. This frequency domain data is output in the form of phase velocity against wavelength to form a dispersion curve. This dispersion curve is then used to forward model a profile of shear wave velocity against depth. In the process of forward modeling, bulk densities and Poisson's ratio are estimated for the material, and shear wave velocities and layer thicknesses are selected to match the field dispersion curve. The selected data is correct if the theoretical dispersion curve constructed from the data matches the field dispersion curve. Output from a SASW sounding will therefore consist of two plots. The first plot is of Rayleigh velocity against wavelength showing the field dispersion data and a theoretical curve based on the plot of shear wave velocity against depth. The second is the plot of shear wave velocity against depth.

The data analysis was undertaken by University of Alberta Ph.D. candidate Richard Stahl. This operation was conducted using field dispersion curves visually constructed from selected data and estimated bulk unit weights of 1300 kg/m^3 above and 1500 kg/m^3 below the water table. The depth of water is as determined by CPT tests at the same locations. With the exception of SASW-1, in which the crust was too thin to model effectively, analysis was conducted first assuming the material to be constant with depth, then assuming a stiff (higher shear wave velocity) crust.

Figures 4.26 to 4.29 show the paired plots of Rayleigh velocity against wavelength and shear wave velocity against depth for SASW-1 to SASW-4. Note the effect the assumption of a higher velocity crust has in creating a low velocity (and therefore looser) region beneath the crust. The effect of this assumption will become more clear when shear wave velocities are used in a V_s - e - p' relationship to estimate in-situ state.

Sample Name	Atterberg Limits	Specific Gravity	Void Ratio		Grain Size Distribution	Descriptive Classification	USC Description
			e _{max}	e _{min}			
Bottom Ash Plant Feed	Non-plastic				Gravel % 33.4 Sand % 61.6 Fines % 5.0	Gravelly sand with trace fines. Predominantly gray to gray-brown, porous and friable grains.	SP
Fly Ash Plant Feed	Non-plastic				Gravel % 0.0 Sand % 18.7 Fines % 81.3	Silt and some sand. Gray, non-plastic. Low dry strength.	ML
Bulk Sample 1	Non-plastic	2.27	1.64 - # 4 Sieve	1.08	Gravel % 3.0 Sand % 79.2 Fines % 17.8	Sand with some silt and trace gravel. Gravel 40% gray, porous, friable grains, 40% black vitreous subangular grains and 20% rounded, gray-brown stones. Sand 70% gray porous material, 30% black vitreous material.	SM
Bulk Sample 2	Non-plastic	2.21	2.51 - # 10 Sieve	1.61	Gravel % 5.9 Sand % 86.6 Fines % 7.5	Sand with trace silt and trace gravel. Gravel 50% gray, porous, friable grains, 50% black vitreous subangular grains. Sand 80% gray porous material, 20% black vitreous material.	SW/SM
Bulk Sample 3	Non-plastic	2.23	2.21 - # 10 Sieve	1.83	Gravel % 5.0 Sand % 86.0 Fines % 9.0	Sand with trace silt and trace gravel. Gravel 70% gray, porous, friable grains, 30% black vitreous subangular grains. Sand 90% gray porous material, 10% black vitreous material.	SW/SM
Bulk Sample 4	Non-plastic				Gravel % 2.1 Sand % 35.0 Fines % 62.9	Sandy silt with trace gravel. Gravel 50% gray, porous, friable grains, 50% black vitreous subangular grains. Sand 90% gray porous material, 10% black vitreous material. Silt gray, non-plastic with low dry strength.	ML
Bulk Sample 5	Non-plastic	2.26	1.20 - # 4 Sieve	0.61	Gravel % 1.4 Sand % 40.6 Fines % 58.0	Sandy silt with trace gravel. Gravel 50% gray, porous, friable grains, 50% black vitreous subangular grains. Sand 90% gray porous material, 10% black vitreous material. Silt gray, non-plastic with low dry strength.	ML

Table 4.1: Index Properties for Bulk Samples From the Wabamun Plant and from Locations B1 through B5.

Sample Name	Atterberg Limits	Specific Gravity	Void Ratio		Grain Size Distribution	Descriptive Classification	USC Description
			e_{max}	e_{min}			
CPT-1 at 0.0 m	Non-plastic				Gravel % 23.4 Sand % 68.7 Fines % 7.9	Sand with some gravel and little fines. Gravel 60% grey, porous and friable grains, 40% black vitreous subangular grains. Sand 90% grey, porous material, 10% black vitreous material	SP/SM
CPT-1 at 0.5 m	Non-plastic				Gravel % 14.3 Sand % 82.5 Fines % 3.2	Sand with some gravel and little fines. Gravel 30% grey, porous and friable grains, 70% black vitreous subangular grains. Sand 90% grey, porous material, 10% black vitreous material	SP
CPT-1 at 1.3 m	Non-plastic				Gravel % 26.2 Sand % 72.5 Fines % 1.3	Sand with some gravel and little fines. Gravel 50% grey, porous and friable grains, 50% black vitreous subangular grains. Sand 90% grey, porous material, 10% black vitreous material	SP
CPT-1 at 1.8 m	Non-plastic				Gravel % 16.8 Sand % 78.9 Fines % 4.3	Sand with some gravel and little fines. Gravel 60% grey, porous and friable grains, 40% black vitreous subangular grains. Sand 90% grey, porous material, 10% black vitreous material	SP

Table 4.2: Index Properties for In-situ Samples from Location 11.



Figure 4.1: November, 1994 aerial photograph of the 1977 ash lagoon with sampling and testing locations indicated.

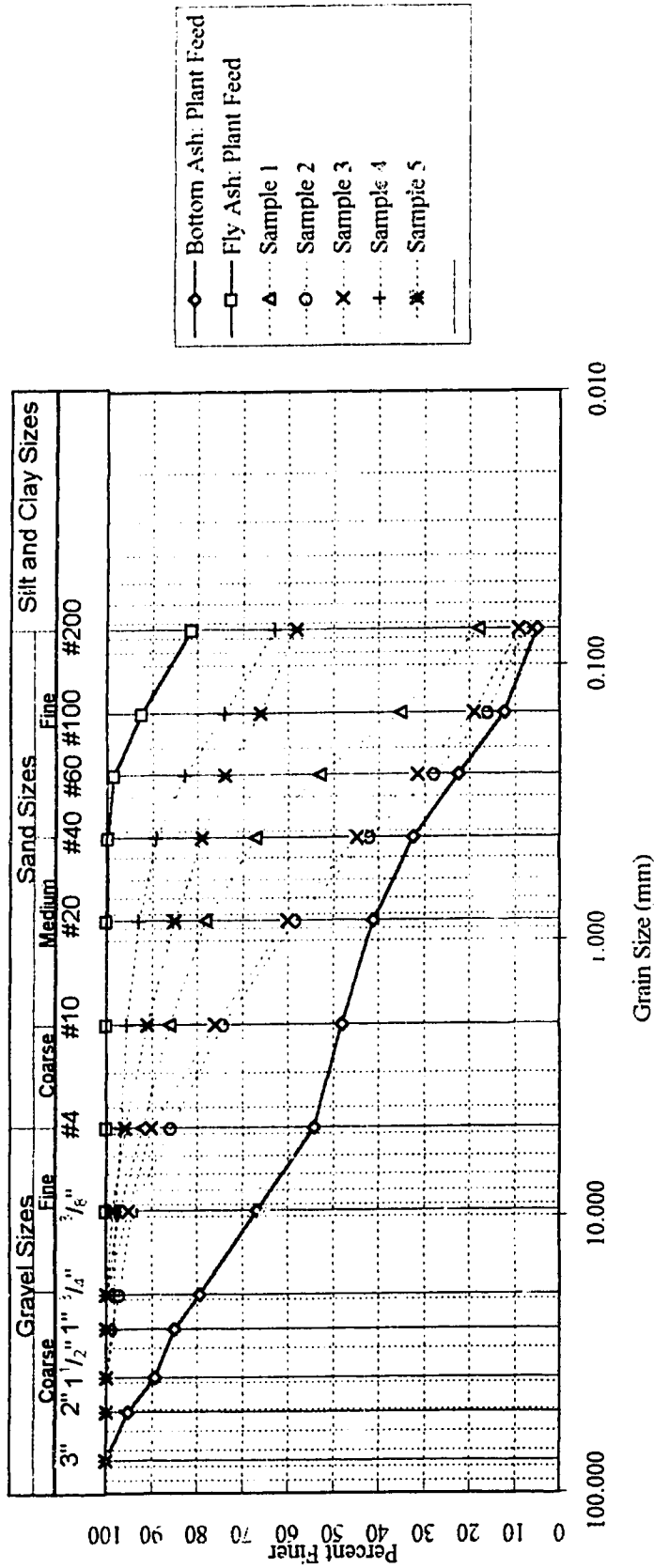


Figure 4.2: Grain size distributions for bulk samples taken from the Wabamun plant and from sample locations B1 through B5.

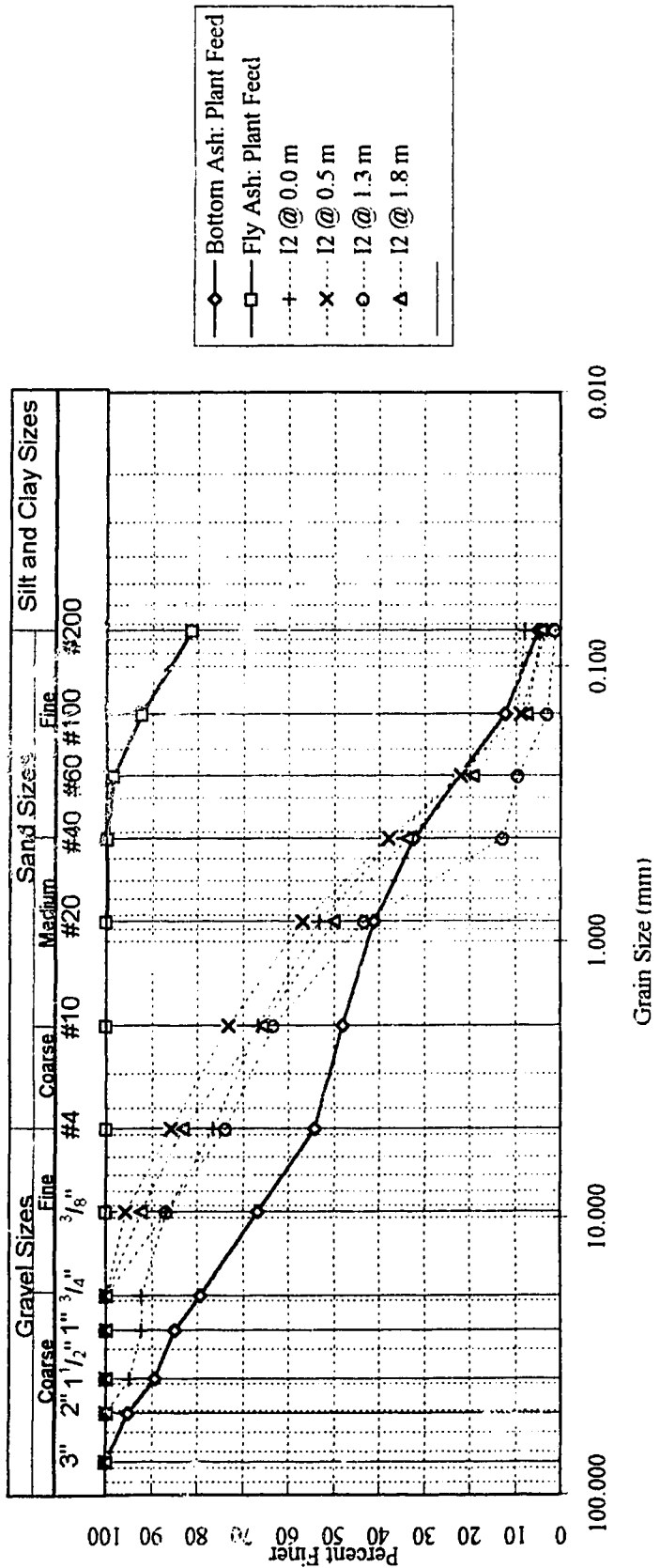


Figure 4.3: Grain size distributions for piston samples taken at location 11.

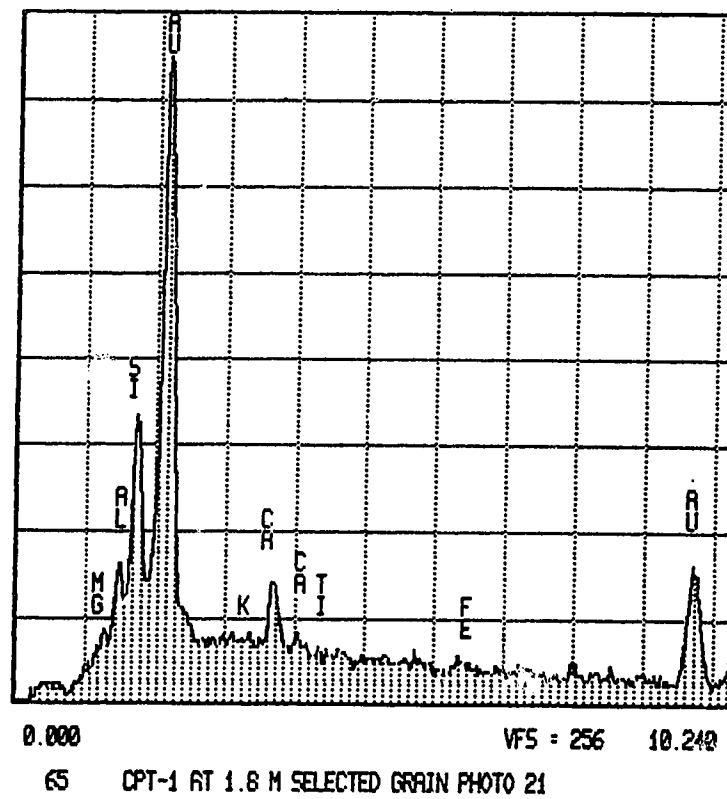
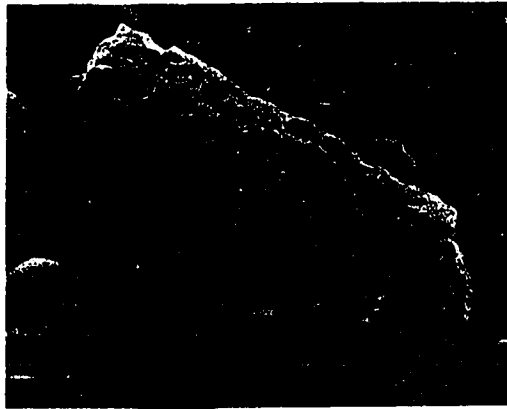


Figure 4.4: SEM photograph and qualitative mineralogy for black, vitreous and blocky sand grain. Analysis shows grain to be predominantly carbon.

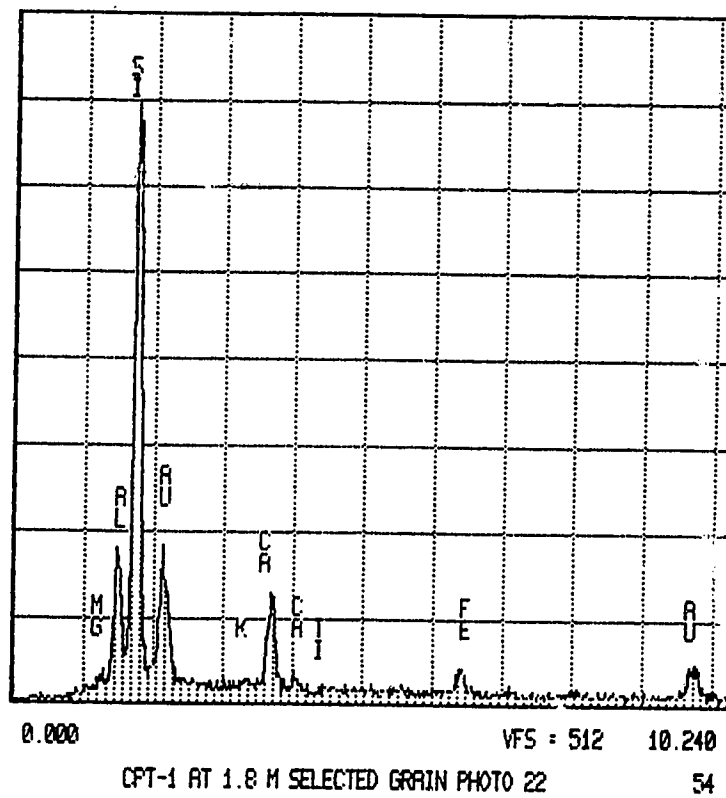


Figure 4.5: SEM photograph and qualitative mineralogy for white, glossy sand grain. Analysis shows grain to be predominantly silica, aluminum and calcium.

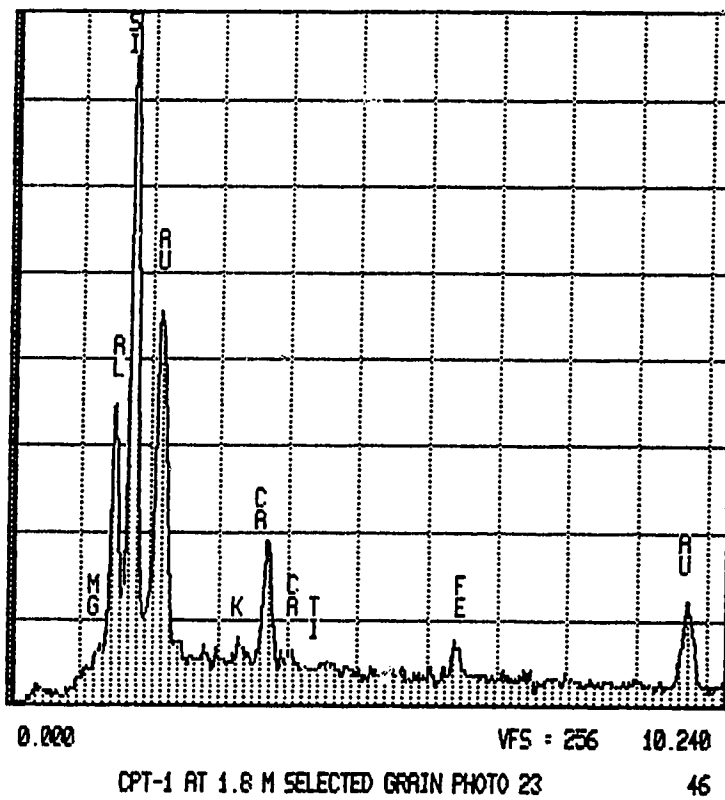
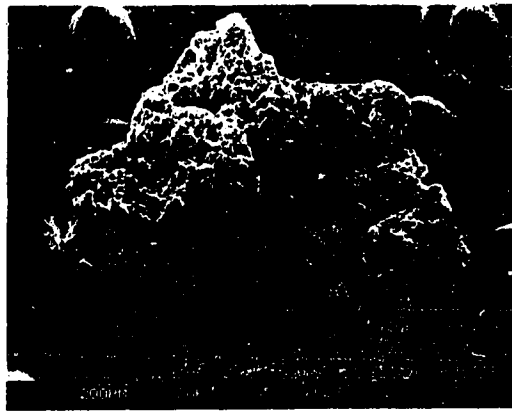


Figure 4.6: SEM photograph and qualitative mineralogy for white, porous sand grain. Analysis shows grain to be predominantly silica, aluminum and calcium.

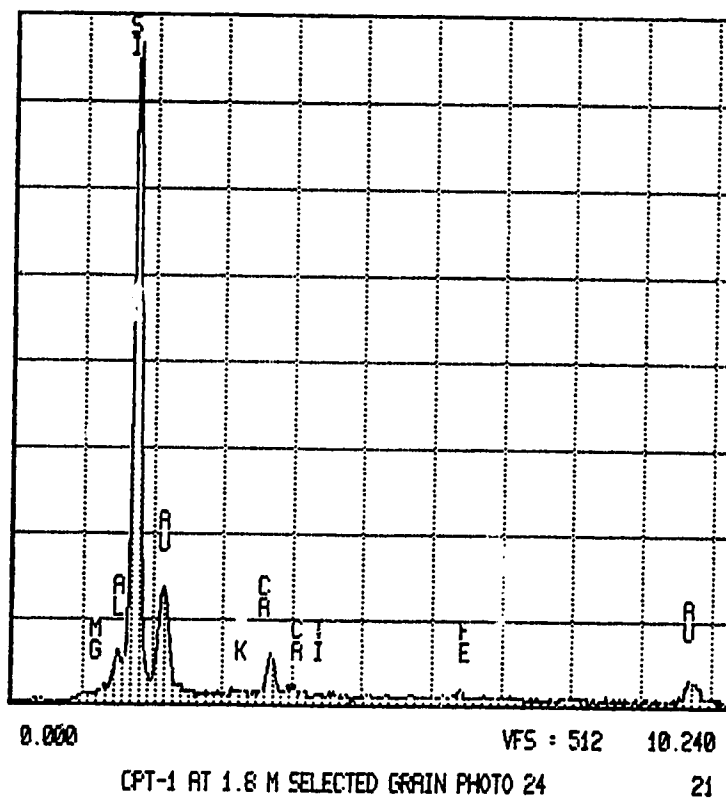


Figure 4.7: SEM photograph and qualitative mineralogy for white, blocky sand grain. Analysis shows grain to be predominantly silica.

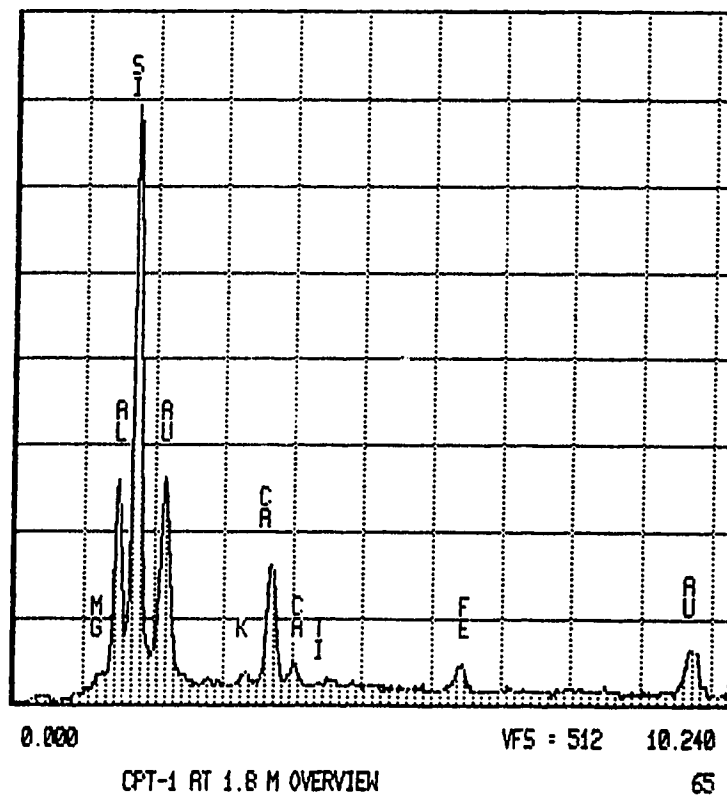
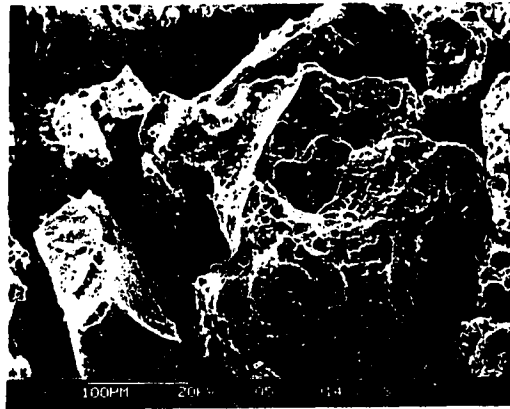


Figure 4.8: SEM photograph and qualitative mineralogy of I1 @ 1.8m. Overview analysis shows material to be predominantly silica, aluminum and calcium.

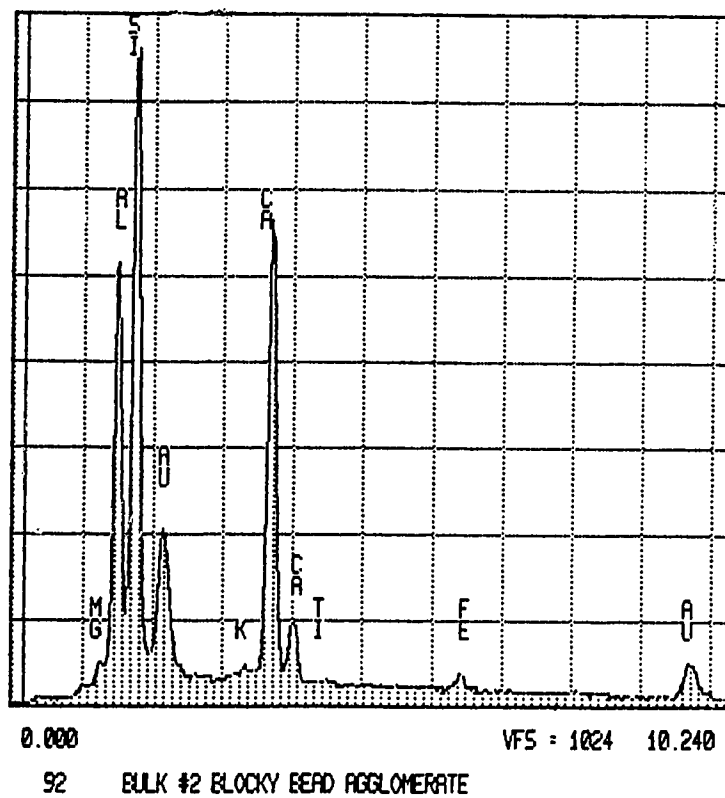
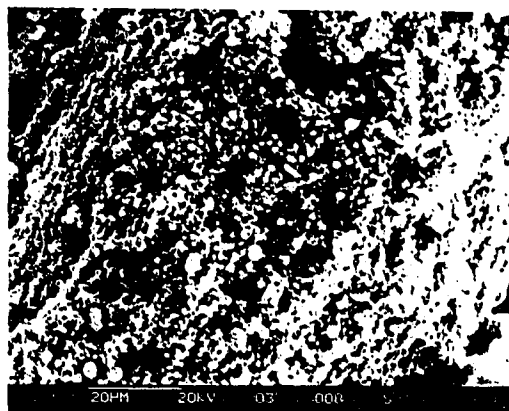


Figure 4.9: SEM photograph and qualitative mineralogy of B2. Overview analysis shows material to be predominantly silica, aluminum and calcium.

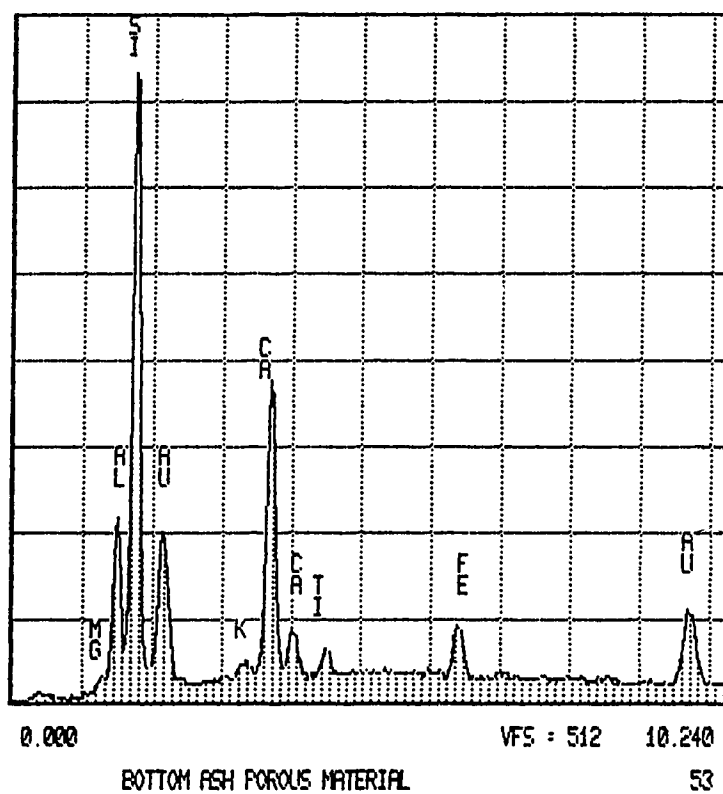
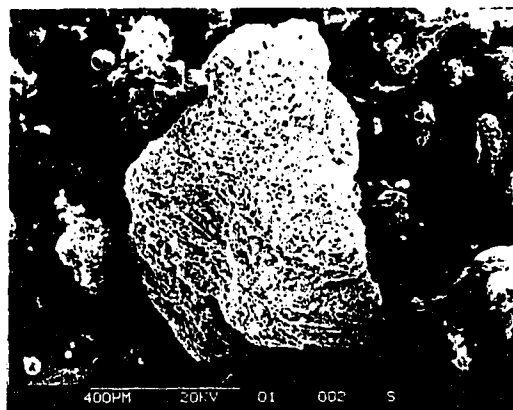


Figure 4.10: SEM photograph and qualitative mineralogy of bottom ash plant feed. Material is predominantly carbon (the large grain) with silica, aluminum and calcium making up the smaller grains.

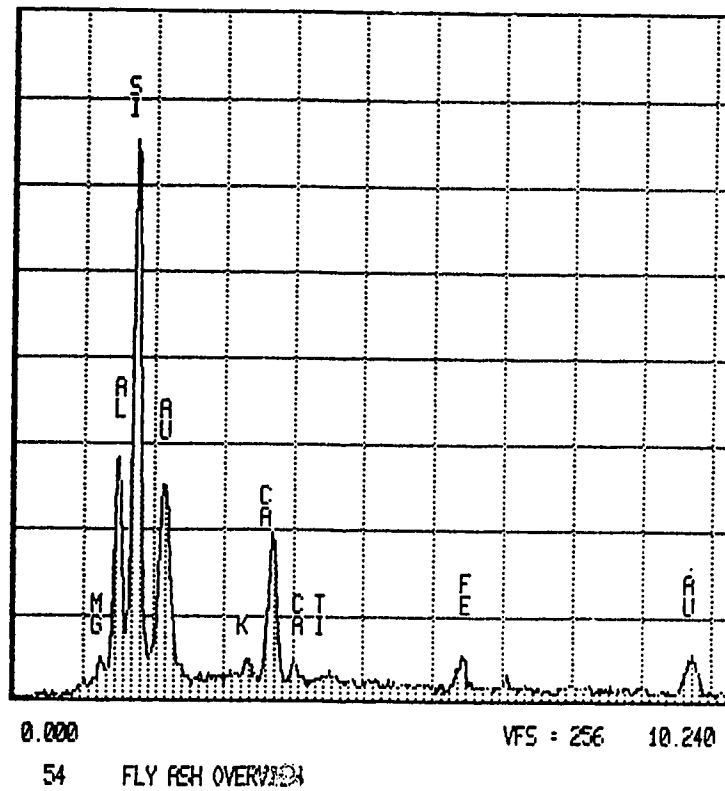
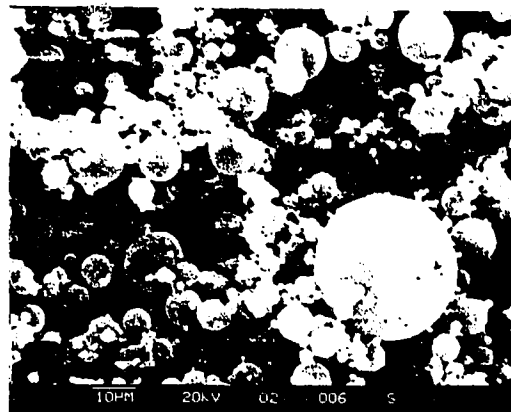


Figure 4.11: SEM photograph and qualitative mineralogy of fly ash plant feed. Overview analysis shows material to be predominantly silica, aluminum and calcium.

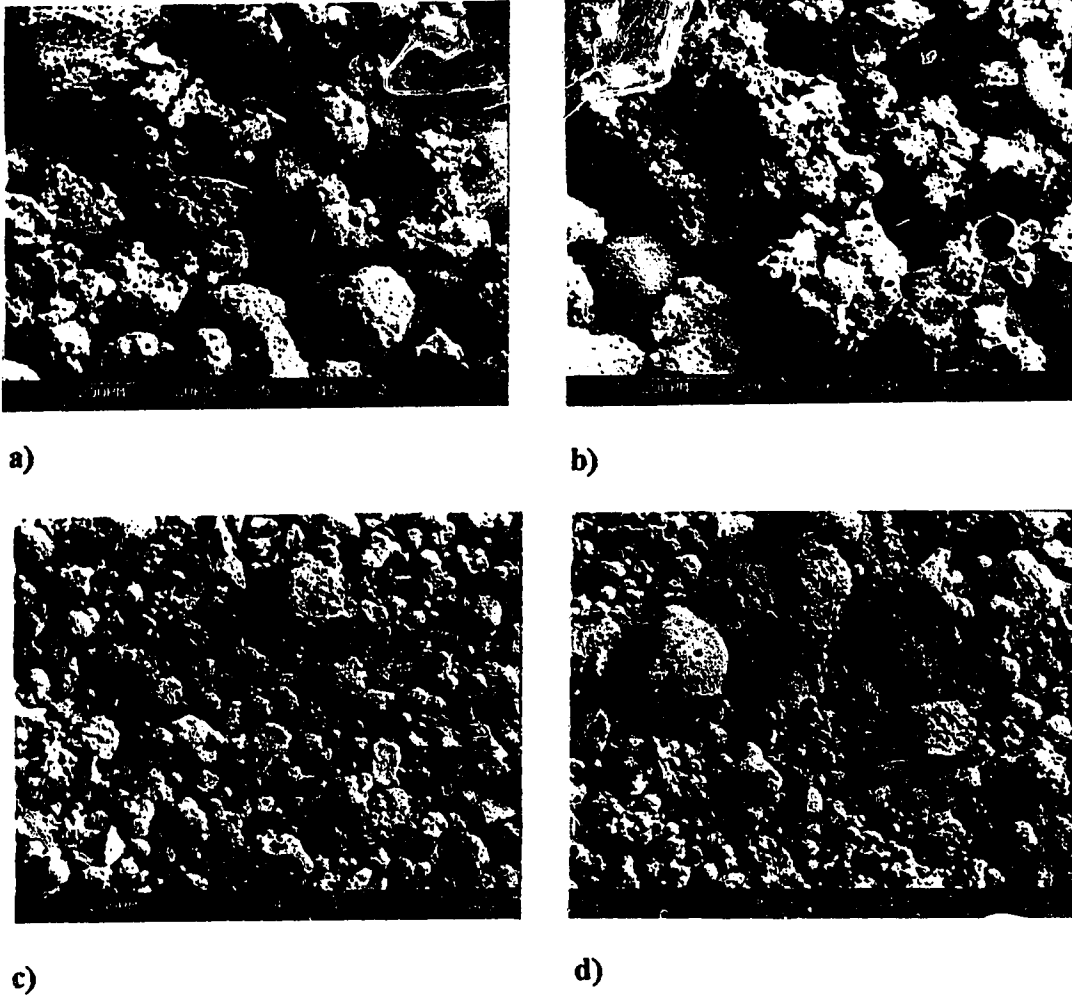


Figure 4.12: SEM photographs at 100 times magnification of a) I1 @ 1.8 m b) I1 @ 1.3 m c) B3 and d) B2.

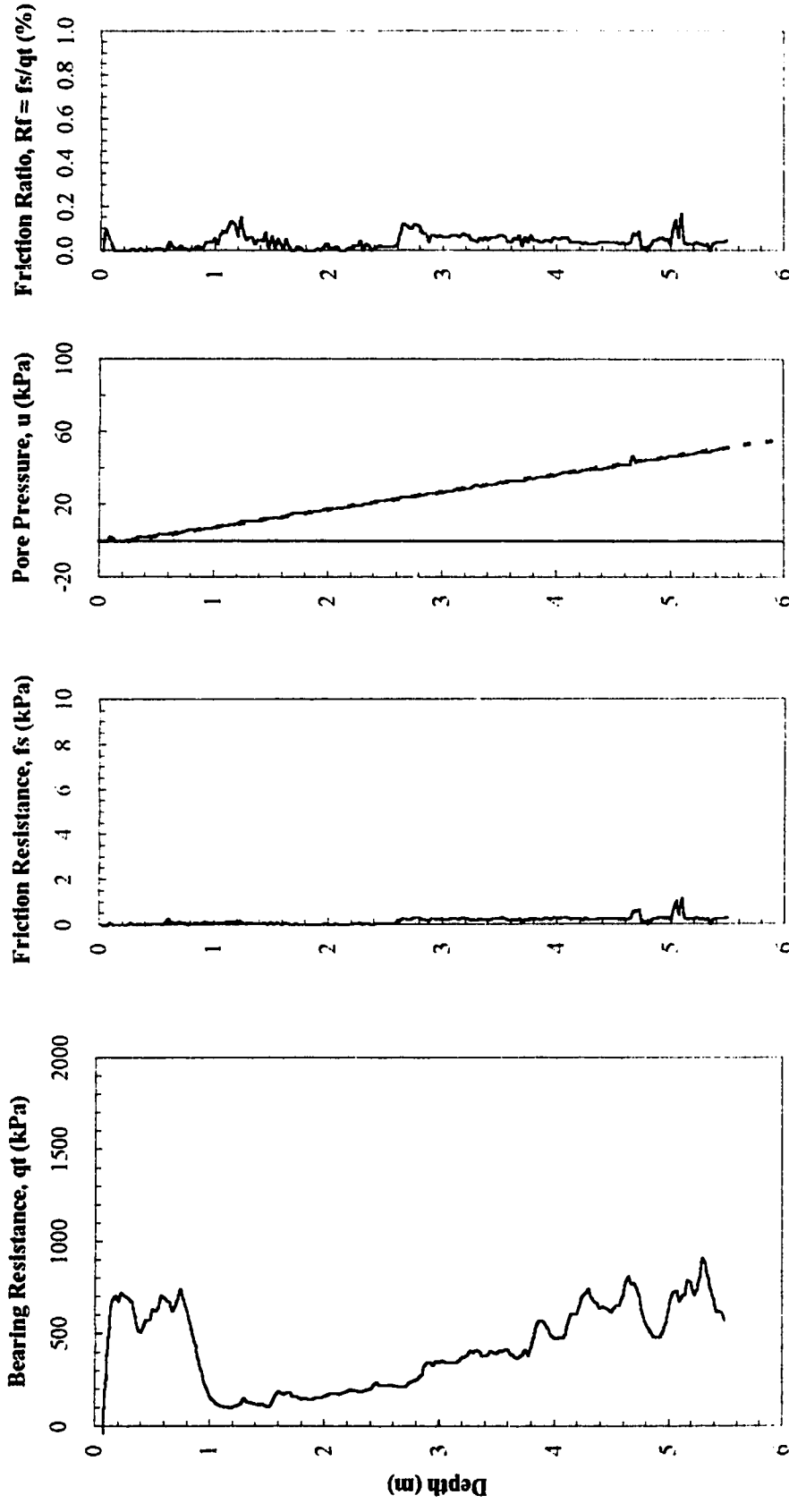


Figure 4.13: CPT data for test location I1 showing bearing resistance, friction resistance, pore pressure and friction ratio against depth.

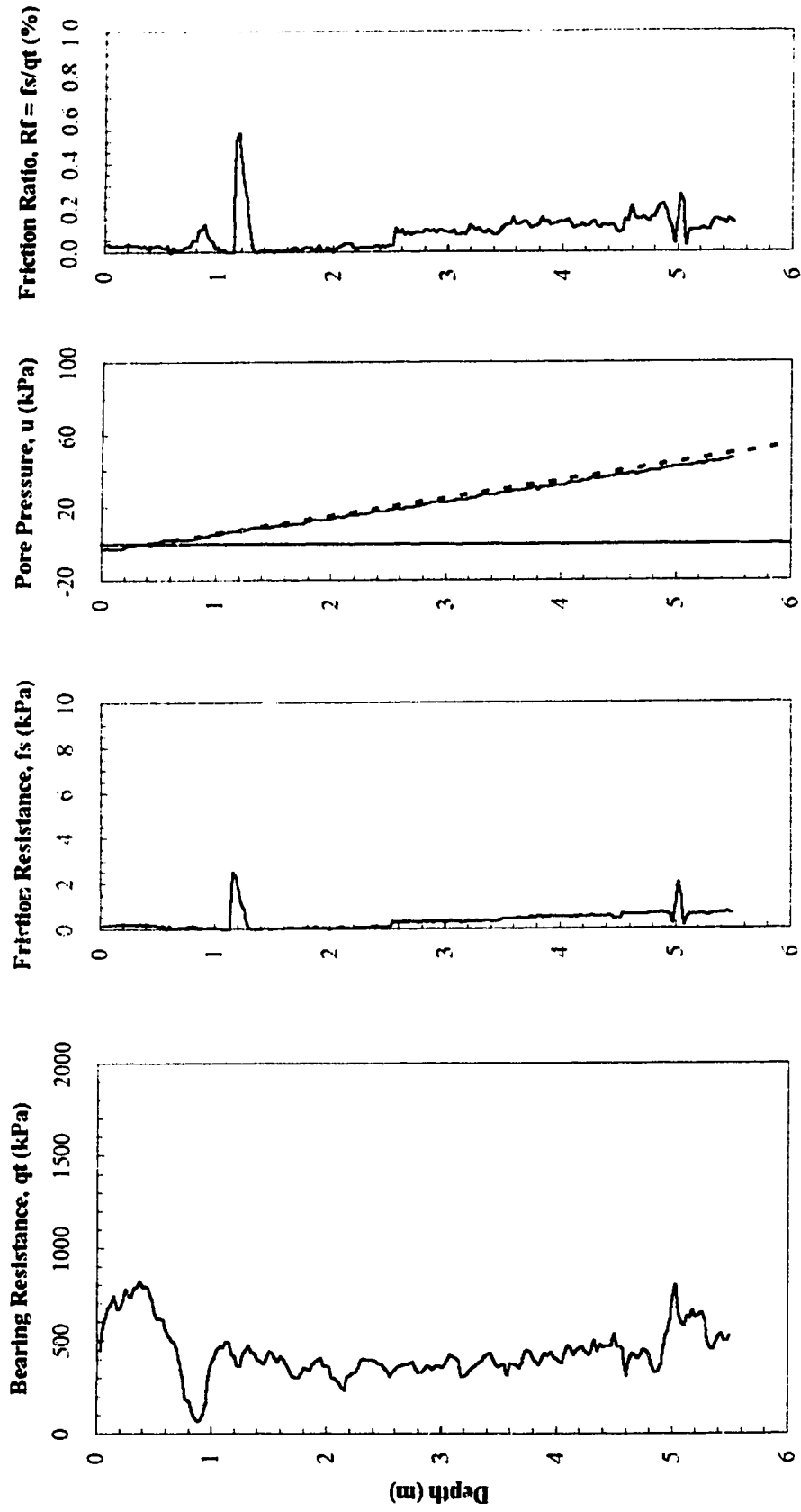


Figure 4.14: CPT data for test location 12 showing bearing resistance, friction resistance, pore pressure and friction ratio against depth.

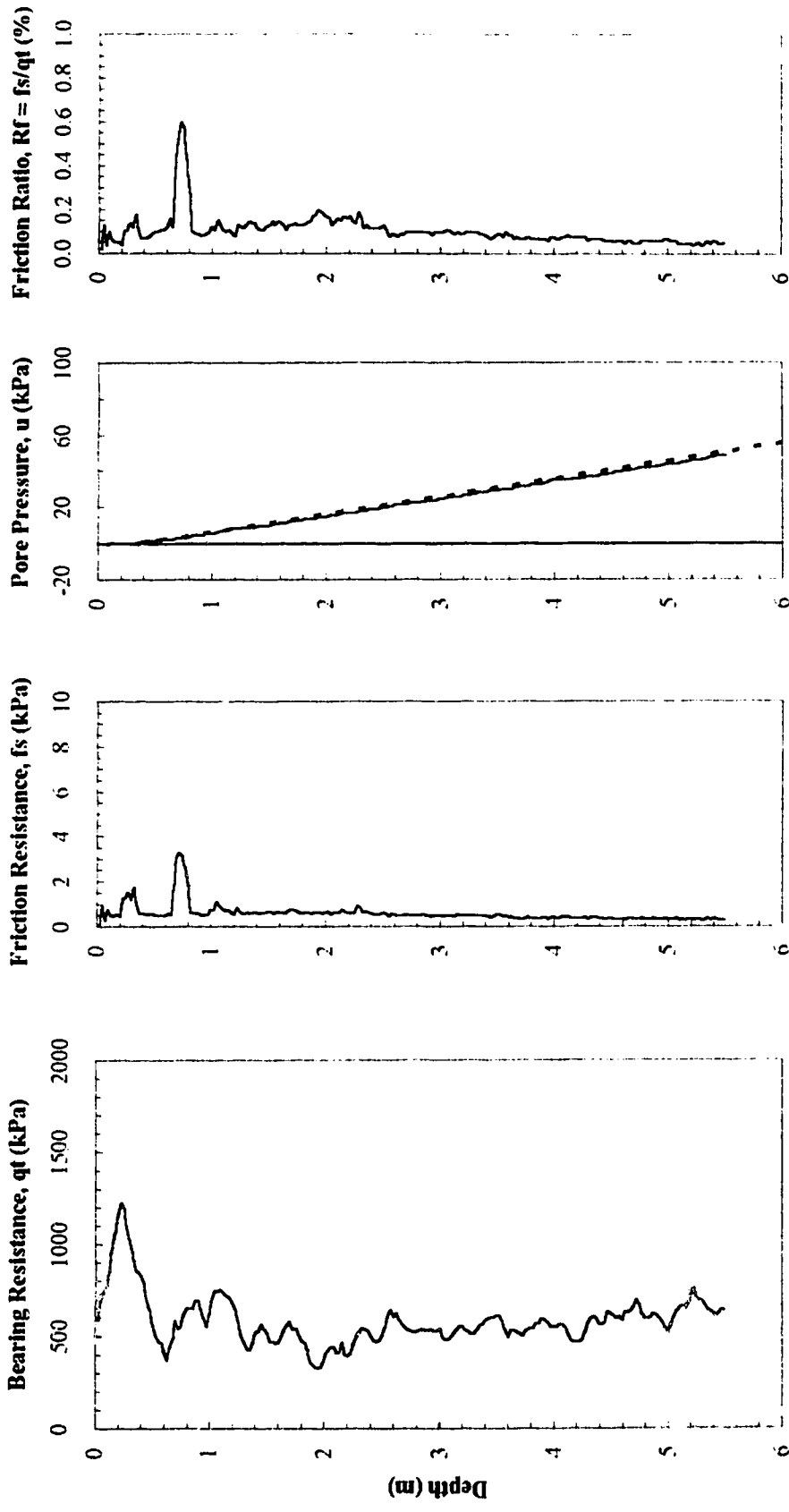


Figure 4.15: CPT data for test location I3 showing bearing resistance, friction resistance, pore pressure and friction ratio against depth.

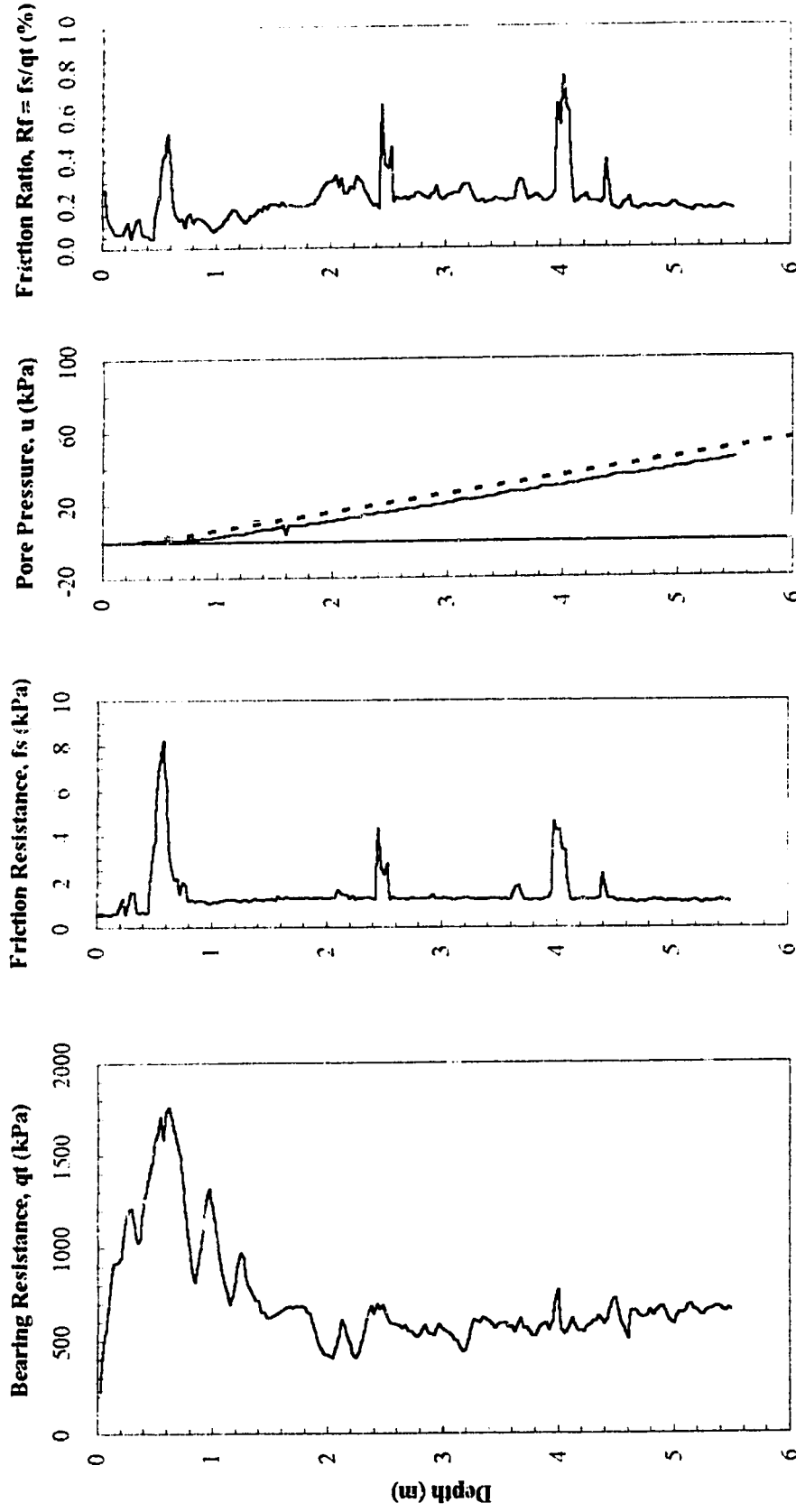


Figure 4.16: CPT data for test location 14 showing bearing resistance, friction resistance, pore pressure and friction ratio against depth.

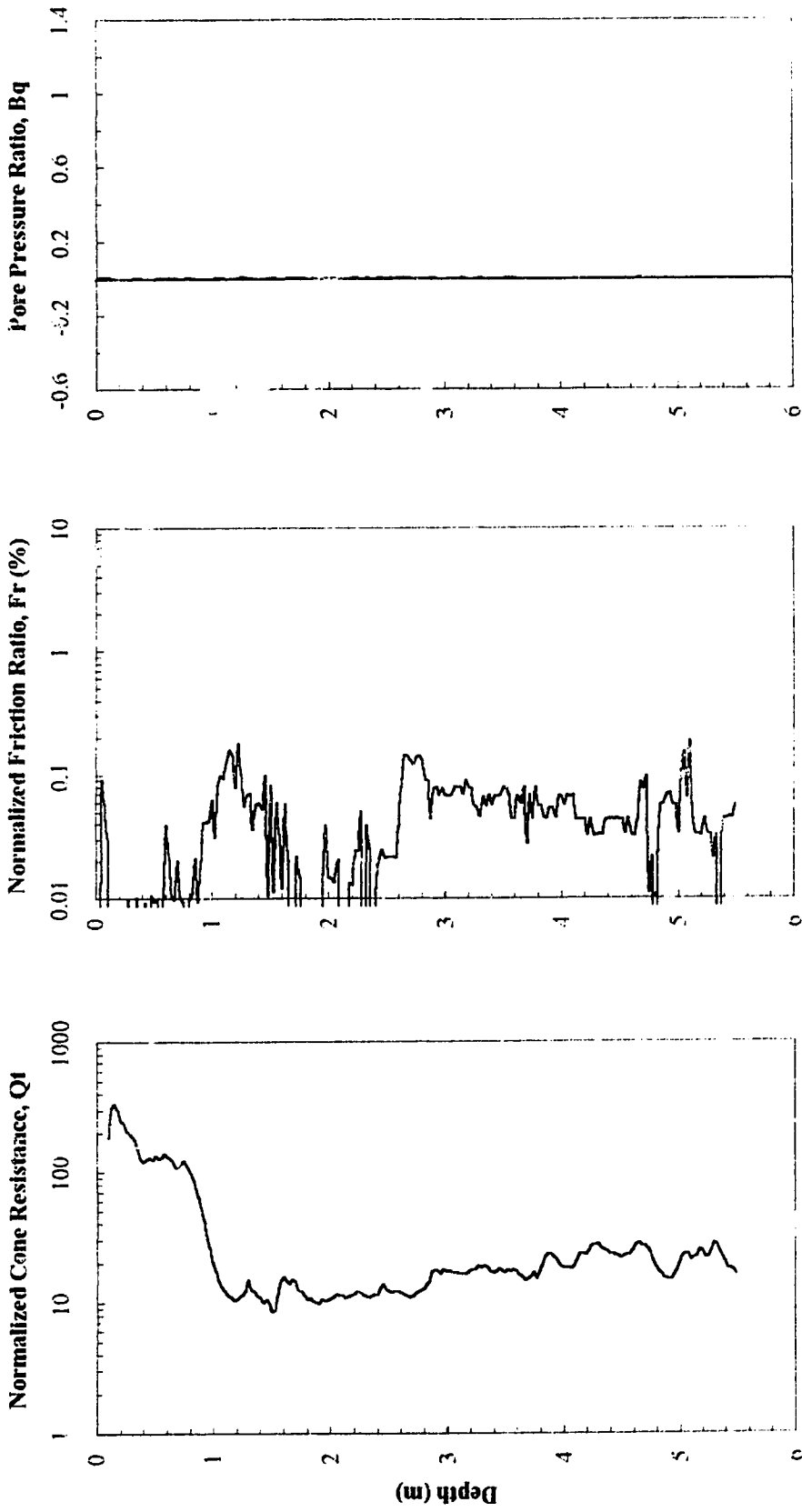


Figure 4.17: CPT data for test location 11 showing normalized cone resistance, normalized friction ratio and pore pressure ratio against depth.

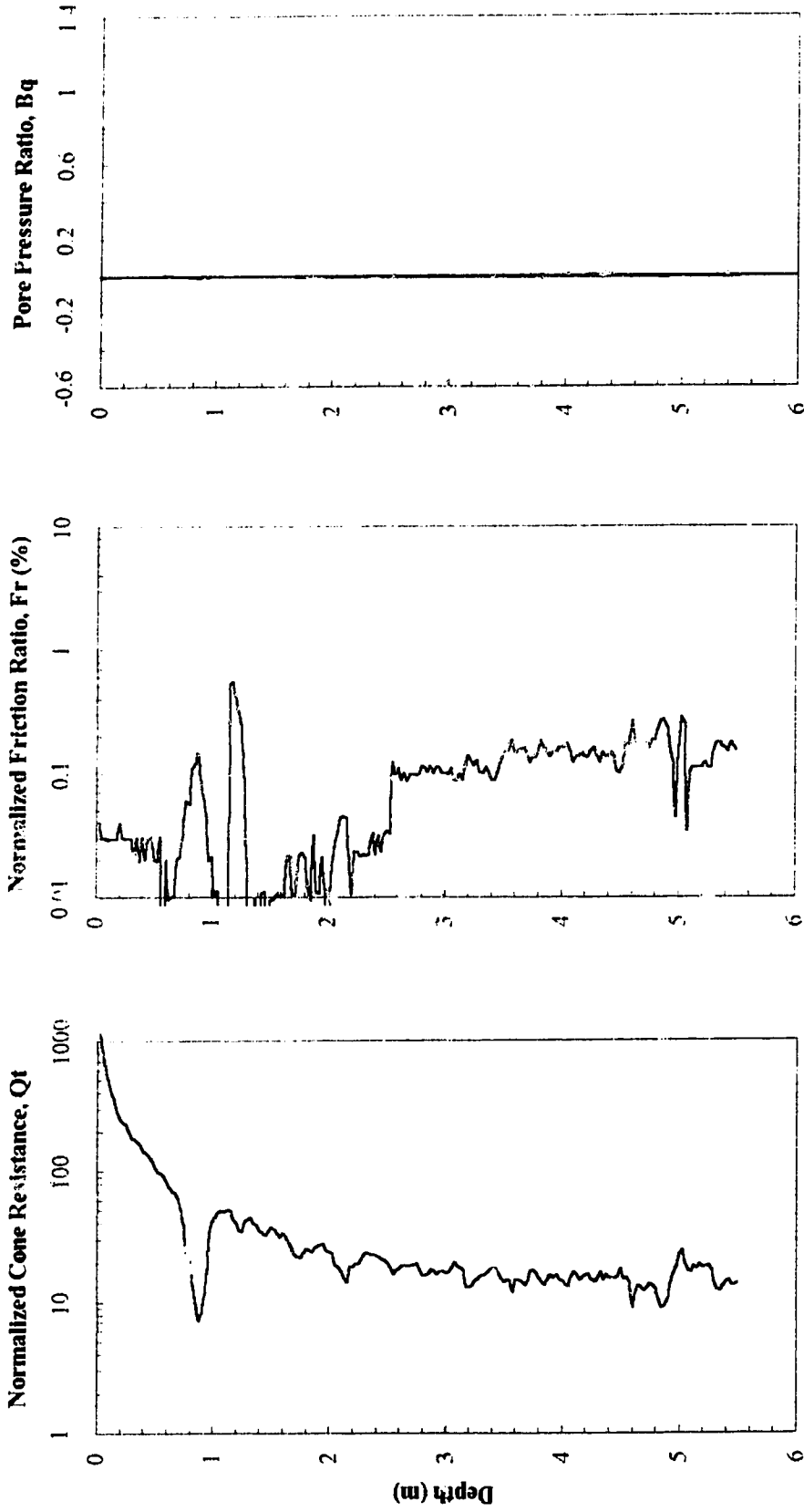


Figure 4.18: CPT data for test location 12 showing normalized cone resistance, normalized friction ratio and pore pressure ratio against depth.

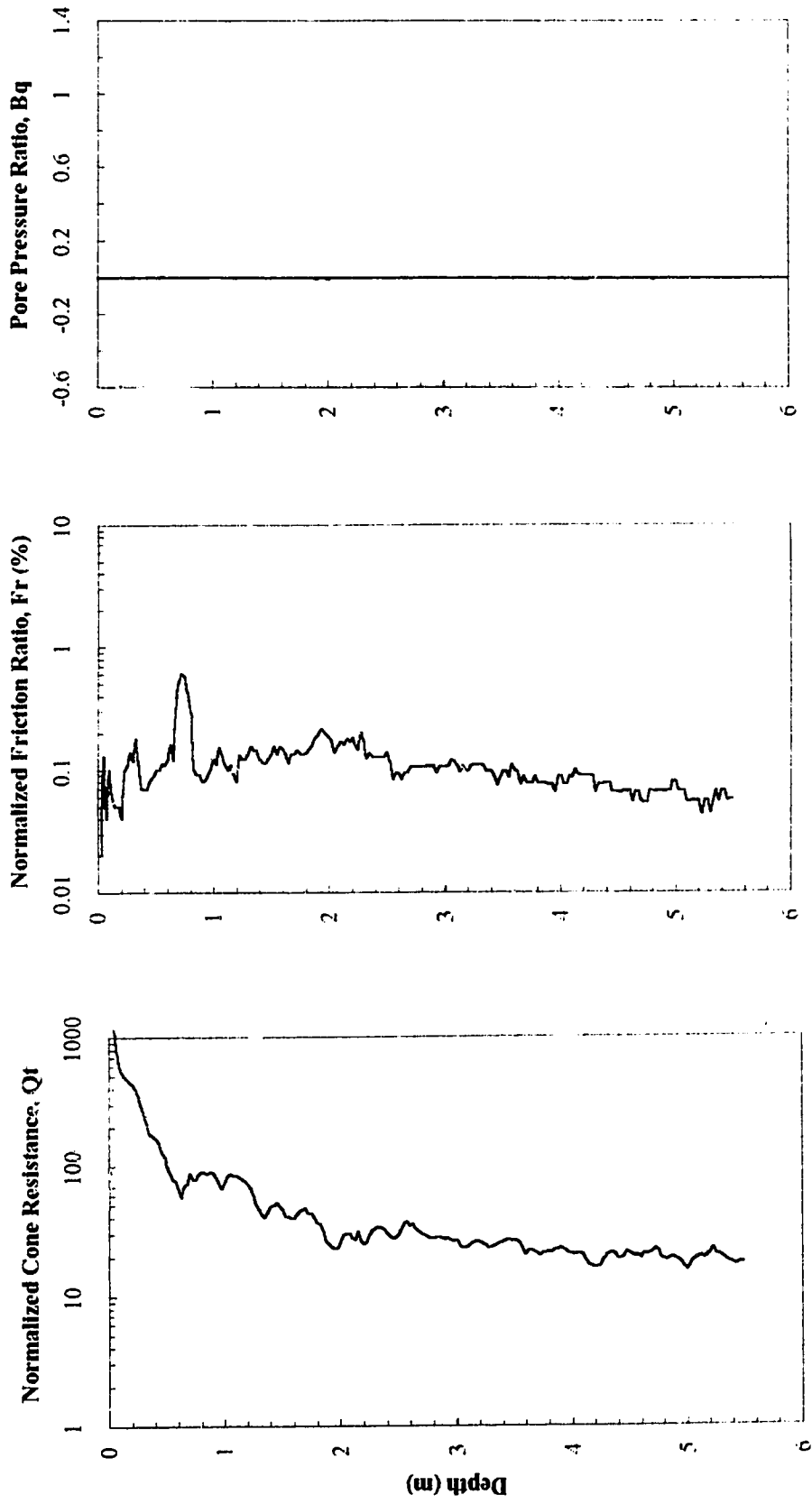


Figure 4.19: CPT data for test location I3 showing normalized cone resistance, normalized friction ratio and pore pressure ratio against depth.

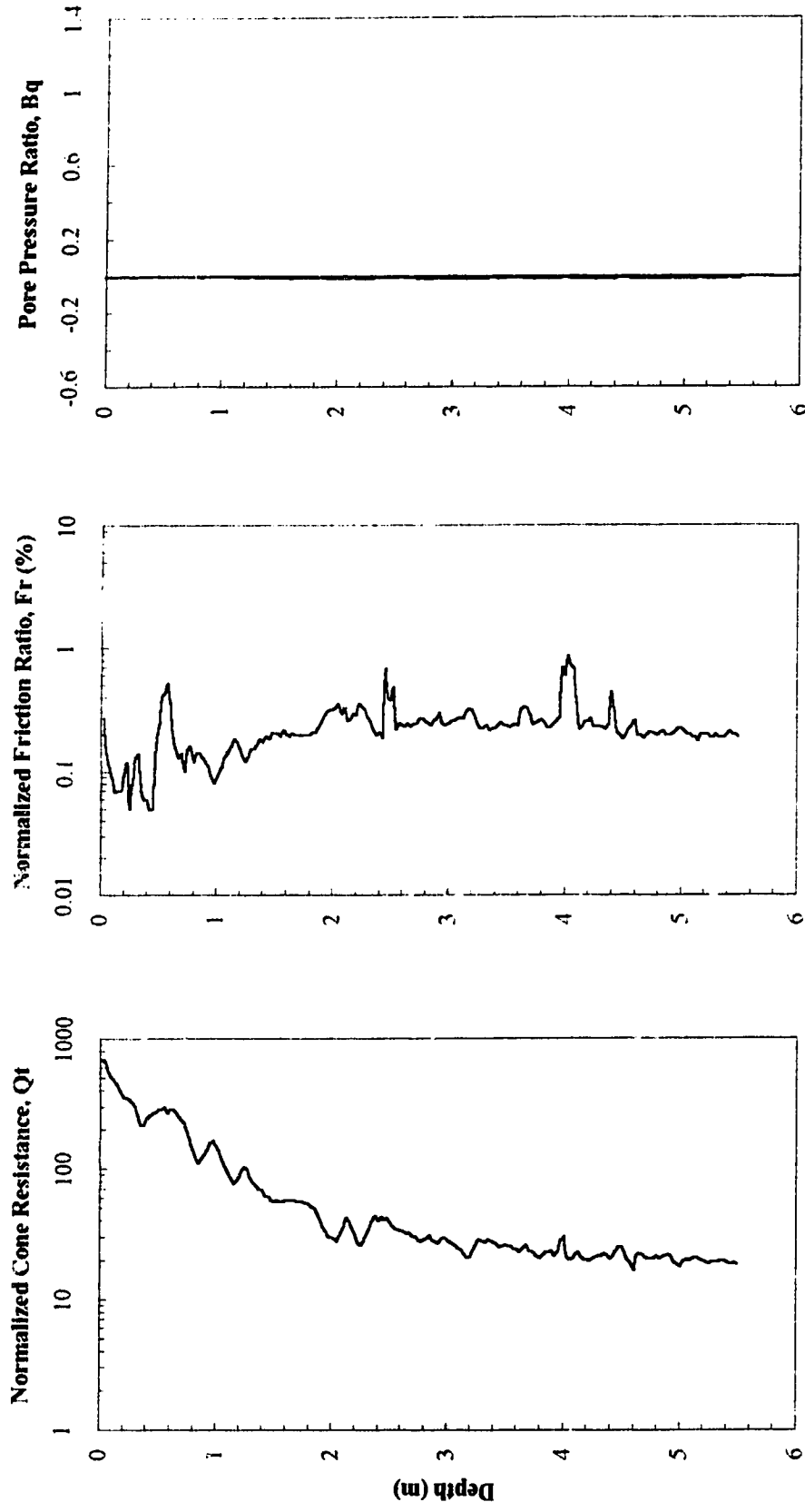


Figure 4.20: CPT data for test location I4 showing normalized cone resistance, normalized friction ratio and pore pressure ratio against depth.

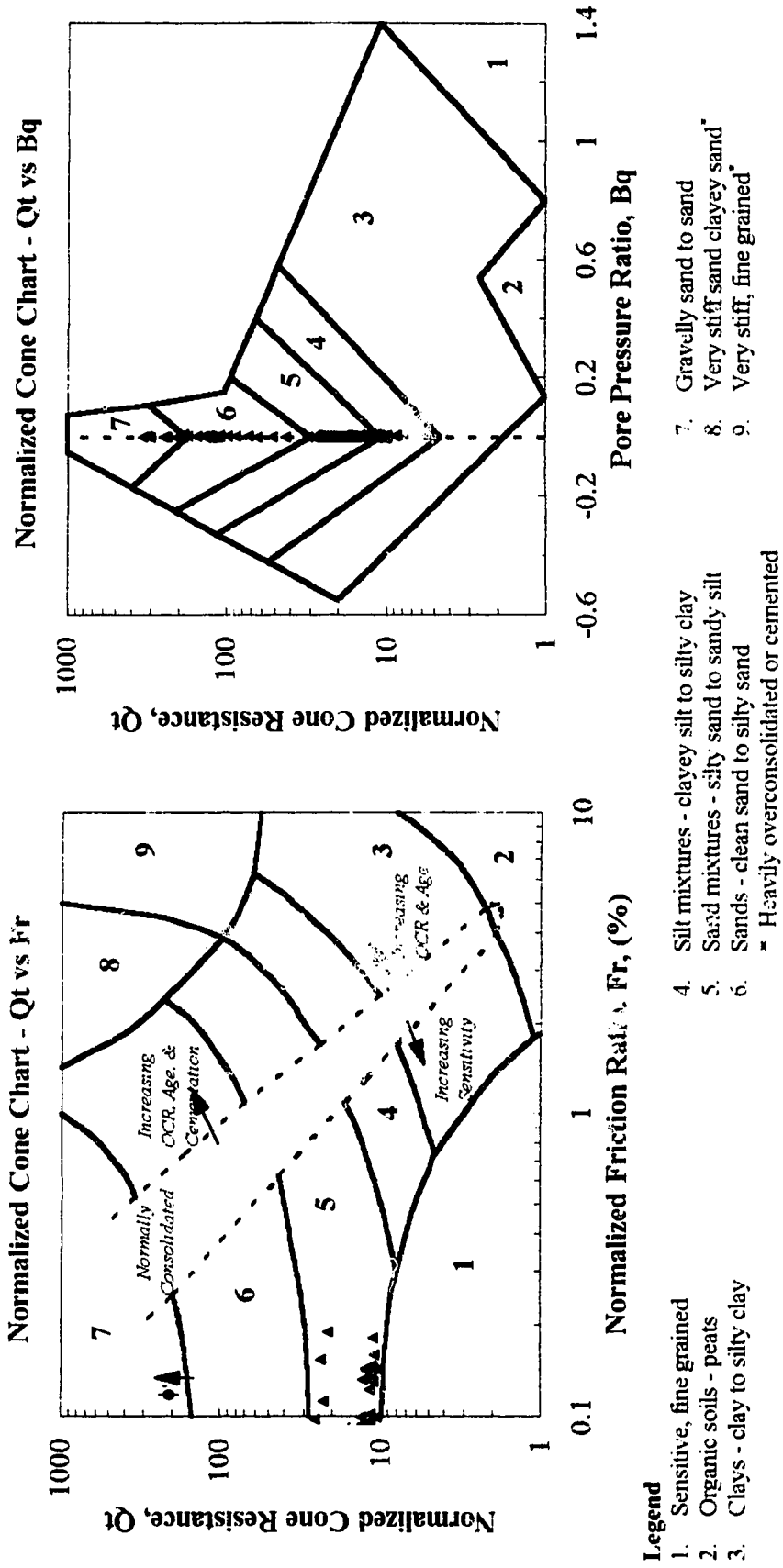


Figure 4.21: Classification based on CPT data for test location 11 showing normalized cone resistance against normalized friction ratio and normalized cone resistance against pore pressure ratio.

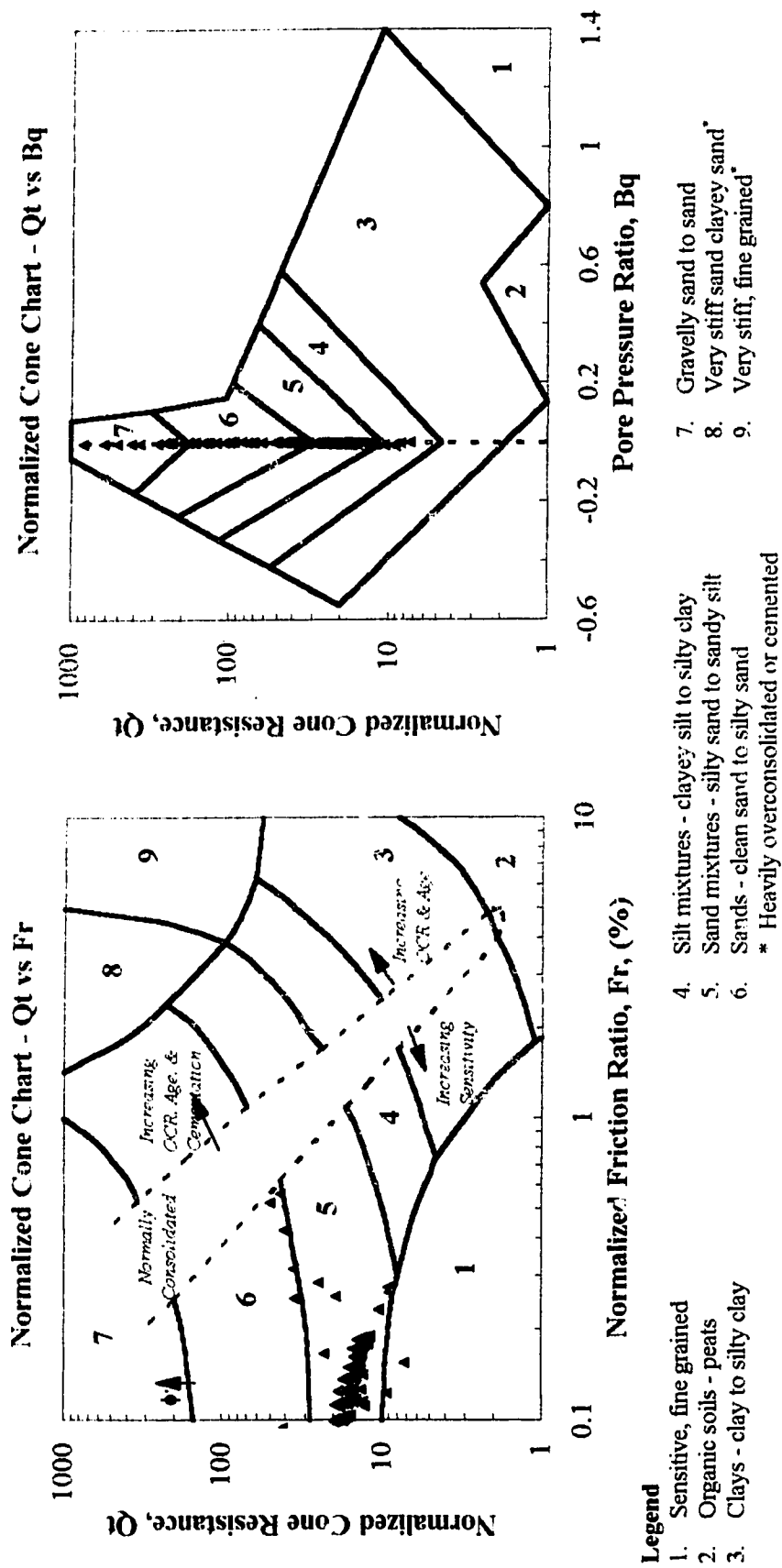


Figure 4.22: Classification based on CPT data for test location I2 showing normalized cone resistance against normalized friction ratio and normalized cone resistance against pore pressure ratio.

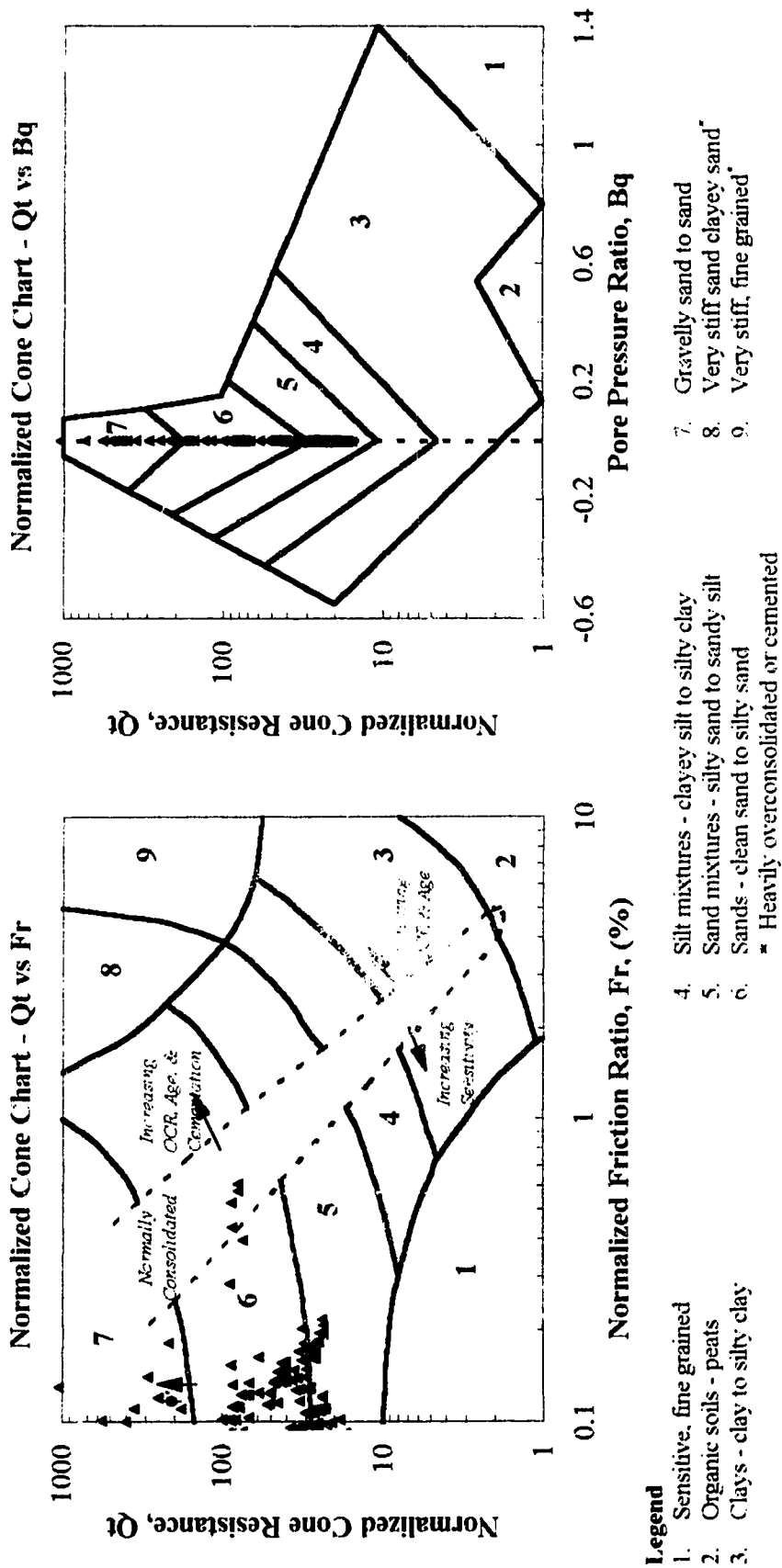


Figure 4.23: Classification based on CPT data for test location I3 showing normalized cone resistance against normalized friction ratio and normalized cone resistance against pore pressure ratio.

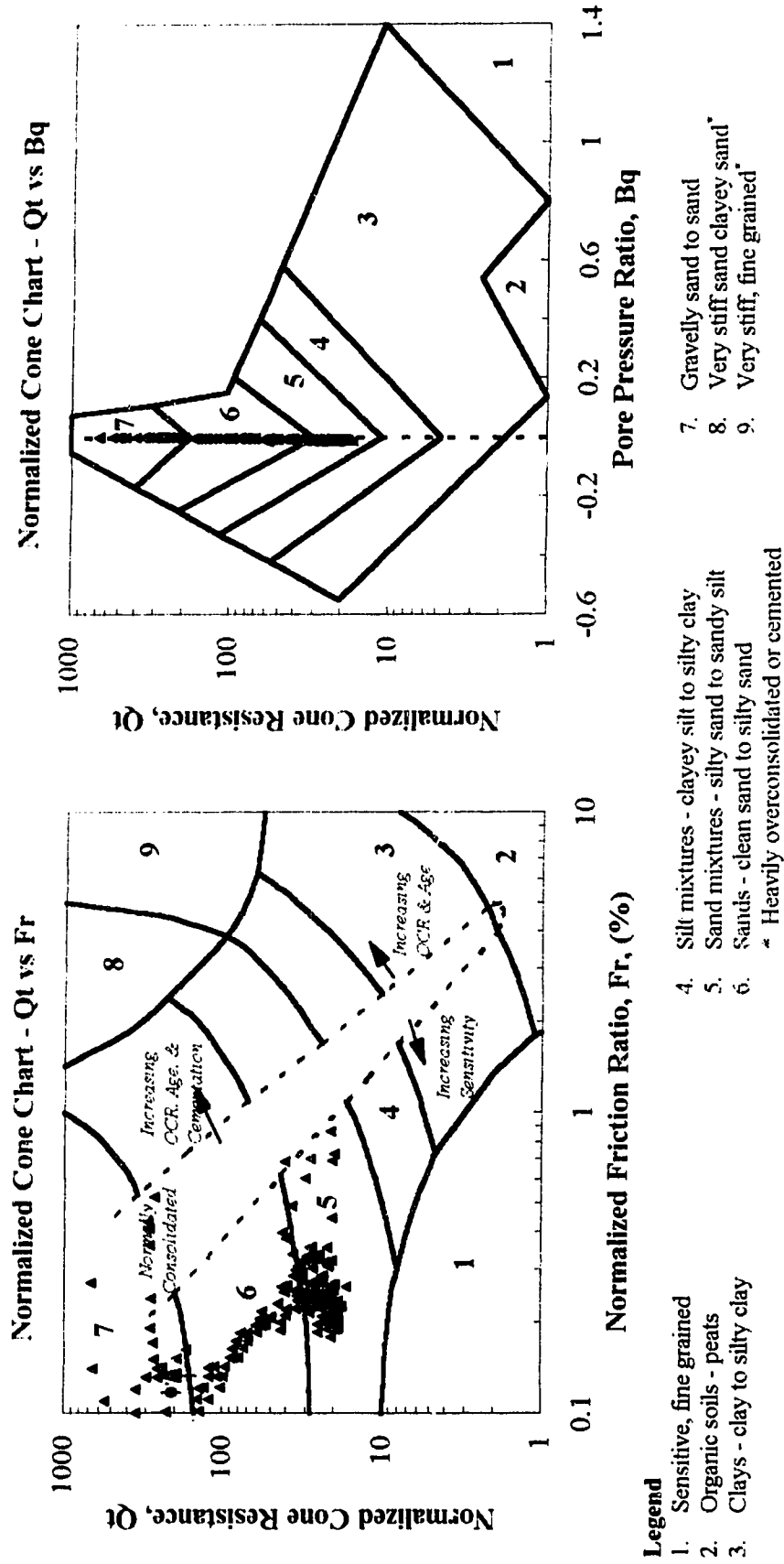
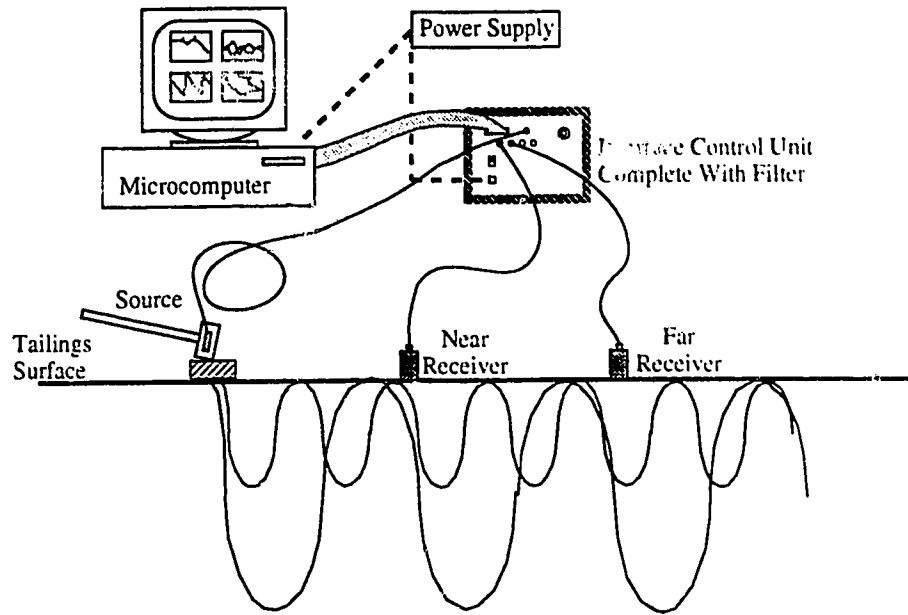


Figure 4.24: Classification based on CPT data for test location I4 showing normalized cone resistance against normalized friction ratio and normalized cone resistance against pore pressure ratio.

Spectral Analysis of Surface Waves (SASW)



- Receivers Monitor Passage of Waves Generated by Source
- Time Signal Transformed to Frequency Domain Using Fast Fourier Transform Algorithm
- Following Five Samples of Input Signals, Phase Velocities and Wavelengths Are Output to Form Dispersion Curve

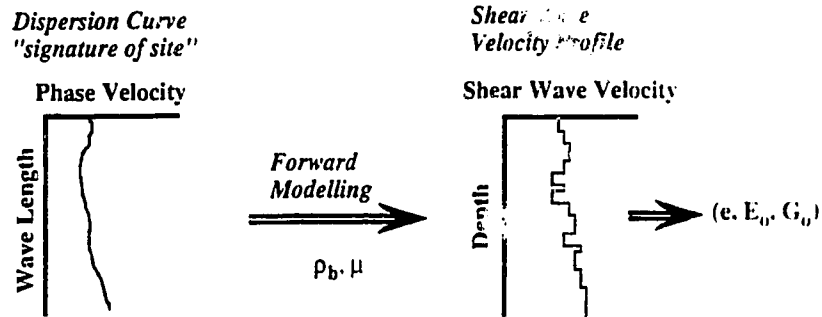


Figure 4.25: Schematic of Spectral Analysis of Surface Waves (SASW) testing and data interpretation (Stahl, 1995b).

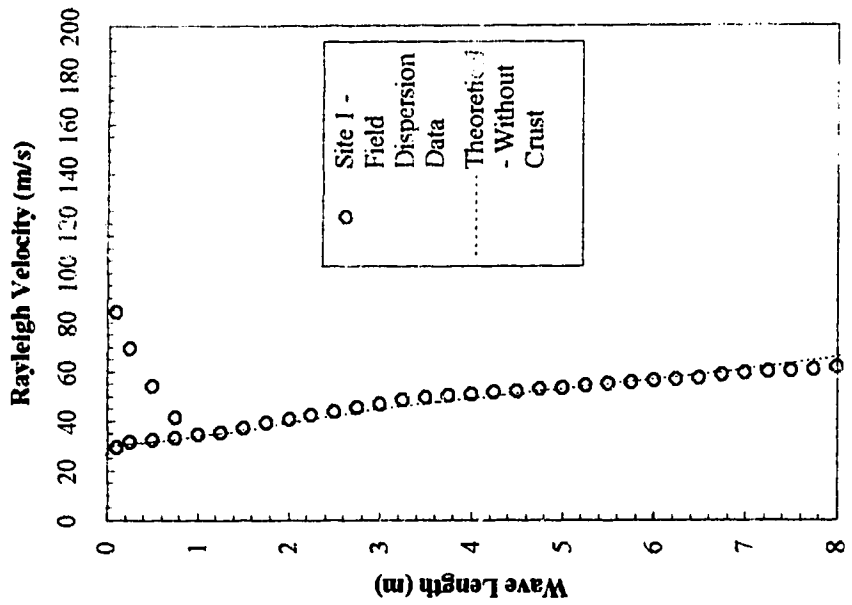
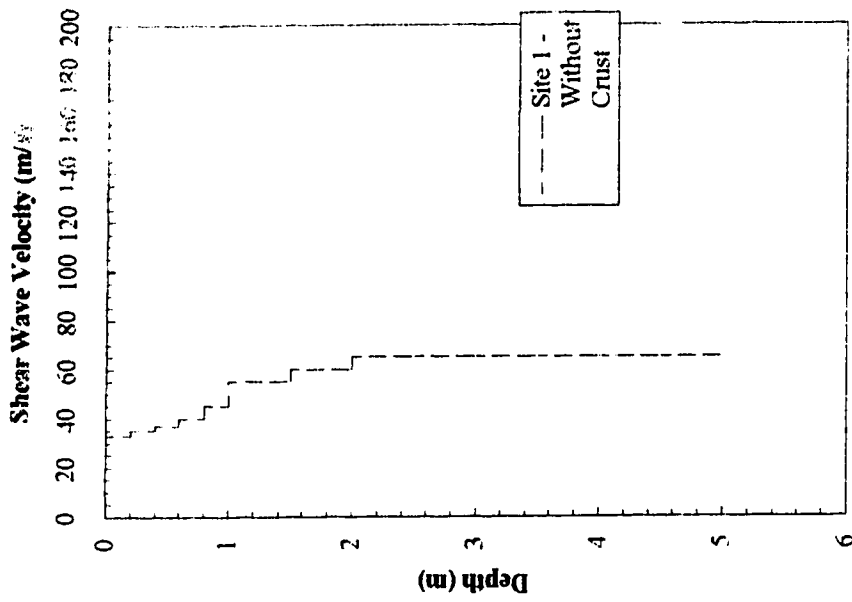


Figure 4.26: SASW data for test location I1 showing Rayleigh velocity against wavelength and shear wave velocity against depth.

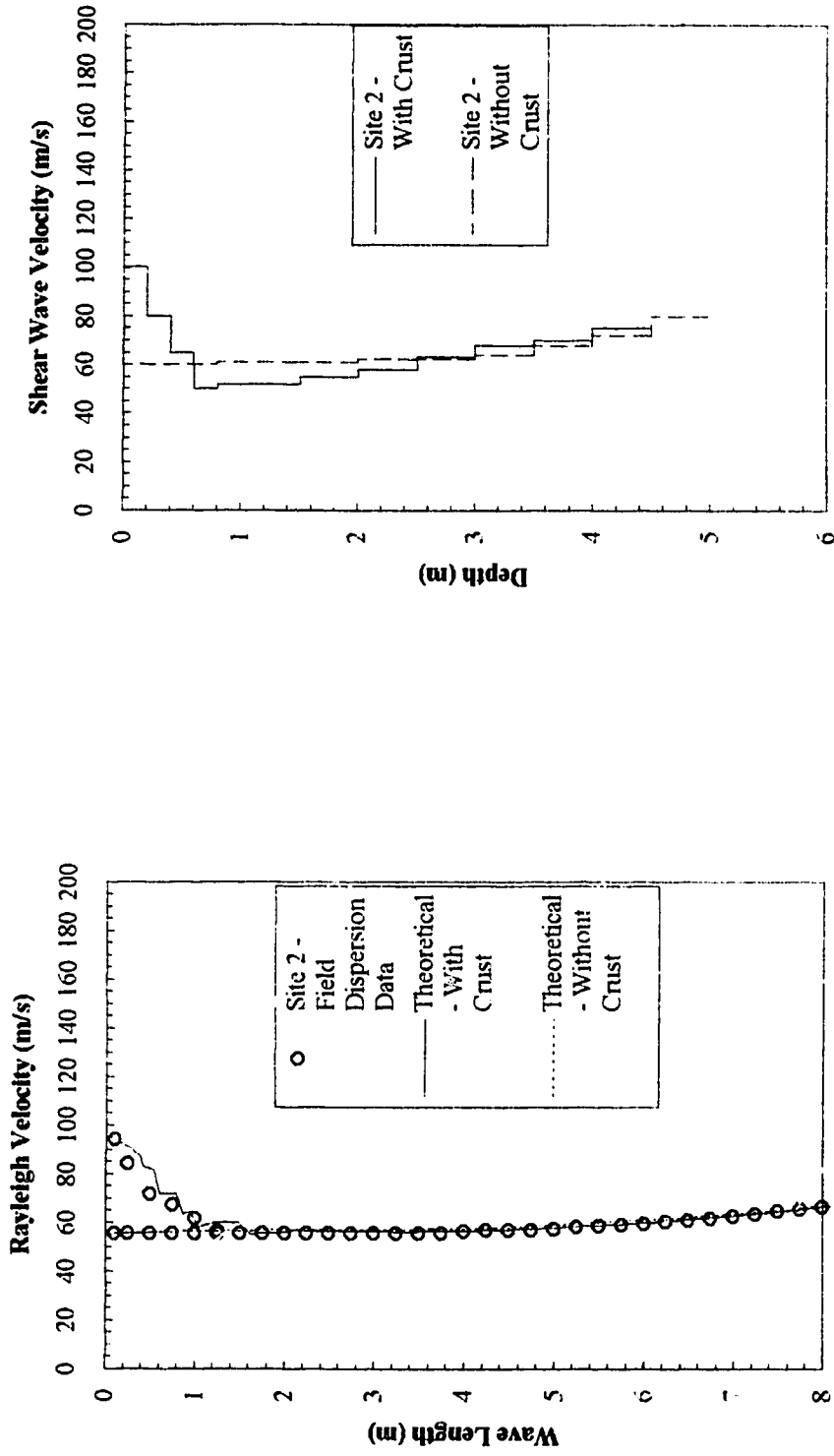


Figure 4.27: SASW data for test location I2 showing Rayleigh velocity against wavelength and shear wave velocity against depth.

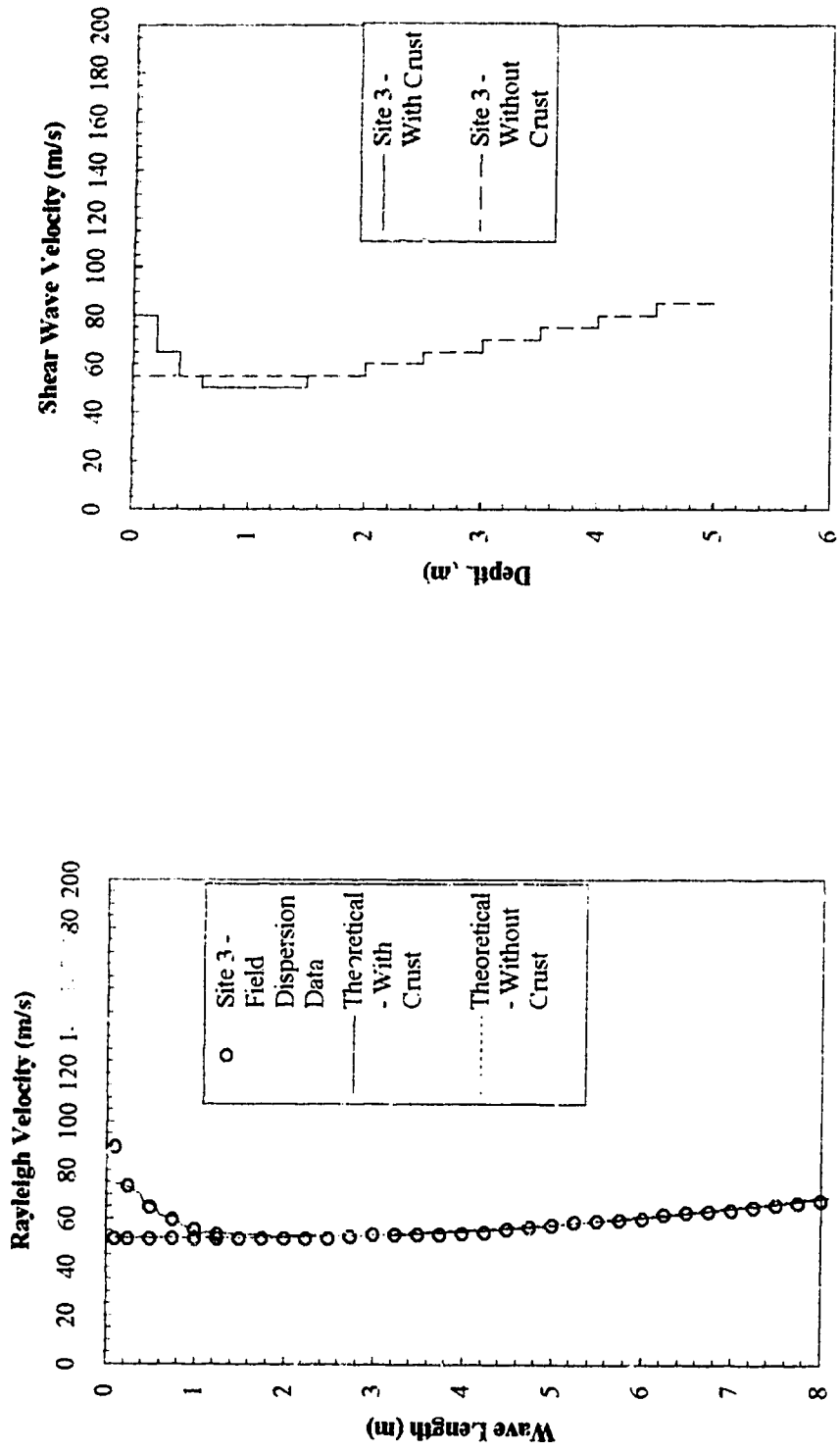


Figure 4.28: SASW data for test location 13 showing Rayleigh velocity against wavelength and shear wave velocity against depth.

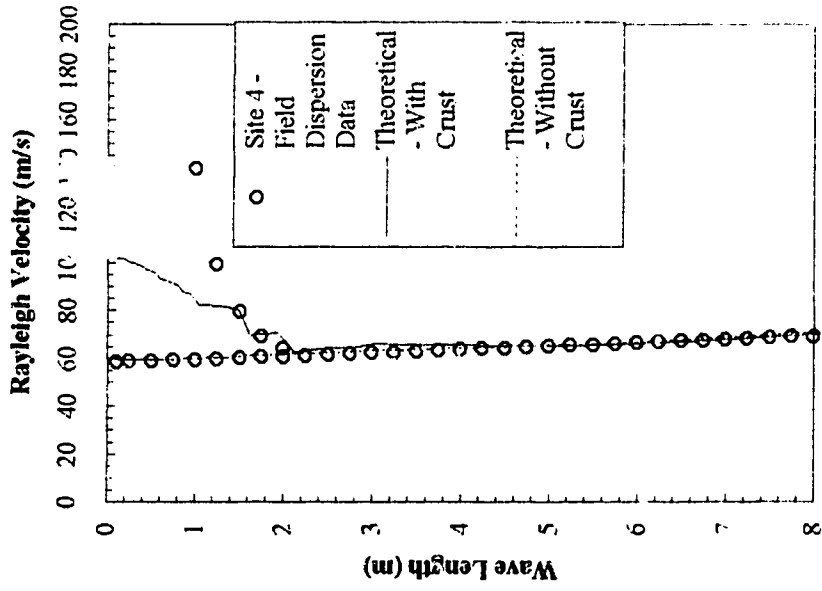
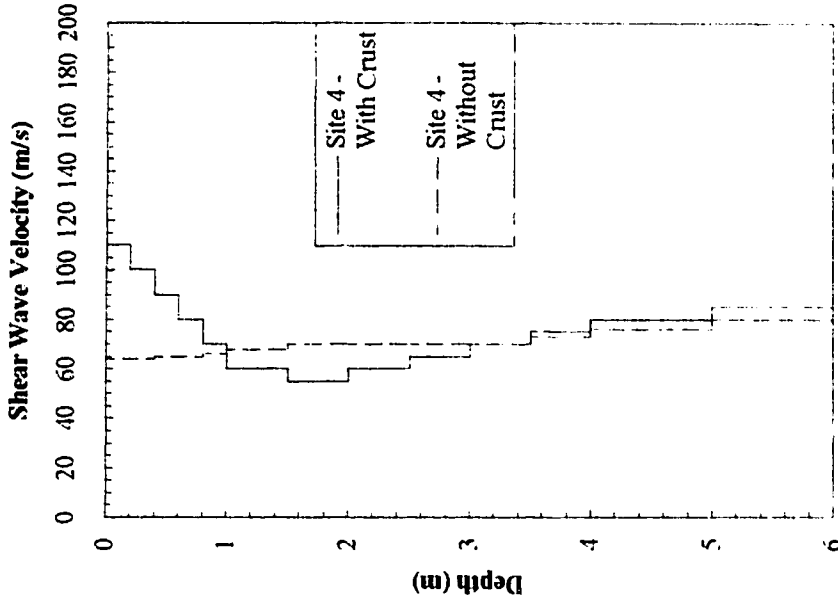


Figure 4.29: SASW data for test location 14 showing Rayleigh velocity against wavelength and shear wave velocity against depth.

5. Triaxial Testing With Shear Wave Velocity Measurement

Triaxial testing with shear wave velocity measurements was conducted in order to determine the USS characteristics and $e-p'-V_s$ relationship for Wabamun sand.

5.1. Triaxial Testing Procedure

Triaxial testing with shear wave velocity measurement was conducted according to procedures developed at the University of Alberta by Sasitharan (1994), Cunning (1994), Chillarige (1995) and others. The specific procedures used for the testing of the Wabamun sand are described in detail in Appendix A.

5.1.1. Testing Equipment

The triaxial testing program was conducted using a modified triaxial testing cell in a modified Wykeham Farrance loading frame. The modifications to the cell included the use of an internal load cell to eliminate the measurement of rod friction, a removable top cap to allow assembly of the cell around the sample and load cell with minimal disturbance to the sample, and single protruding bender elements in the loading head and base pedestal to allow for the measurement of shear wave velocity. Modifications to the loading frame consisted of a facility to apply dead loads to the loading ram to compensate for unequal end area effects and allow for samples to be isotropically consolidated. A schematic diagram of the test setup (after Cunning, 1994) is shown in figure 5.1. A schematic of the protruding bender element system developed by Sasitharan (1994) is shown in figure 5.2.

5.1.2. Sample Preparation

All samples were prepared by the method of moist tamping. This technique produces the loosest possible structure in reconstituted soil samples (Ishihara, 1993). The technique also eliminates the problem of segregation of fines that can occur in the water pluviation method (Cunning, 1994).

5.1.3. Calculation of Void Ratio

Void ratio after sample preparation can easily be determined from the sample measurements and soil mass. Changes in void ratio following sample preparation were calculated based on the volume changes during saturation and consolidation. As volume changes during saturation cannot be measured directly, they must be calculated by other means. Due to the difficulty in using girth belts on the very loose samples tested in this research, it was necessary to assume elastic response and apply a simple elastic approach to evaluating the volumetric strain:

$$\varepsilon_v / \varepsilon_a = 3 \quad [9]$$

where: ε_v = volumetric strain (%)
 ε_a = axial strain (%)

After preparation, the samples were saturated using the procedure described in Appendix A until either Skempton's B parameter exceeded 0.95 or consecutive equal measurements of B were attained. Note that in a porous material such as the Wabamun sand, a B value of one can indicate that only the macropores are saturated, and that some further saturation of micropores could take place due to consolidation stresses. However for the purposes of this work, the criteria described above were assumed to indicate full saturation.

Following saturation, the samples were consolidated in increments of 25, 50, or 100 kPa. During consolidation, the void ratio for the sample was calculated using the following equation from Cuning (1994):

$$e = \frac{G_s * (V_{init} - \Delta V_{sat} - \Delta V_{consol.} - \Delta V_{mem.corr.}) * \rho_w}{M_s} - 1 \quad [10]$$

where: G_s = Specific gravity of the solids
 M_s = The mass of the solids, g
 ρ_w = The density of water, 1 g/cm³
 V_{init} = The volume after sample preparation, cm³
 ΔV_{sat} = The calculated volume change during saturation, cm³

- $\Delta V_{\text{consol.}}$ = The measured volume change during consolidation, cm^3
 $\Delta V_{\text{mem.corr.}}$ = The change in volume during membrane penetration, cm^3

The change in volume due to membrane penetration is included in the equation for completeness. Vaid and Negussy (1984) point out that the penetration of the membrane into the soil voids must be accounted for in the calculation of void ratio. They suggest a value of $0.0048 \text{ cm}^3/\text{cm}^2$ per log cycle of effective confining stress for a mean grain size (D_{50}) of 0.35 mm. This correction is neglected in this research first because it represents a void ratio change of less than ± 0.005 at the highest effective confining stress encountered, and second because the relationship between membrane penetration and grain crushing is not understood.

5.1.4. Shear Wave Velocity Measurement

Shear wave velocity in the samples was measured using the protruding bender element system developed by Sasitharan (1994), Figure 5.2. A Wavetek 148 A-20 AM/FM/PM generator, a Kistler 504 Dual Mode Amplifier, a Phillips PM 3365A 100 MHz 100 MS/s oscilloscope and a Hewlett Packard Color Pro pen plotter were used to generate and record the shear waves.

The bender element protrudes into the sample approximately 10 mm. When shear wave velocity measurements are to be taken, the top source element is excited with a ± 15 volt DC, 20 Hz square wave produced by the Wavetek generator. This causes the piezoceramic material in the bender element to alternately expand and contract, creating back and forth motion of the cantilever portion of the bender element, and a shear wave in the sample. This shear wave is transmitted through the soil skeleton to the base receiver element. This element oscillates, producing an electrical signal, which is picked up by the Kistler Dual Mode Amplifier, and enhanced for display on the oscilloscope. Both waves are displayed on the oscilloscope, allowing for the travel time (Δt) in seconds to be determined using the first pulse arrival method. Figure 5.3 shows a typical oscilloscope output trace, with both the generator and received wave, as well as the frequency and time

difference. From the time difference and the known separation of the bender element tips, the shear wave velocity is determined.

The measurement of shear wave velocity in all of the triaxial tests was not possible due to problems with equipment failure. However, sufficient measurements were obtained to allow extrapolation of the existing database on other sands.

5.2. Material Tested

After careful review of the index testing and SEM work, it was concluded that either bulk sample #2 or bulk sample #3 would be acceptable to represent the in-situ material. However, after splitting each sample on the #10 sieve to achieve a sample gradation that could be tested in the available apparatus, it was concluded that neither sample was sufficiently large to allow the completion of an entire testing program. The samples were therefore combined to form a bulk aggregate sample with index properties similar to that of the original samples. Table 5.1 shows the index properties for the bulk aggregate sample, while figure 5.4 shows the grain size distribution.

Sample Name	Atterberg Limits	Specific Gravity	Void Ratio		Grain Size Distribution	Descriptive Classification	USC Description
			e_{max}	e_{min}			
Bulk aggregate for triaxial testing	Non-plastic	2.15	2.40	1.58	Gravel % Sand % Fines %	Sand with little fines. 90% grey, porous material, 10% black, vitreous material.	SW

Table 5.1: Index Properties for Triaxial Test Samples.

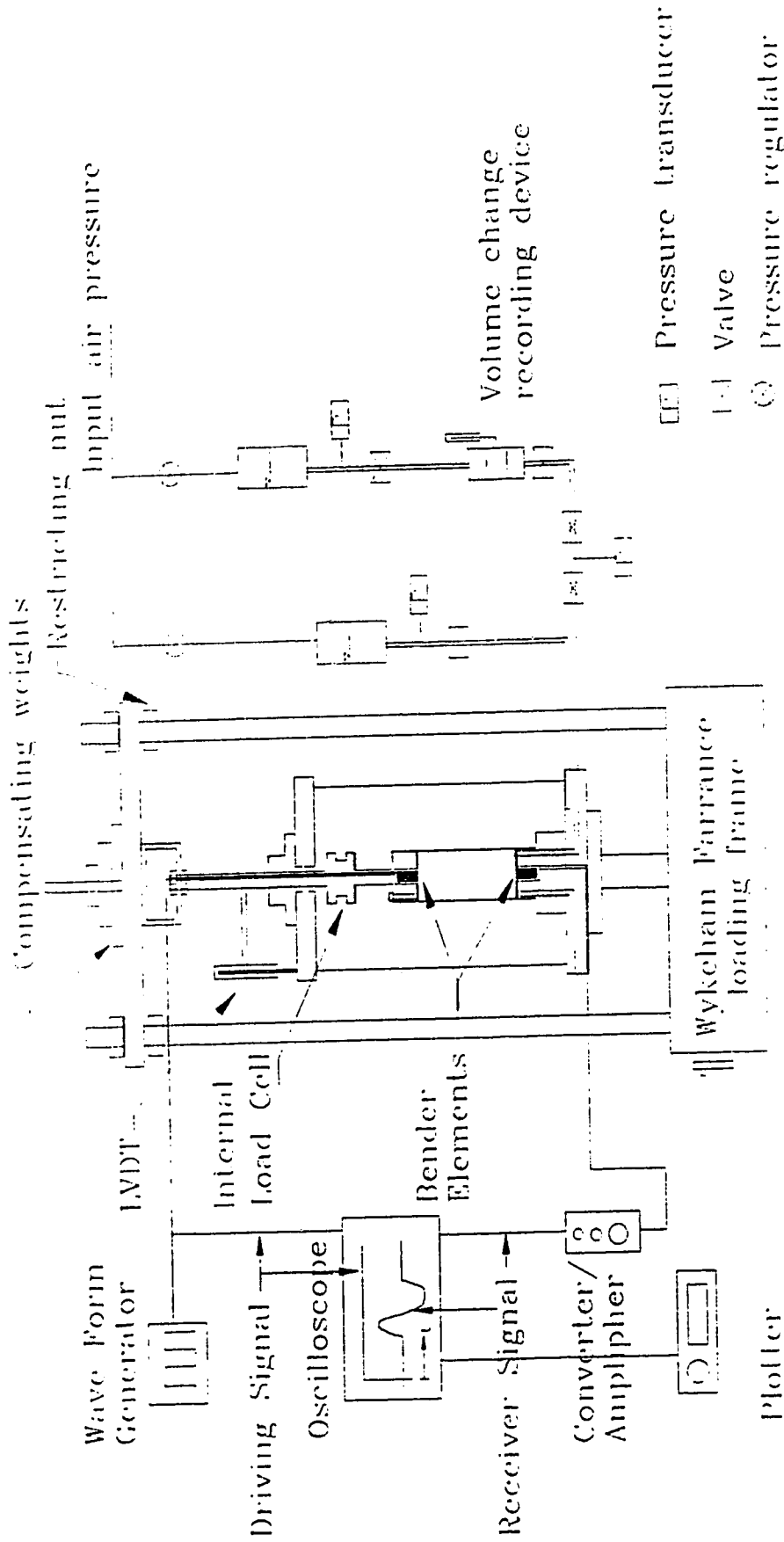
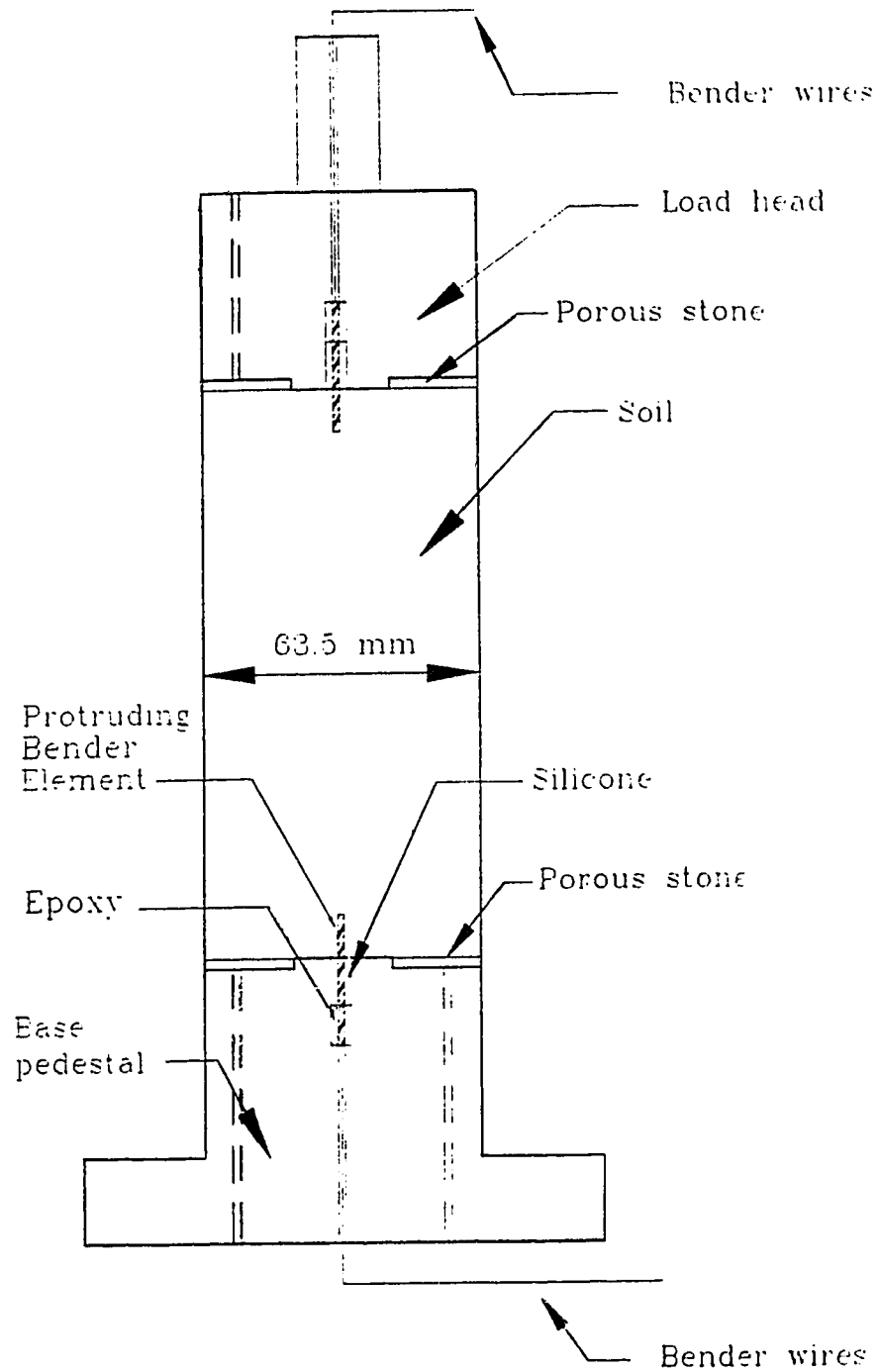


Figure 5.1: Schematic diagram of triaxial testing apparatus with shear wave velocity measurement, after Cunning (1994).



Each bender element
 32 mm L x 12.5 mm W x 0.5 mm t

Figure 5.2: Schematic diagram of protruding bender element system in triaxial head and base, after Sasitharan (1994).

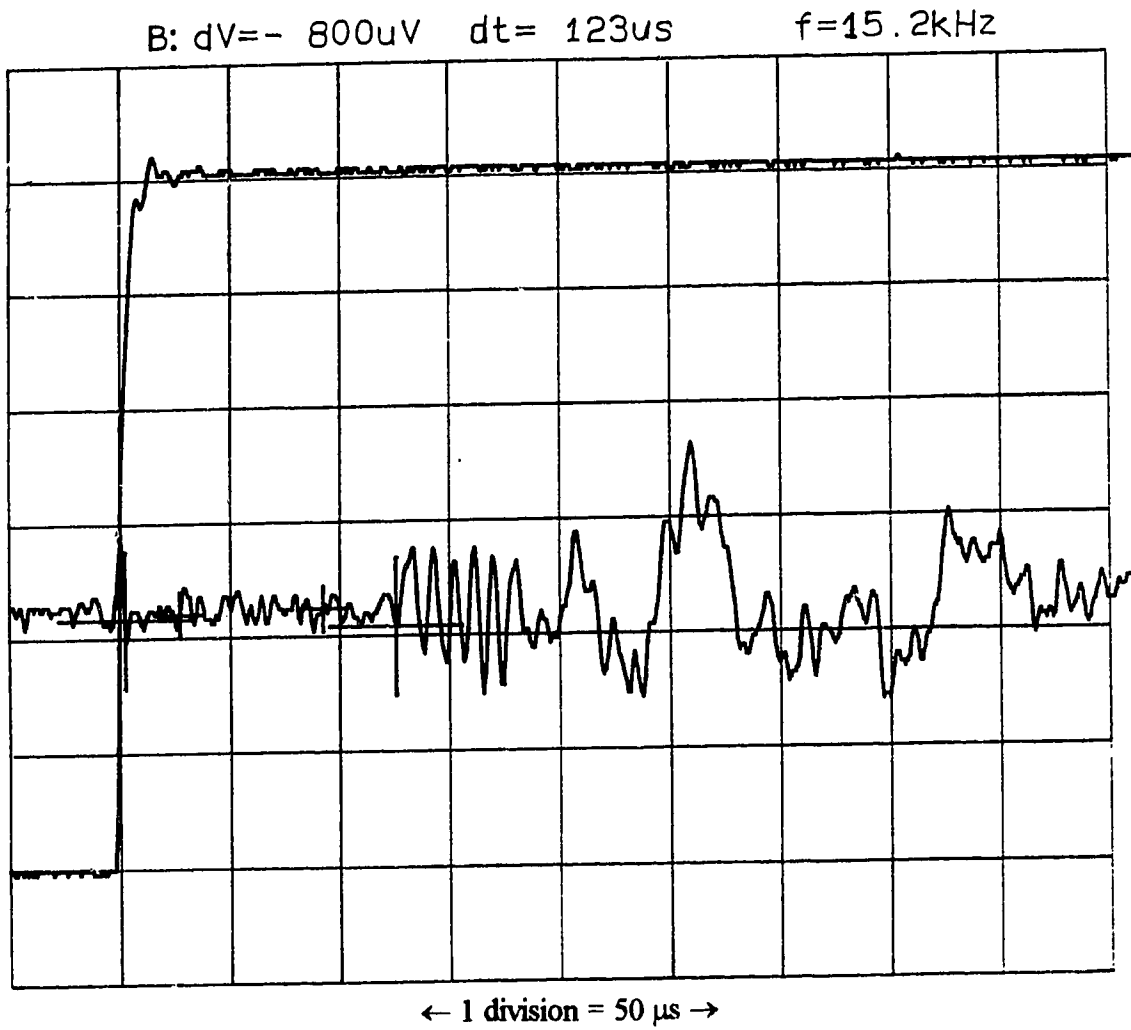


Figure 5.3: Typical plot of laboratory shear wave during consolidation in triaxial test apparatus.

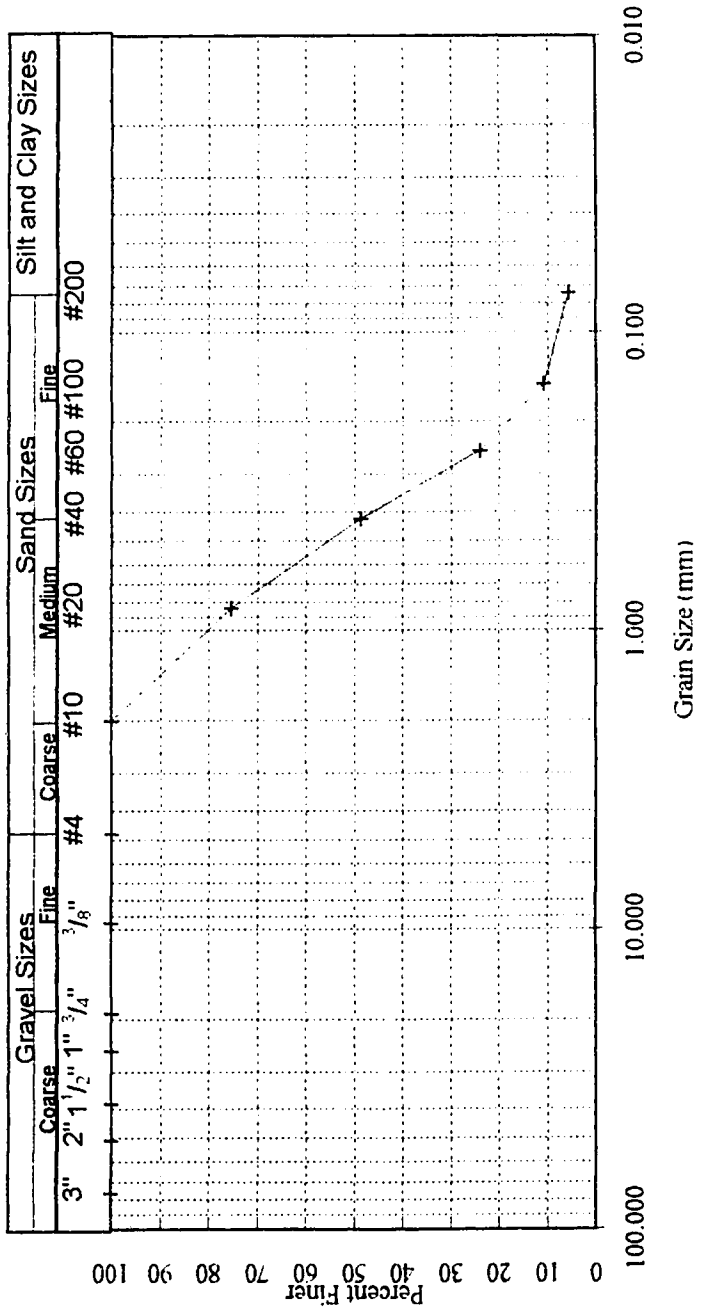


Figure 5.4: Grain size distribution of material prepared for triaxial test program.

6. Test Results

Each test conducted was given a test identification number, for example WS-250-T1-CU-LSS. This describes the test as Wabamun Sand (WS) tested at an isotropic consolidation state at the start of shear of 250 kPa in test number 1 (T1), a consolidated undrained test (CU) which showed the material to have limited strain softening characteristics (LSS). Other abbreviations include: CD = consolidated drained, SS = strain softening, and SH, strain hardening. The definition of tests as limited strain softening, strain softening or strain hardening follow the schematic behavior of a cohesionless soil in response to loading described by Robertson (1994).

6.1. Consolidation

Figure 6.1 summarizes the e versus p' relationships for the tests, including consolidation curves, quasi-steady states and ultimate steady states. This figure clearly demonstrates that the Wabamun sand undergoes crushing during consolidation, initiated at an effective stress of approximately 80 to 100 kPa. The effect of this crushing can be seen in the post-testing grain sizes shown in figure 6.2. This shows that crushing or increase in fines of the sample increases dramatically with the isotropic consolidation stress at the start of shearing. Note that tests WS-75-T4-CU-LSS and WS-75-T9-CD-SH, which started at the same isotropic consolidation stresses and close to the same void ratio, but were tested along different stress paths show little difference in grain crushing. That is, the change in grain size due to testing shown in figure 6.2 is the same for both tests. This despite the fact that test WS-75-T4-CU-LSS is an undrained test at a void ratio of 2.296, while WS-75-T9-CD-SH is a drained test, and undergoes a change in void ratio during testing of 0.633, ending at a void ratio of 1.675. Test WS-604-T8-CU-SS, which underwent a void ratio change of 0.600 during consolidation and was tested undrained at a void ratio of 1.661 showed an increase in fines due to crushing of 20%. This suggests that the grain crushing that takes place during the test is a function of consolidation only, and is not a factor in void ratio changes that take place during drained testing. However, to confirm this, and to understand what significance it may hold, it would be necessary to

conduct grain size analyses after consolidation and before testing for both the drained and undrained tests.

6.2. Shear Loading Results

A total of five triaxial compression tests were carried out on the Wabamun sand. All samples were prepared by the method of moist tamping as detailed in Appendix A, and consolidated to between 51 and 604 kPa before shearing at a constant rate of 0.15 mm/ min. Four samples were sheared undrained, and one sample was sheared drained. Due to the unavailability of shear wave velocity measuring equipment during this portion of the laboratory testing program, shear wave velocity measurements at USS were not taken.

Table 6.1 summarizes the test results for these tests, including the e , p' , σ_1' and σ_3' at USS for these tests. Figure 6.3 shows the results in terms of q against axial strain, figure 6.4 shows the variation in pore pressure with axial strain for the undrained tests, and figure 6.5 shows the variation in pore water volume with axial strain for the drained test. It can be seen that of the consolidated undrained tests, one showed a clear strain softening response, one showed a very limited strain softening response with little strain softening before strain hardening, and two showed limited strain softening behavior. These tests all reached initial peak deviator stresses at 0.5% to 2% axial strain. The corresponding pore pressures increased over the first 2% to 5% axial strain before leveling off. The consolidated drained test showed a strain hardening response, reaching a peak value of q at about 17% strain. The corresponding volume change showed a continued decrease, indicating water being expelled from the sample, up to the end of the test at 25% strain. For this reason, the sample should not be considered to have reached ultimate steady state.

Figure 6.6 shows the normalized stress paths for the tests in terms of q/p'_{USS} against p'/p'_{USS} . In this plot, consolidated undrained tests are normalized to p'_{USS} , while the consolidated drained test has each point normalized to p'_{USS} at the same void ratio. This normalization follows that suggested by Sladen and Oswell (1989) and eliminates the

effect of different void ratios from the different tests, such that the USSL appears as a point, and the collapse surface as a line. All tests should therefore end at the point $q_{\text{USS}}/p'_{\text{USS}} = M$ and $p'_{\text{USS}}/p'_{\text{USS}} = 1$. Figure 6.7 shows a plot of q_{USS} against p'_{USS} with a best fit straight line of $M = 1.56$ fitted to the data.

Based on the tests conducted, the USS parameters for Wabamun sand were determined to be:

$$\begin{aligned}\Gamma &= 3.2 \\ \lambda_{\text{In}} &= 0.5 \\ M &= 1.56 \\ \text{Valid over the stress range } p' &= 38 \text{ kPa to } 134 \text{ kPa}\end{aligned}$$

$$\begin{aligned}\Gamma &= 6.6 \\ \lambda_{\text{In}} &= 2.1 \\ M &= 1.56 \\ \text{Valid over the stress range } p' &= 134 \text{ kPa to } 227 \text{ kPa}\end{aligned}$$

This bilinear USSL attempts to account for the change in slope of the USSL due to the initiation of grain crushing at approximately 100 kPa effective stress. It was determined by best fit straight lines for steady states below and above the point of grain crushing. This bi-linear relationship is shown in figure 6.1.

6.3. Shear Wave Velocity Measurement

In general, shear wave velocity measurements should be normalized to in-situ horizontal and vertical stress according to the relationship:

$$V_{s1} = V_s \left(\frac{P_a}{\sigma'_{V'}} \right)^{na} \left(\frac{P_a}{\sigma'_{H'}} \right)^{nb} = V_s \left(\frac{P_a}{\sigma'_{V'}} \right)^{na+nb} \left(\frac{1}{K_0} \right)^{nb} \quad [11]$$

where:	V_{s1}	= Normalized shear wave velocity
	V_s	= Laboratory measured shear wave velocity
	P_a	= A reference stress, usually 100 kPa
	$\sigma'_{V'}$	= Vertical effective stress
	$\sigma'_{H'}$	= Horizontal effective stress
	na	= An exponent, usually 0.125
	nb	= An exponent, usually 0.125

$$K_0 = \sigma_{H'} / \sigma_{V'}$$

Robertson et al. (1992) recognised the difficulty in applying a normalization that requires K_0 be known, and recommended that normalized shear wave velocity be defined as:

$$V_{s1} = v_s \left(\frac{P_a}{\sigma_{V'}} \right)^{na+nb} \quad [12]$$

Chillarige et al. (1995) recognised that the error in excluding $\sigma_{H'}$ is typically less than 10%. Note that there is no difference between equation [11] and equation [12] if K_0 is equal to 1.0, as is the case in isotropically consolidated laboratory samples. However, in cases where K_0 is not equal to 1.0, as is generally the case when estimating in-situ state of natural deposits, it is important to account for K_0 . For this reason, the e-p'- V_s relationship will be developed using the general form of the equation for V_{s1} . The method used to account for K_0 when using the normalization defined by Robertson et al. (1995) is also shown.

Cunning (1994) details a method for determining an e-p'- V_s relationship based on shear wave velocity measurements taken during consolidation and at USS for a number of triaxial tests. In this method, shear wave velocity measurements are normalized to the stress state at which the measurement was taken according to equation [11]. Normalized shear wave velocities are then plotted as V_{s1} versus e, and a relationship between V_{s1} and e established as the equation of the best fit line. Cunning (1994) used a relationship of the form:

$$V_{s1} = A + Be \quad [13]$$

where: A and B = constants for a given sand or sands

We can substitute equation [13] and equation [4] into equation [11] and rearrange to get a relationship between void ratio, mean effective stress and shear wave velocity of the form:

$$V_s = (A - Be) \left(\frac{3p'}{(1 + 2K_0)P_a} \right)^{nu+nb} K_0^{nb} \quad [14]$$

If instead we were to substitute equation [13] and equation [4] into equation [12], following the normalization defined by Robertson et al. (1992), we would get a relationship of the form:

$$V_s = (A - Be) \left(\frac{3p'}{(1 + 2K_0)P_a} \right)^{na+nb} \quad [15]$$

This relationship differs from equation [14] by the factor K_0^{nb} . In order to account for this term, Robertson et al. (1995) define the relationship between V_{s1} and e as:

$$V_{s1} = (A + Be) K_0^{nb} \quad [16]$$

By substituting equation [4] and equation [16] into equation [12] and rearranging, we arrive again at equation [14]. Thus the normalization by Robertson et al. (1992), used with the corresponding definition of the V_{s1} - e relationship, is identical to the general normalization equation. This research will follow the accepted normalization by Robertson et al. (1992), and the corresponding definition of the V_{s1} - e relationship.

6.3.1. Laboratory Shear Wave Velocity Measurements

Test WS-298-110 was conducted following the completion of the general triaxial testing program to take advantage of the availability of working shear wave velocity measuring equipment and to obtain a limited set of shear wave velocity data. The results of these measurements are shown in table 6.1.

6.3.2. Determination of e - p' - V_s Relation By Extrapolation

The shear wave velocity measurements described in section 5.3.1 are clearly not sufficient to establish an e - p' - V_s relationship according to the method of Cunning (1994).

Skirrow (1995) as part of his research presented a summary of V_{s1} and e data for all of the sands that had been tested at the University of Alberta at that time. This relationship, shown in figure 6.8, is valid over a void ratio range of 0.4 to 1.3 and gives the relationship between V_{s1} and e as:

$$V_{s1} = (373 - 245e)K_0^{0.125} \quad [17]$$

While this relationship is acceptable over the void ratio range given, it suggests that shear wave velocities will go to zero at a void ratio of 1.522. This relationship cannot be valid at the void ratio range of 1.6 to 2.4 encountered in this research. Therefore the three data points for Wabamun sand, as well as recent data for Fraser sand (Chillarige, 1995) and Alaska sand (Cunning, 1994) were added to the V_{s1} versus e plot by Skirrow (1995), and a new relationship was determined. This plot can be found in figure 6.9. An exponential best fit gives a relationship between V_{s1} and e as:

$$V_{s1} = (139.54e^{-0.9019})K_0^{0.125} \quad [18]$$

This relationship is valid over the void ratio range of 0.4 to 2.4.

Substituting equation [4] and equation [18] into equation [12], we get the relationship between void ratio, mean effective stress and shear wave velocity valid for all the sands tested over a void ratio range of 0.4 to 2.4:

$$V_s = (139.54e^{-0.9019}) \left(\frac{3p'}{(1 + 2K_0)100} \right)^{0.25} K_0^{0.125} \quad [19]$$

Based on this relationship, contours of V_s can be plotted in e versus $\log p'$ space for a given value of K_0 . Figure 6.10 shows this data, along with the contours based on the relationship by Skirrow (1995), and the bilinear USSL for a K_0 value of 1.0 (isotropic consolidation). The contours of V_s based on equation [19] agree reasonably well with the contours based on Skirrow (1995) in the void ratio range of 0.5 to 1.0. The difference between the two sets of contours increases dramatically with the change in void ratio both above and below this range.

As mentioned previously, the linear best fit that Skirrow (1995) applied to his summary of V_{s1} against e (figure 6.8) is valid only over a limited range, and predicts that

shear wave velocities will go to zero at a void ratio of 1.522. The effect of this is seen clearly in the e versus $\log p'$ plot, with the contours of V_s proposed by Skirrow (1995) becoming asymptotic to a void ratio of 1.522. The non-linear best fit of the V_{s1} against e data proposed in this research would appear to be preferable, as it approximates reasonably the best fit straight line by Skirrow (1995) over the void ratio range of 0.4 to 1.0, and actually better fits the data in the void ratio range of 1.0 to 1.3, but does not place an artificial constraint on the shear wave velocity.

Test No.	p'c (kPa)	e	Vs (m/s)
WS-250-T1-CU-LSS	25.1	2.168	-
	50.0	2.157	-
	100.9	2.139	-
	150.4	2.113	-
	200.4	2.073	-
	250.4	2.026	-
WS-51-T3-CU-LSS	26.1	2.428	-
	50.8	2.407	-
WS-75-T4-CU-LSS	24.4	2.308	-
	50.3	2.303	-
	75.4	2.296	-
WS-604-T8-CU-SS	24.8	2.261	-
	51.3	2.253	-
	74.4	2.242	-
	101.1	2.210	-
	151.0	2.121	-
	200.2	2.030	-
	299.8	1.906	-
	399.3	1.796	-
	499.7	1.724	-
603.8	1.661	-	
WS-74-T9-CD-SH	24.9	2.308	-
	49.5	2.285	-
	74.2	2.212	-
WS-298-T10	23.7	2.373	-
	48.0	2.362	-
	98.6	2.339	66.6
	198.6	2.205	70.5
	297.8	2.085	77.4

Test No.	p'_{uss} (kPa)	e_{uss}	Vs_{uss} (m/s)	$\sigma'_{1\text{uss}}$ (kPa)	$\sigma'_{3\text{uss}}$ (kPa)
WS-250-T1-CU-LSS	154	2.026	-	321	71
WS-51-T3-CU-LSS	38	2.407	-	77	20
WS-75-T4-CU-LSS	67	2.296	-	118	41
WS-604-T8-CU-SS	227	1.661	-	421	101
WS-74-T9-CD-SH	176	1.675	-	377	77
WS-298-T10	N/A	N/A	N/A	N/A	N/A

Table 6.1: Summary of Triaxial Test Data.

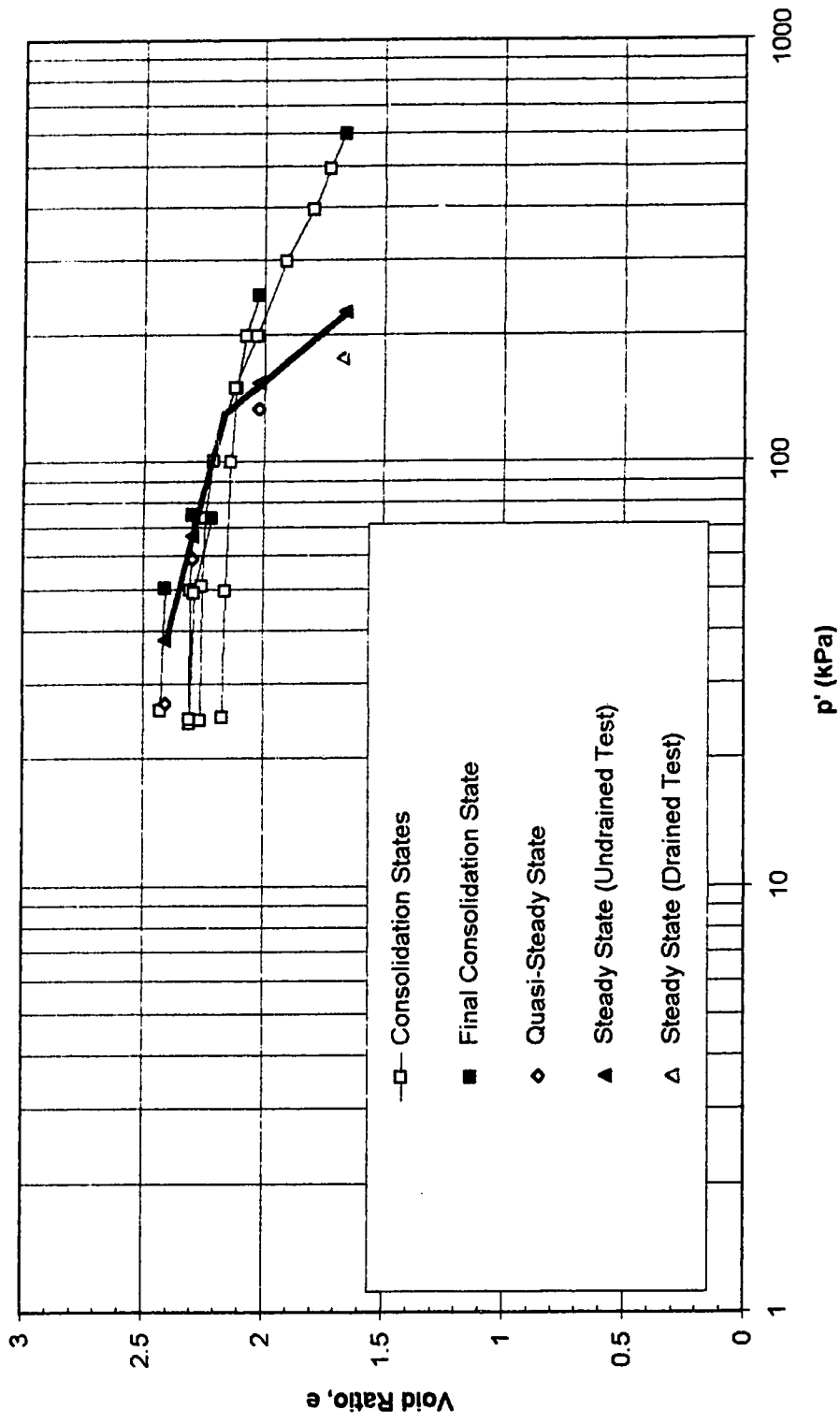


Figure 6.1: Summary of material states in e against $\log p'$ space during consolidation and triaxial testing, showing proposed bilinear USSL.

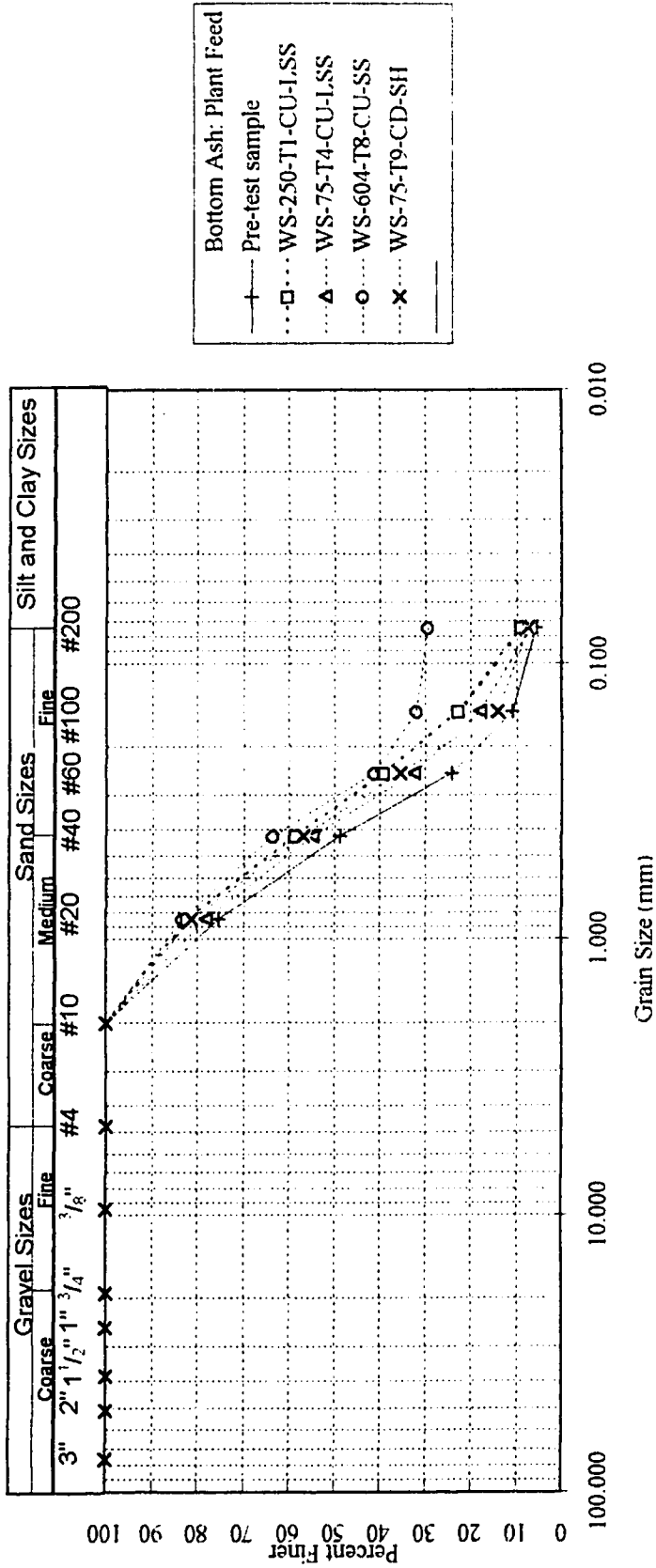


Figure 6.2: Grain size distribution of test samples following consolidation and triaxial testing.

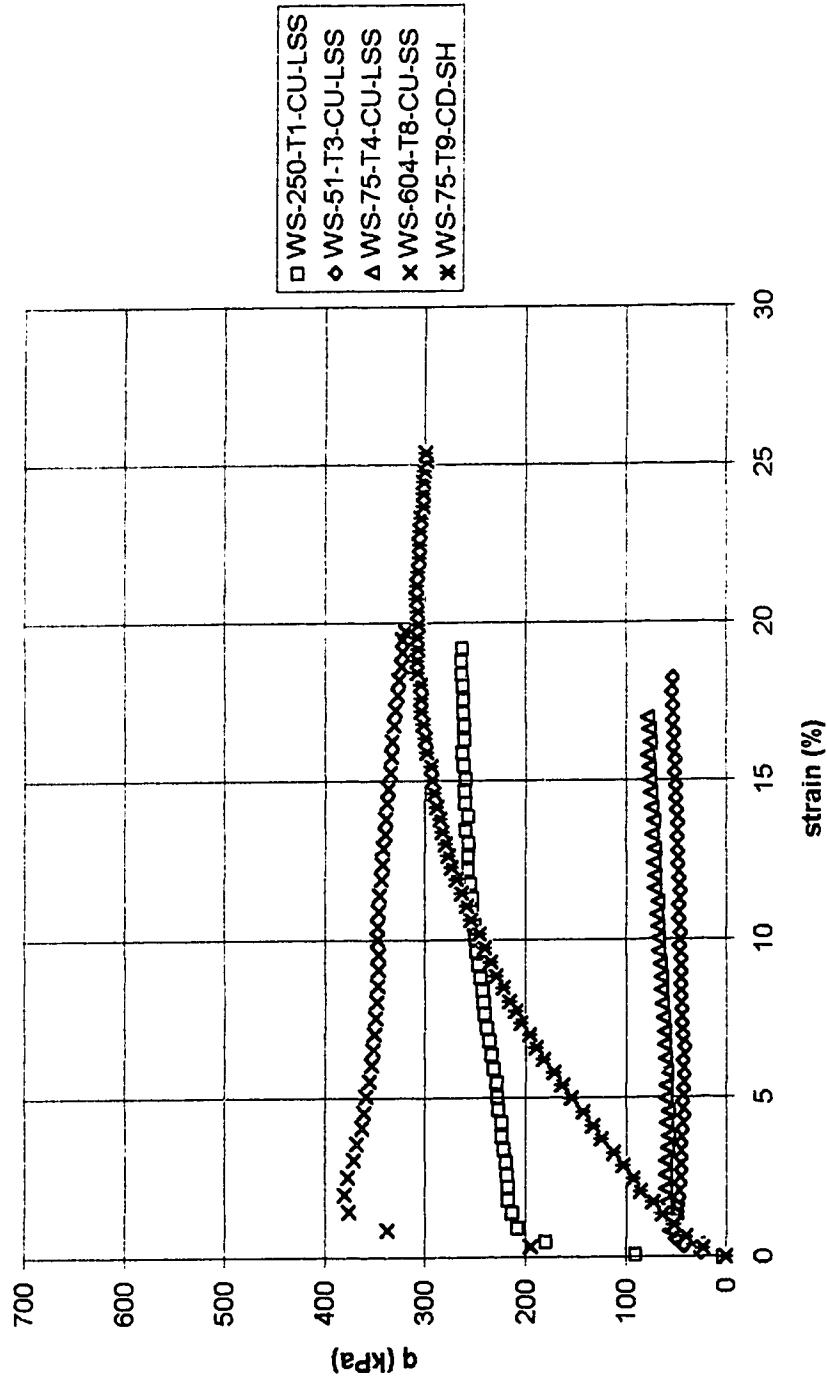


Figure 6.3: Summary of q against percent strain for all tests.

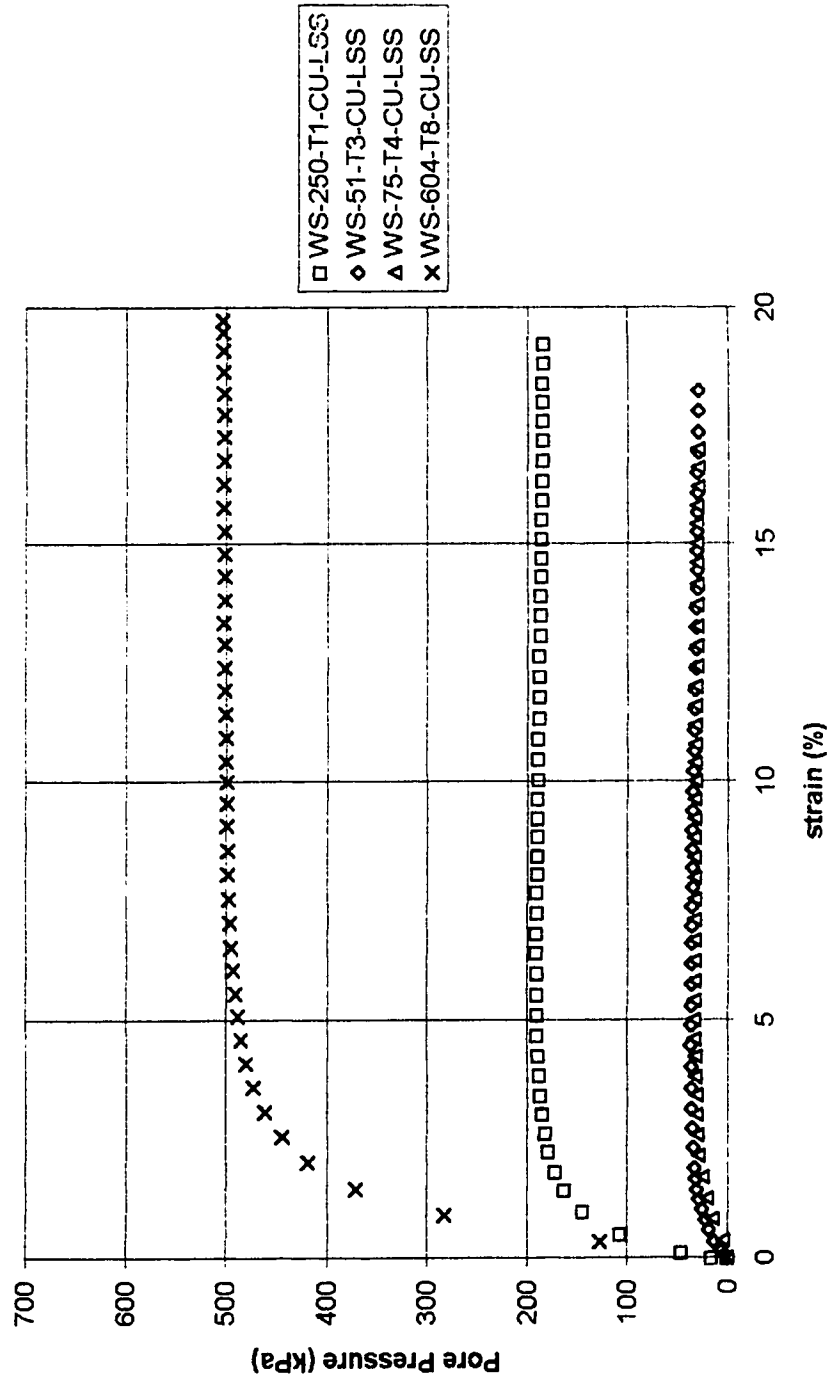


Figure 6.4: Summary of pore pressure against percent strain for undrained tests.

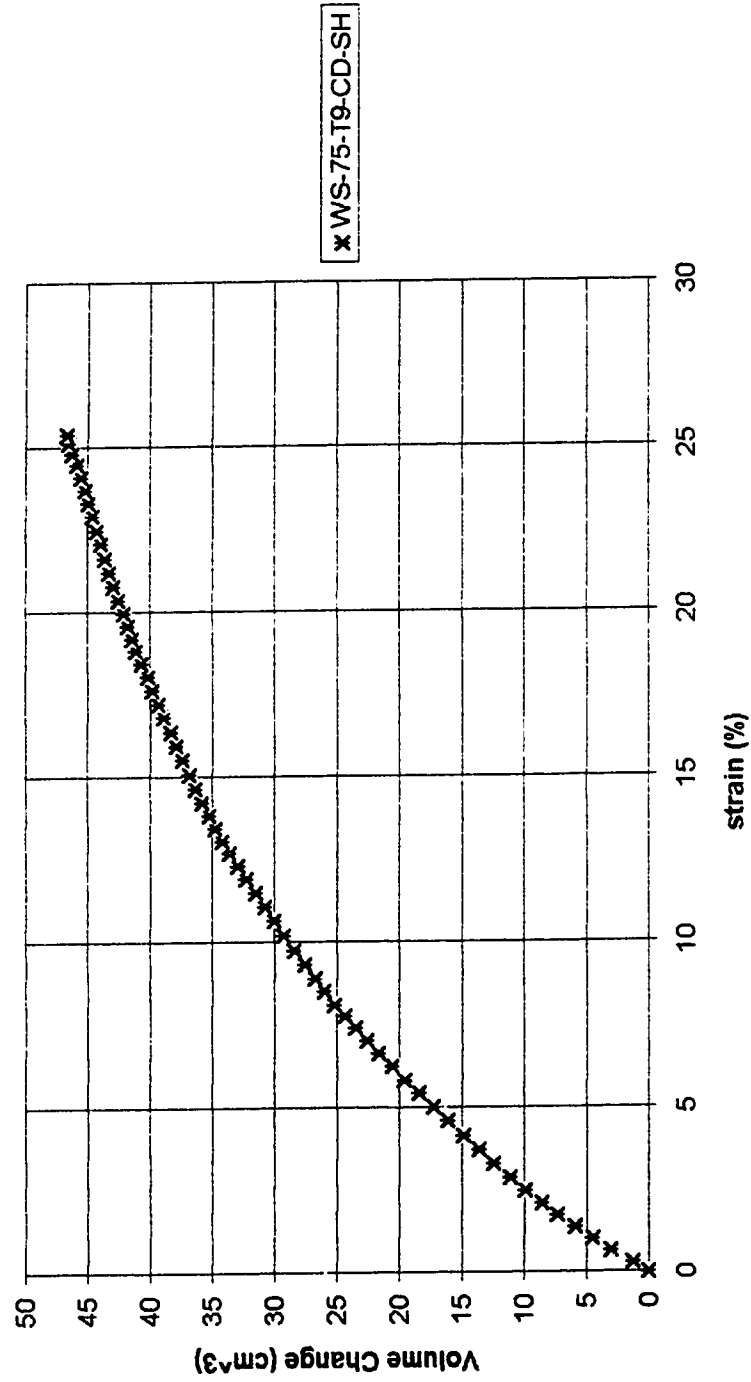


Figure 6.5: Summary of volume change against percent strain for drained test.

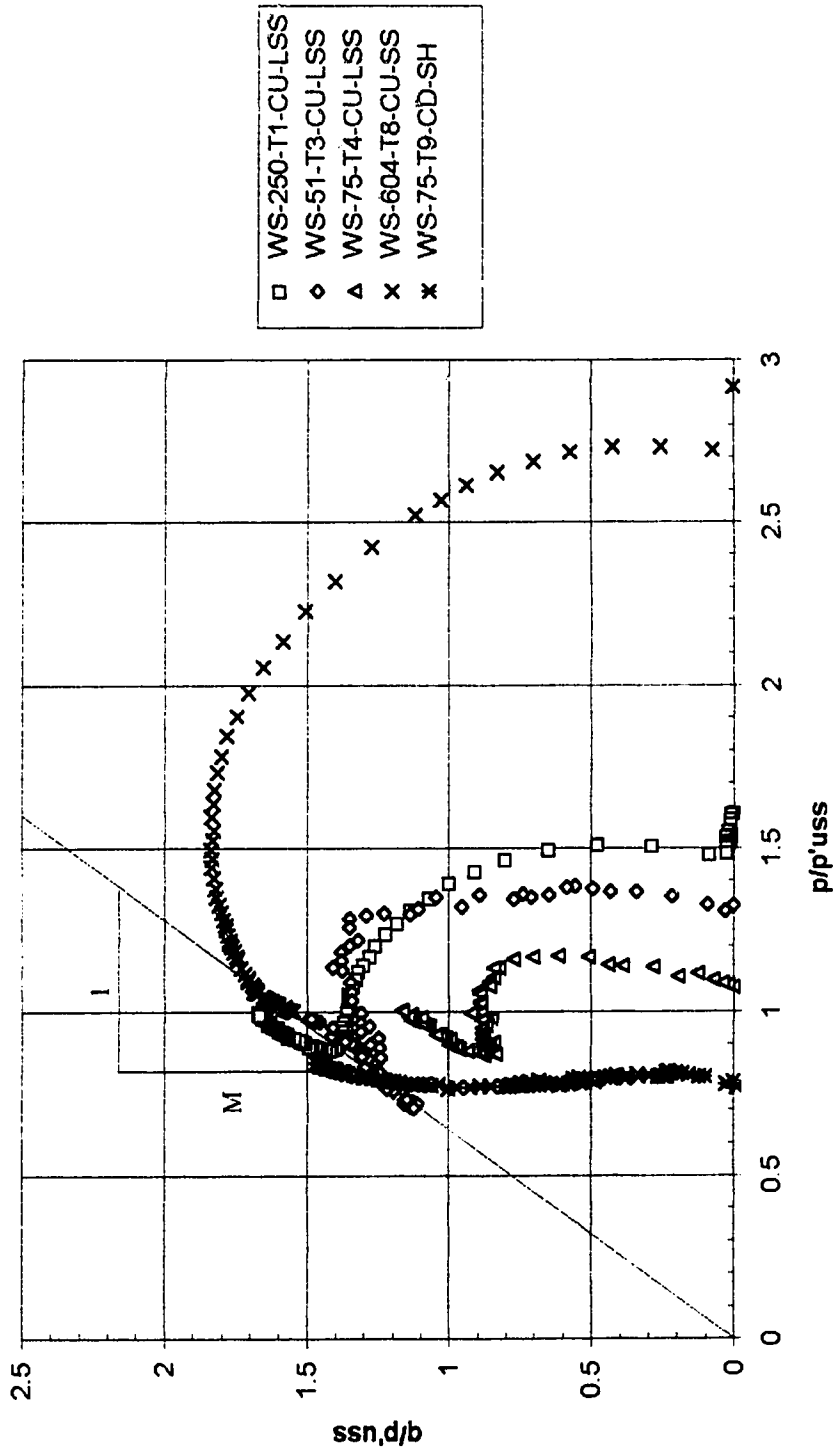


Figure 6.6: Summary of q/p'_{uss} against p/p'_{uss} (normalized stress space) for all tests.

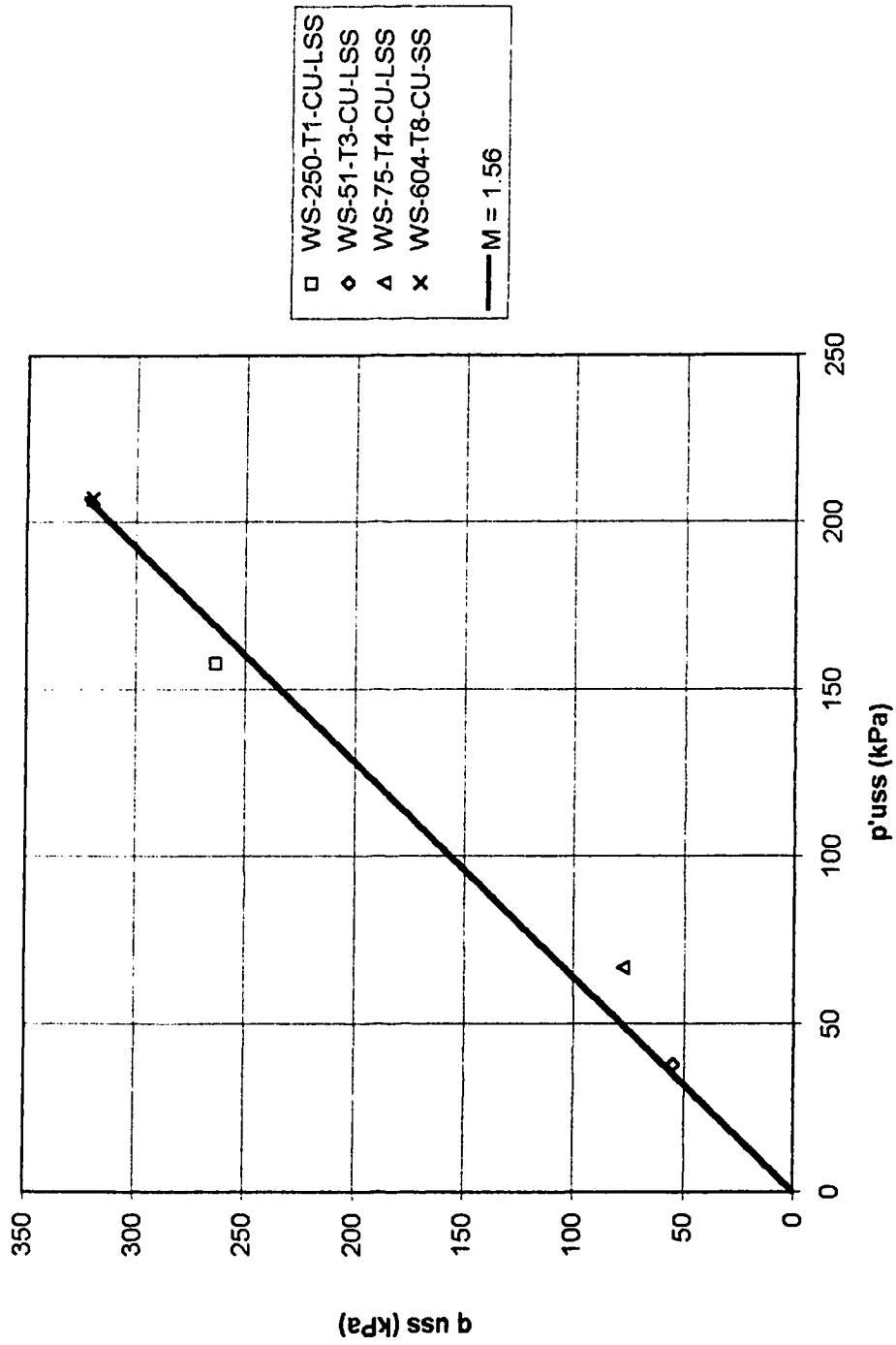


Figure 6.7: q_{uss} against p'_{uss} for all drained tests with best-fit line of slope M shown.

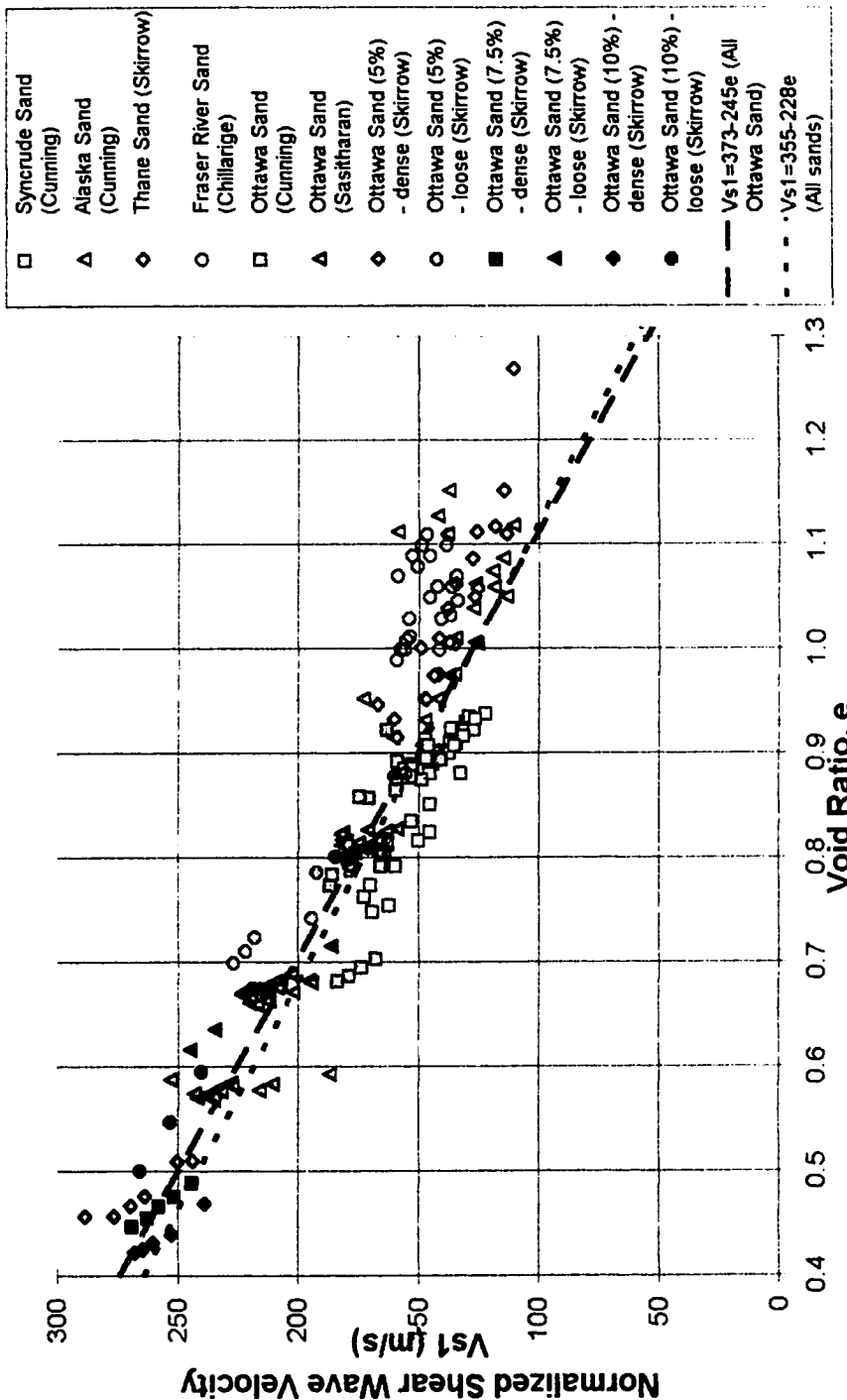


Figure 6.8: Summary of normalized shear wave velocity against void ratio after Skirrow(1995).

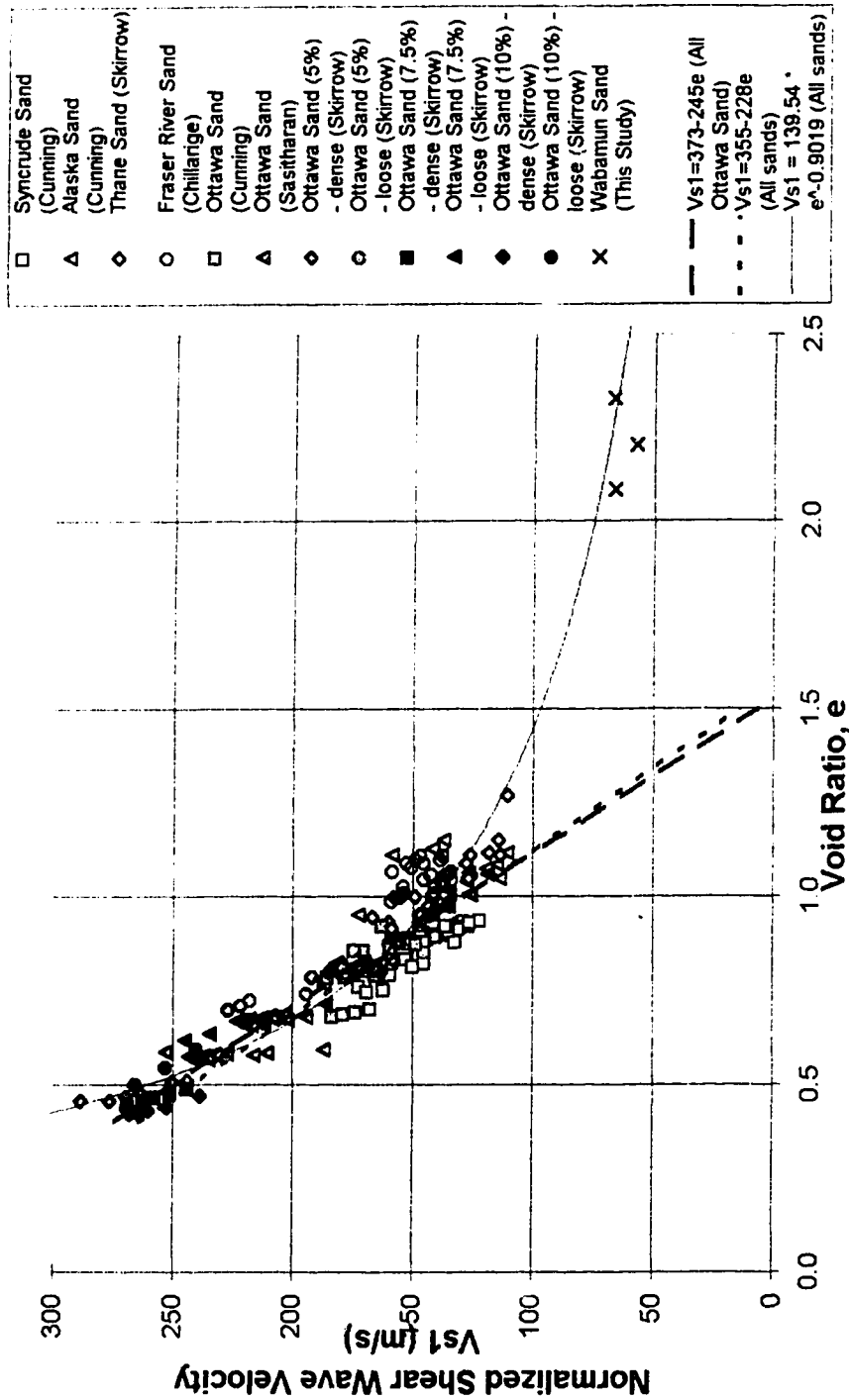


Figure 6.9: Summary of normalized shear wave velocity against void ratio with the addition of Wabamun sand, after Skirrow (1995).

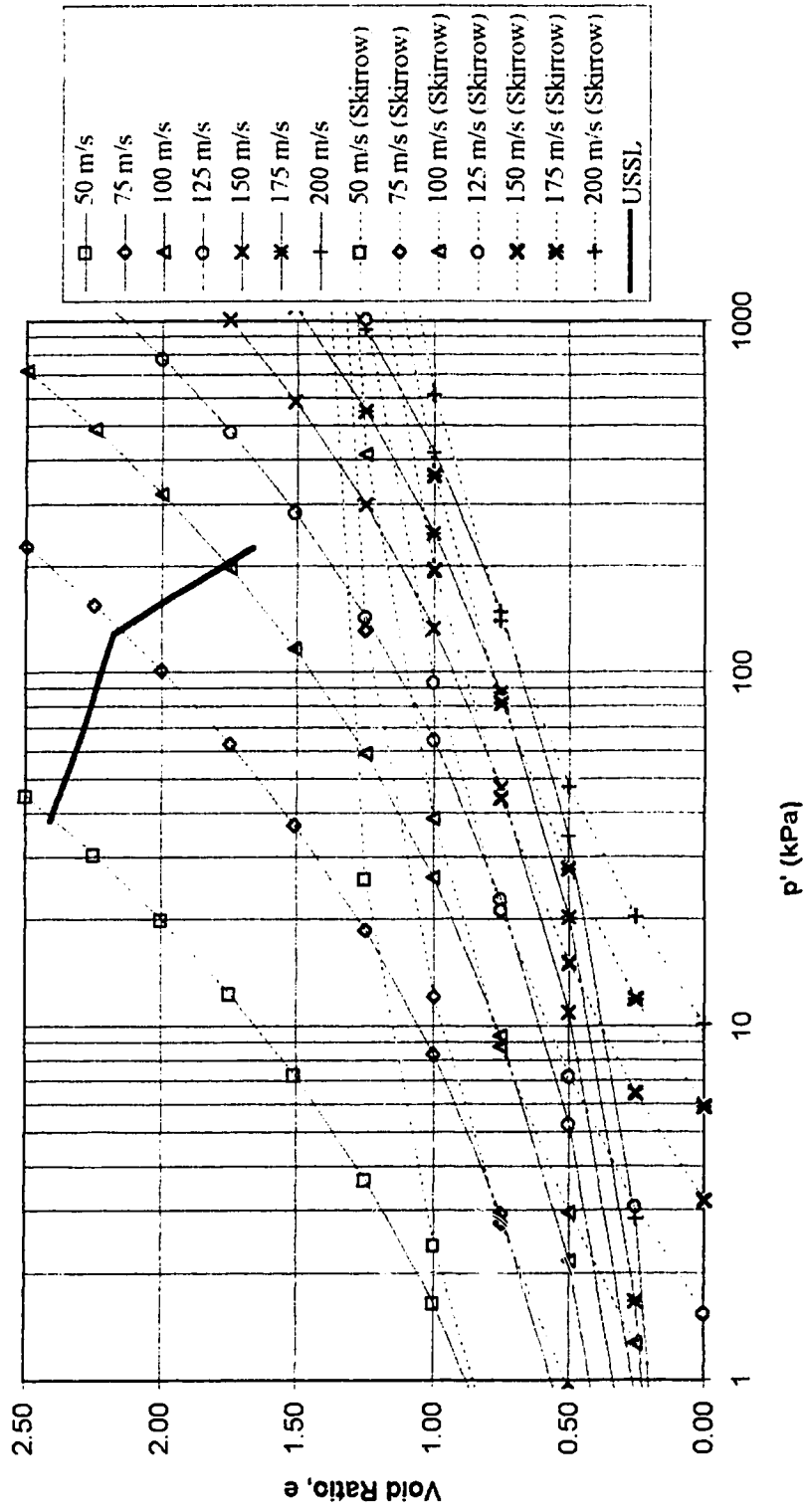


Figure 6.10: Contours of V_s in e against $\log p'$ space proposed by this research with the contours proposed by Skirrow (1995) and the bi-linear USSL for Wabamun sand shown for comparison.

7. Analysis of Test Data

7.1. Large Strain Consolidation Results

As part of the laboratory triaxial testing program, large strain isotropic consolidation testing on the Wabamun sand was undertaken. As discussed in Section 6.1, significant void ratio changes, likely due to grain crushing, occurred at effective stresses of greater than 80 to 100 kPa. Section 3.1.4 discusses the concept of a limiting state line (LSL) put forward by Semple (1988), or a limiting compression curve (LCC) suggested by Pestana and Whittle (1995). Both suggest that there is a unique limiting state, defined in e - p' space, beyond which a freshly deposited soil cannot exist. Semple (1988) suggests that this limiting state is a straight line in e - $\log p'$ space (figure 3.6). Pestana and Whittle (1995) proposed the use of a straight line in $\log e$ - $\log p'$ space (figure 3.7b) which becomes a curve asymptotic to a void ratio of zero at high stresses in e - $\log p'$ space (figure 3.7a).

Figure 7.1 summarizes the consolidation data for the Wabamun sand first as e - $\log p'$, and then as $\log e$ - $\log p'$. The LSL as described by Semple (1988) and the LCC defined by Pestana and Whittle (1995) are shown in each plot. From this figure it can be seen that within the range of void ratios and stresses considered in this test program, there is little difference between the LSL and the LCC. Further, an extrapolation of the LSL in e - $\log p'$ space and an extrapolation of the LCC in $\log e$ - $\log p'$ space both predict the effective stress at a void ratio of 1.0 to be approximately 5,000 kPa. For all practical purposes, this data is equally well represented by either the LSL or the LCC.

Semple (1988) and Pestana and Whittle (1995) both suggest that a state boundary line exists which is unique to all freshly deposited soils. In order to investigate this, consolidation data for a variety of sands was compiled. The data was selected to represent a range of initial void ratios from approximately 0.6 to 2.4, and a range of effective stresses for the initiation of crushing from approximately 80 kPa to 8000 kPa. All of the sands were consolidated isotropically from their initial stress conditions. Sands

were not all prepared by the same method, and samples of a given sand were not necessarily all prepared by the same method. Figure 7.2 shows this data in e -log p' space, and figure 7.3 shows the data in log e -log p' space. Again the LSL as described by Semple (1988) and the LCC defined by Pestana and Whittle (1995) are shown in each plot. Note in these plots that the LSL and the LCC represent a limiting state for all the sands, but that not all of the tests reach the suggested limiting state. In particular, the Halibut sand (Airey et al., 1988) has an initiation point for crushing a full log cycle below the LSL and LCC at the same void ratio.

In figure 7.2 it can be seen that the LSL predicts that all materials will go to a void ratio of zero at an effective stress of 100,000 kPa, while figure 7.3 shows the LCC reaching a void ratio of 0.3 at the same stress level. This supports the observation of Pestana and Whittle (1995) that the LSL is only an acceptable model for constitutive sand behavior over limited stress ranges. It appears that the LCC is a better model when considering large ranges of stress and void ratio. It would be beneficial, however, to test the Wabamun sand to extremely high stresses in order to observe which of the two curves the material would follow.

7.2. Classification Based on In-situ Testing

As discussed in section 3.1.5, Robertson et al. (1995) suggested a method for classifying soil behavior and evaluating age and cementation effects based on normalized cone resistance (Q_t) and normalized small strain shear modulus (G_o/q_t). The classification chart (figure 3.11) predicts that both Q_t and G_o/q_t will increase with age and cementation.

In-situ test site I2 was selected to conduct detailed analysis because it most closely represents material equivalent to that beneath the centerline of the dike, and because interpretation of SASW data includes shear wave velocity profiles both with and without a stiff crust. Data from the in-situ testing was normalized according to the method described in section 3.1.5, and plotted as Q_t against G_o/q_t . The bulk densities

used in calculating the small strain shear modulus from the field shear wave velocity were 1370 kg/m^3 above the water table and 1519 kg/m^3 below the water table.

Figure 7.4 shows the plot of Q_t against G_o/q_t for the case of no stiff crust, and figure 7.5 shows the same plot for the case of a stiff crust. In order to distinguish the data, it was separated into three depth regions based on the raw cone data (figure 4.14). The material from 0.0 to 0.725 m depth has a higher bearing resistance, and is considered a crust layer. For consistency, this definition will be used even with the shear wave velocity data that assumes the crust to be absent. The material from 0.750 to 0.950 m depth has very low cone bearing resistance, and is considered a weak layer. The remainder of the material, from 0.975 to 5.550 m depth is relatively consistent, and is grouped as the third layer. Note that within the third layer there is some variation in frictional resistance, especially at depths of 1.2 m and 5.4 m. These variations were not considered significant enough to define separate layers. In both of the plots, the material from 0.0 to 0.725 m depth plots in the region of cemented sands or cemented gravelly sands, the material from 0.750 to 0.950 m plots as slightly cemented sands, sand mixtures, silt mixtures and clays, and the remainder of the material plots as uncemented sand, sand mixtures and silt mixtures. The primary effect of the no crust assumption is to move the material from 0.0 to 0.725 m depth more toward the region of cemented gravelly sand. Note that much of the data plots as sand mixtures and silt mixtures, even though the in-situ samples indicate the material to be sand or gravelly sand (figure 4.3). This is due to the compressible nature of the Wabamun sand, and the reduction in cone bearing associated with compressible soils.

This classification by the plots of Q_t against G_o/q_t is similar to that given by plots of Q_t against normalized friction ratio (F_r) and Q_t against pore pressure ratio (B_q) (figure 4.22). The primary difference is that the plots of Q_t against G_o/q_t (figure 7.4 and figure 7.5) place the majority of the material in the range of young, uncemented deposits, while the plot of Q_t against F_r (figure 4.22) places the material well below the range of normally consolidated soil. This supports the discussion in section 4.5.2 that the sleeve friction measurements in the CPT are affected by cementation.

To further investigate the relationship between classification based on F_r and classification based on G_o/q_t , figure 4.22 has been replotted with the three layers identified. In this plot (figure 7.6), a log cycle was added to the classification plot by Robertson (1990) in order to display the F_r for most of the data points. Note that even with the addition of one log cycle, 6.3% of the points still plot off the scale.

Work by Murff (1987) and Zhu et al. (1995) suggest that low cone friction should be related to cemented soils. In the above data, we should expect to see points which plot in the low friction region in Q_t against F_r to plot in the cemented region in Q_t against G_o/q_t . While this appears to fit well with the data for the crust layer (0.0 to 0.725 m), and to a lesser degree the data for the weak layer (0.750 to 0.950 m), it does not hold true for the remainder of the data. However, the findings based on experience in carbonate sands that compressible, cemented materials will exhibit very low frictional resistance (Murff, 1987) appear to hold true for the Wabamun sand.

As a final note, it is worth considering the fact that the data is all based on field measurements with the exception of in-situ density and in-situ stresses assumed in the normalization process. The estimations used in this analysis are based on average values of laboratory measured void ratios and specific gravities, both of which showed significant variation between samples. Further, these parameters were measured on disturbed samples, so that any influence that fabric or cementation may have on in-situ material has been eliminated. Errors in the estimation of these parameters will have varying effects on Q_t , F_r and G_o/q_t . Note especially that the calculation of G_o relies on in-situ density first in the forward modeling of SASW data to calculate V_s and second in the calculation of G_o from V_s and ρ . In general, an increase in density will cause a corresponding decrease in Q_t and F_r , and a proportional increase in G_o/q_t . An accurate parametric analysis could not be undertaken, however, as it would have required re-analysis of the SASW data.

7.3. Prediction of Liquefaction Potential From Laboratory and Field Testing

Cunning (1994) suggested a procedure for evaluating the potential for flow liquefaction based on the laboratory determined e - p' - V_s relationship and USS parameters and field measured values of V_s against depth. The depth can be converted into σ_v' using the bulk density of the soil and the depth of the water table. These data points of coordinates V_s and σ_v' can be plotted in e - p - V_s space (figure 6.10). Figure 6.10 shows the location of the USSL for the Wabamun sand in terms of e against p' .

The location of the in-situ V_s points relative to the USSL gives an estimation of the large strain behavior. Data points which plot above the USSL have the potential for flow liquefaction if the material is strain softening. The potential for strain softening must be determined in the laboratory using samples of the material consolidated to similar values of p' and V_s . Data points which fall below the USSL should exhibit a dilative response, and the potential for flow liquefaction does not exist.

Equation [19] can be rearranged to give void ratio as a function of V_s , p' and K_0 :

$$e = \left(\frac{V_s}{139.54 K_0^{0.125}} \left(\frac{(1 + 2K_0)100}{3p'} \right)^{0.25} \right)^{\frac{-1}{0.9019}} \quad [20]$$

This equation can be used to estimate the void ratio in-situ based on field shear wave velocity measurements and in-situ stress state. For the Wabamun field data, V_s was given by the SASW testing. Vertical effective stress was calculated from σ_v' and K_0 using equation [4]. The vertical effective stress used was that estimated from laboratory measured index properties and used in the normalization of SASW and CPT data. As K_0 was not measured in-situ, plots were made using $K_0=0.4$ and $K_0=1.0$ to represent a range of reasonable values for naturally sedimented deposits. Zhu et al. (1995) point out that increasing cementation in a sand will tend to decrease the at-rest lateral stress. If the Wabamun sand is cemented in-situ, we can expect that the material will exhibit a lower K_0 value, and that the plots for $K_0 = 0.4$ may be more representative of in-situ state.

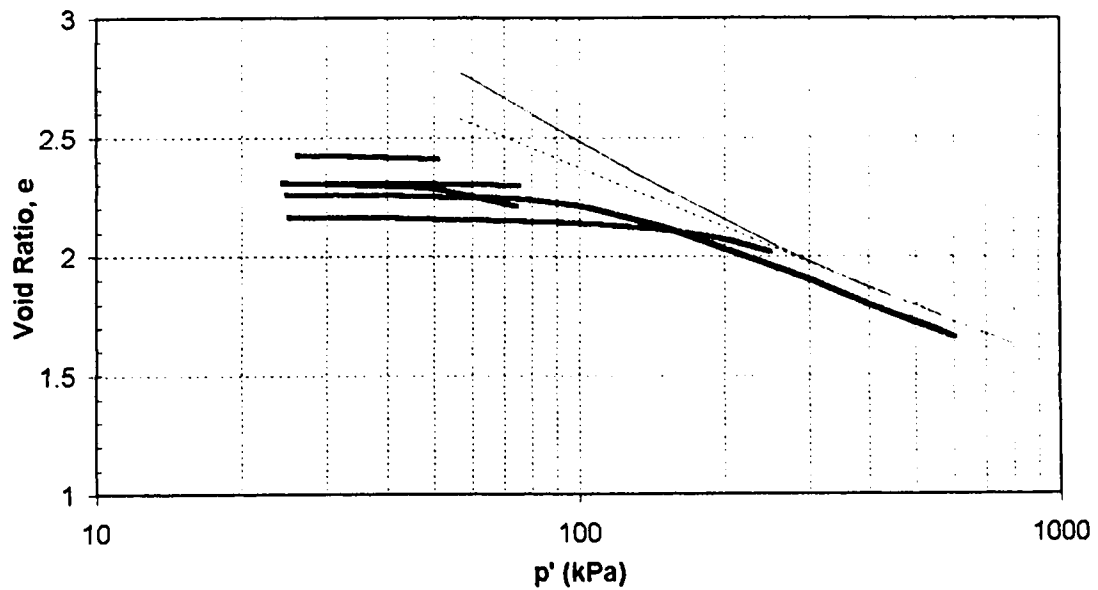
Equation [20] was used to plot field data for SASW testing at in-situ test location 12. Figures 7.7 and 7.8 show the relationship for $K_0=0.4$ and $K_0=1.0$ for the SASW data which assumes no crust, while figures 7.9 and 7.10 show the two cases for the SASW data which assumes a crust. In each plot, three data sets are shown. The first data set shows the in-situ shear wave velocity data as it was determined from SASW. The second data set has an aging correction made to the shear wave velocity according to Figure 3.10 (Robertson et al., 1995). Figure 3.10 suggests that for a deposit of approximately 5 years of age (as determined from the September 1989 airphoto, figure 3.12), the field measured shear wave velocities should be increased by 12 m/s to match laboratory measured shear wave velocities. Note here that the correction uses the minimum age for the deposit. Age of the deposit is expected to increase with depth, up to a maximum age at the base of the lagoon of approximately 17 years.

The second data set is assumed to represent the condition beneath the centerline of the dike prior to the construction of the dike. The third data set therefore estimates the condition of the soil following the construction of the dike and impoundment of the reservoir. Note that for simplicity pore pressure changes resulting from the development of seepage beneath the dike and the effects of consolidation due to this increase in load have not been considered.

Comparison of the plots for a K_0 value of 0.4 to those for K_0 of 1.0 demonstrate the significance of this parameter in estimating in-situ state. While there is little change in the contours of V_s in $e-p'$ space as a result of changes in K_0 , void ratio changes by as much as 0.25 for this material.

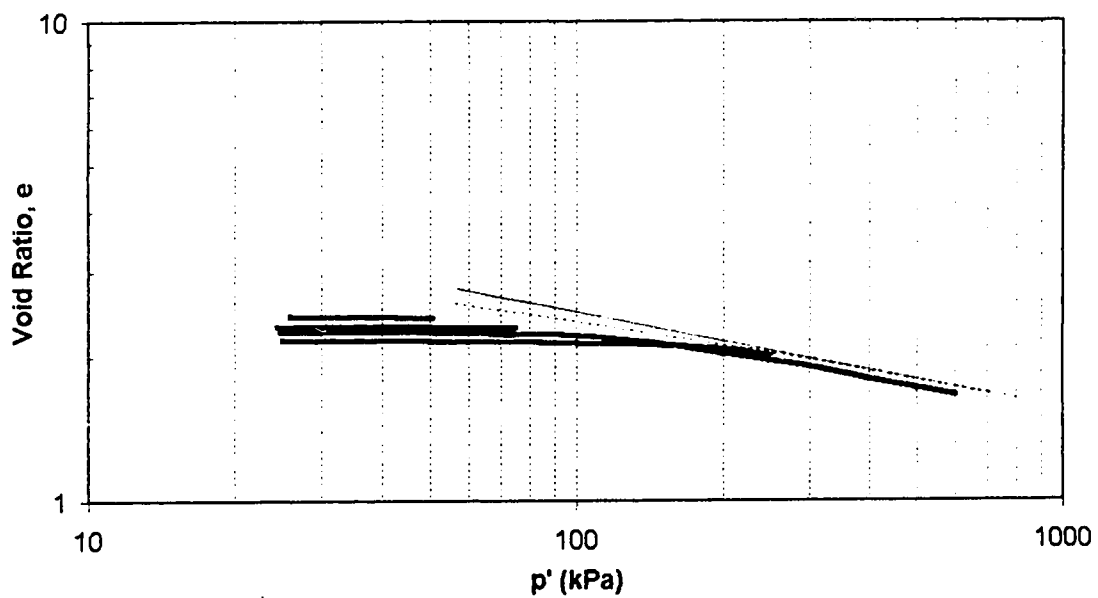
These plots show that this analysis does not predict that the Wabamun sand to be strain softening, despite the fact that it is believed to have failed as a flow liquefaction event. The material which most closely approaches contractive behavior is at a depth of approximately 1.5 m in the analysis which assumes a K_0 of 1.0 and the presence of a stiff crust. The weak layer from 0.750 to 0.950 m depth identified in the CPT at this location (figure 4.14) also plots close to the USSL. However, these points are still some 15 m/s in shear wave velocity below the USSL.

Two explanations for this failure to predict contractive behavior are offered. First, this analysis relies on the prediction of in-situ stresses. As discussed previously the estimation of in-situ stresses, while the best possible under the circumstances, is subject to error. Second, the analysis relies on Robertson et al. (1995) relationship between shear wave velocity and age (figure 3.10). This relationship is based on three silica sands which are neither compressible or cementing. Given the effect of compressibility and cementation on small strain shear modulus (figure 3.11), the shear wave velocity correction with age for Wabamun sand could be higher than that predicted by Robertson et al. (1995).



a)

- Wabamun Sand
- LSL - method by Semple (1988)
- LCC - method by Pestana and Whittle (1995)



b)

- Wabamun Sand
- LSL - method by Semple (1988)
- LCC - method by Pestana and Whittle (1995)

Figure 7.1: Consolidation data for Wabamun sand showing the LSL (Semple, 1988) and the LCC (Pestana and Whittle, 1995) in a) e -log p' and b) log e -log p' .

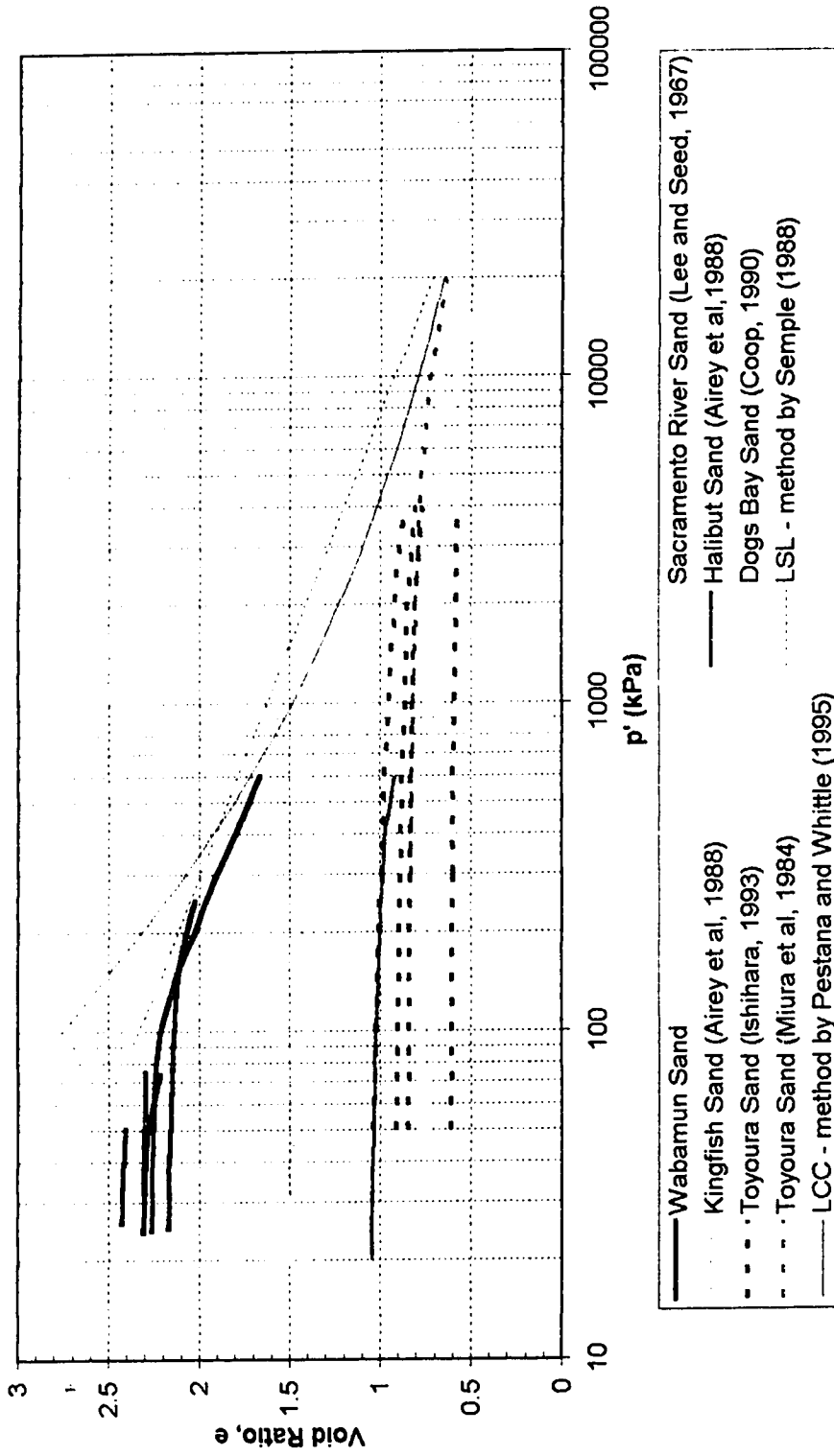


Figure 7.2: Summary of consolidation data for sands showing the LSL (Semple, 1988) and the LCC (Pestana and Whittle, 1995) in e - $\log p'$.

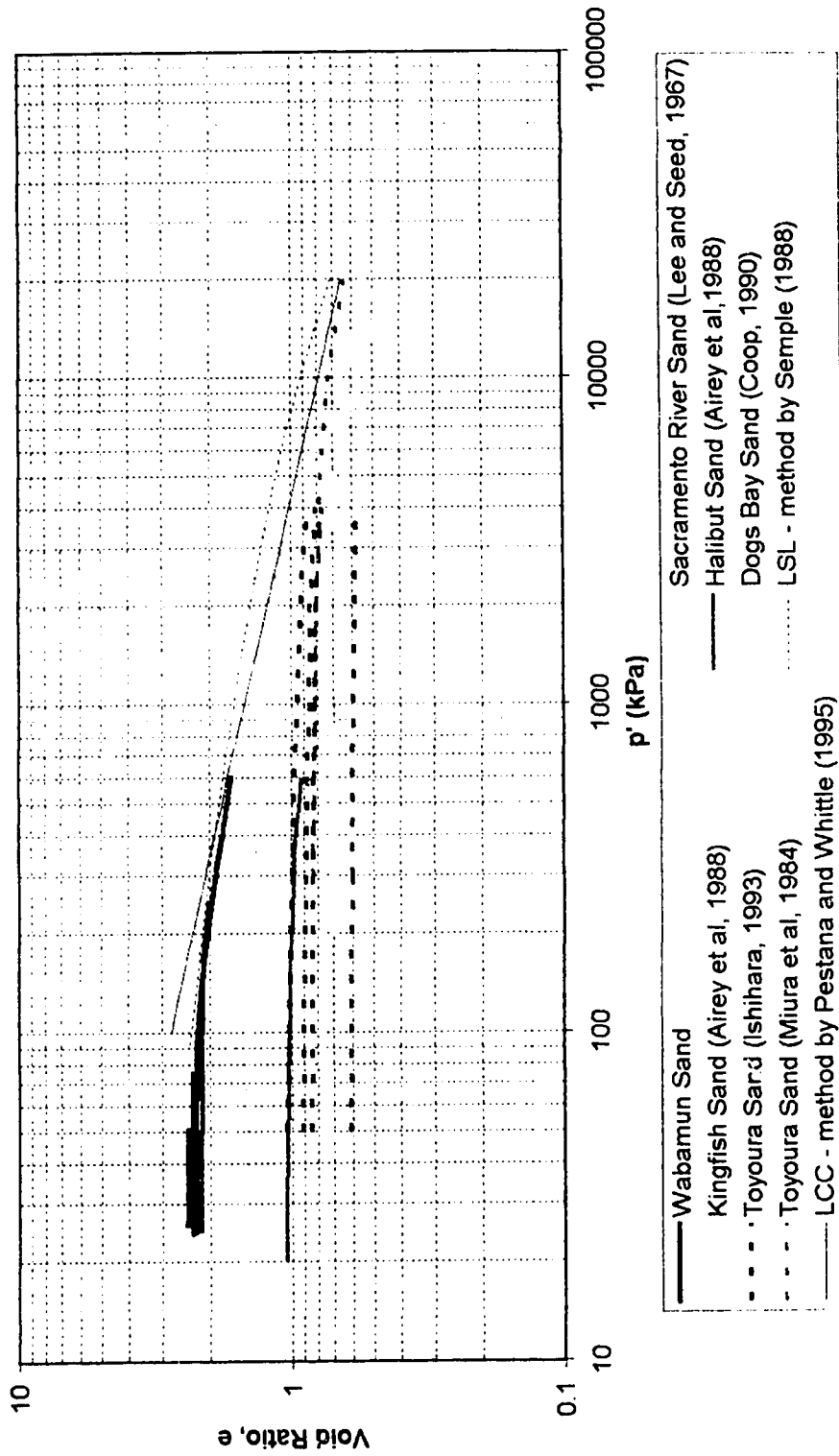
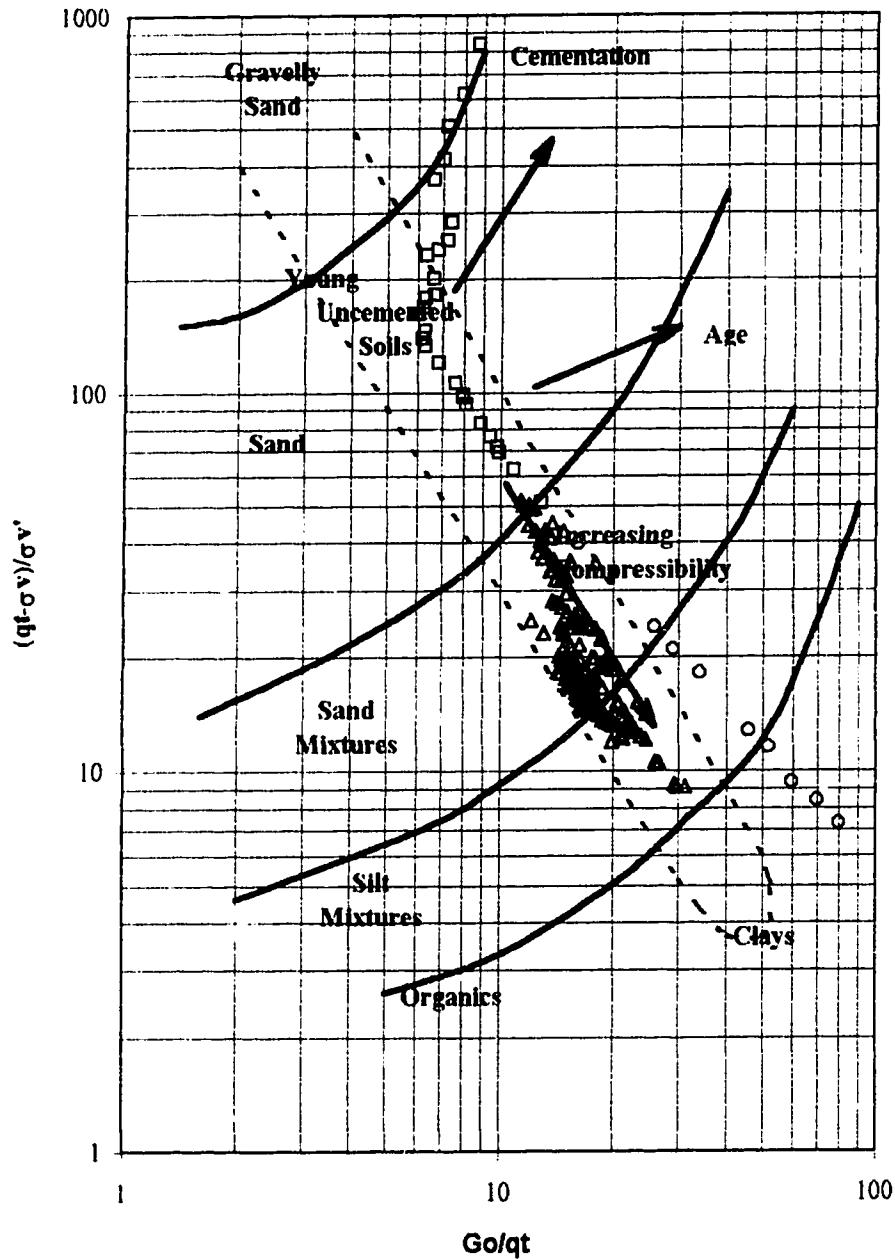


Figure 7.3: Summary of consolidation data for sands showing the LSL (Semple, 1988) and the LCC (Pestana and Whittle, 1995) in $\log e$ - $\log p'$.



□ 0.000 to 0.725 m ○ 0.750 to 0.950 m △ 0.975 to 5.550 m

Figure 7.4: Classification based on normalized cone resistance and normalized small strain shear modulus for in-situ test site I2 with the assumption of no crust in the analysis of SASW data.

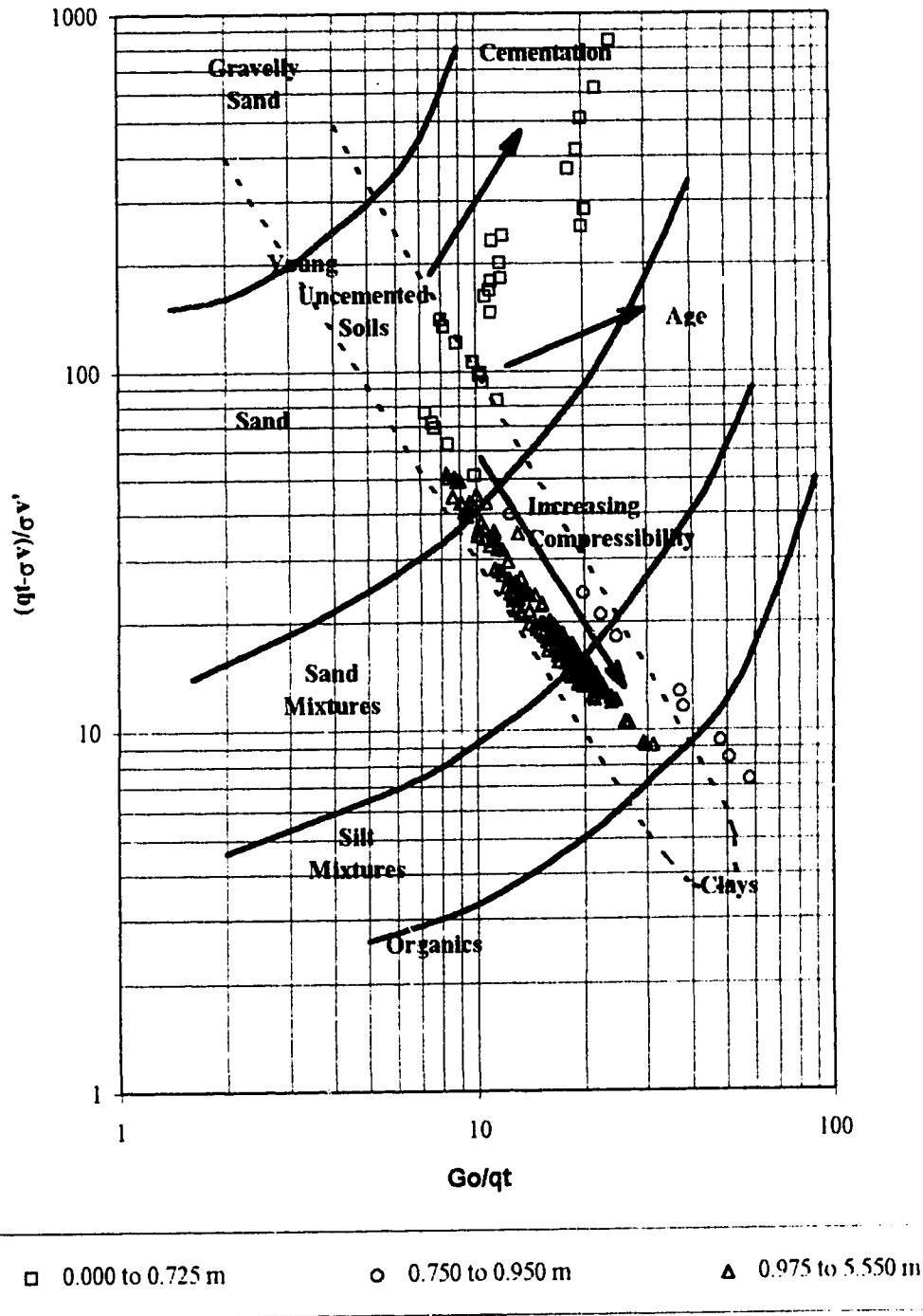
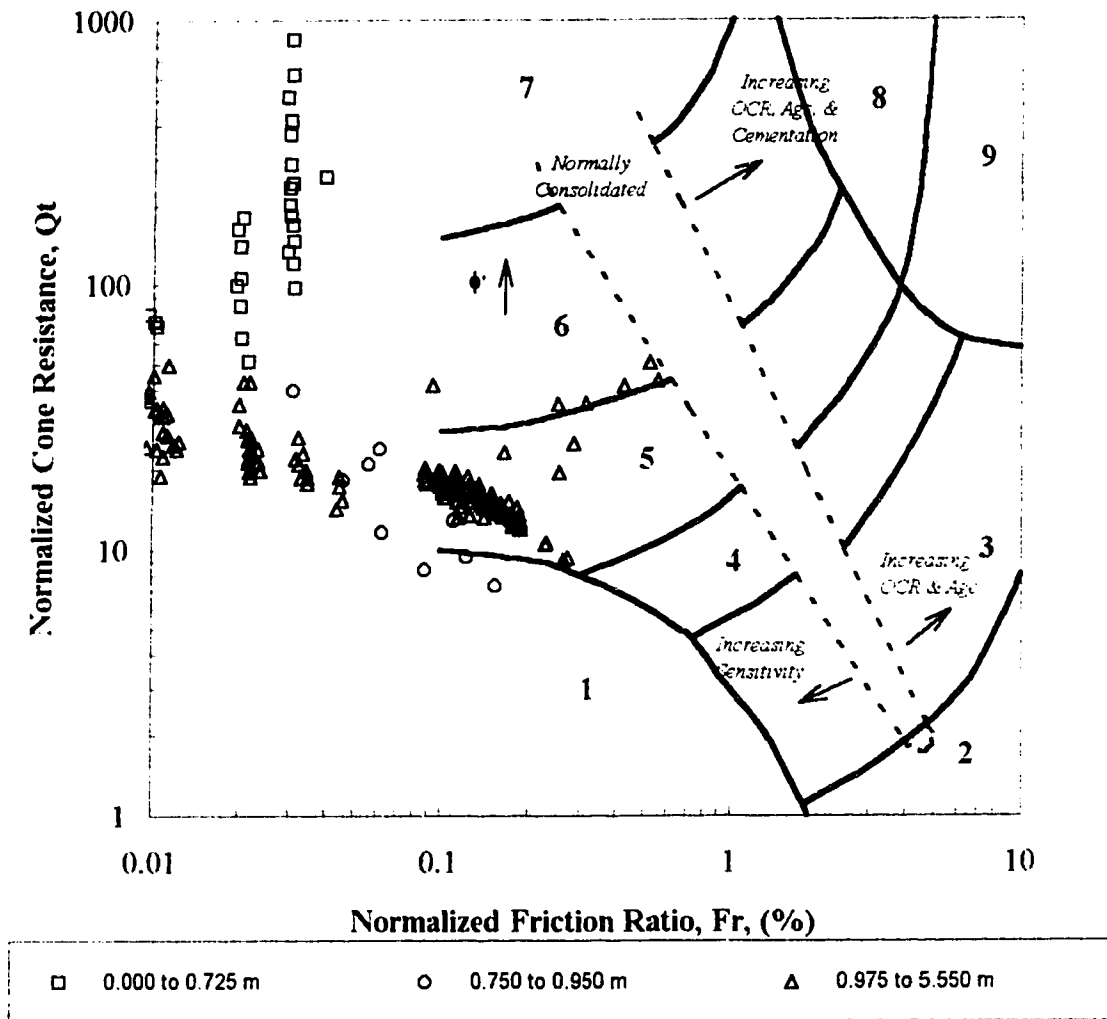


Figure 7.5: Classification based on normalized cone resistance and normalized small strain shear modulus for in-situ test site I2 with the assumption of a stiff crust in the analysis of SASW data.



Legend

- | | | |
|-------------------------------|--|---------------------------------|
| 1. Sensitive, fine grained | 4. Silt mixtures - clayey silt to silty clay | 7. Gravelly sand to sand |
| 2. Organic soils - peats | 5. Sand mixtures - silty sand to sandy silt | 8. Very stiff sand clayey sand* |
| 3. Clays - clay to silty clay | 6. Sands - clean sand to silty sand | 9. Very stiff, fine grained* |
| | * Heavily O/C or cemented | |

Figure 7.6: Classification based on normalized cone resistance and normalized friction ratio for in-situ test site I2 with the scale altered to include 93.7 % of the data points.

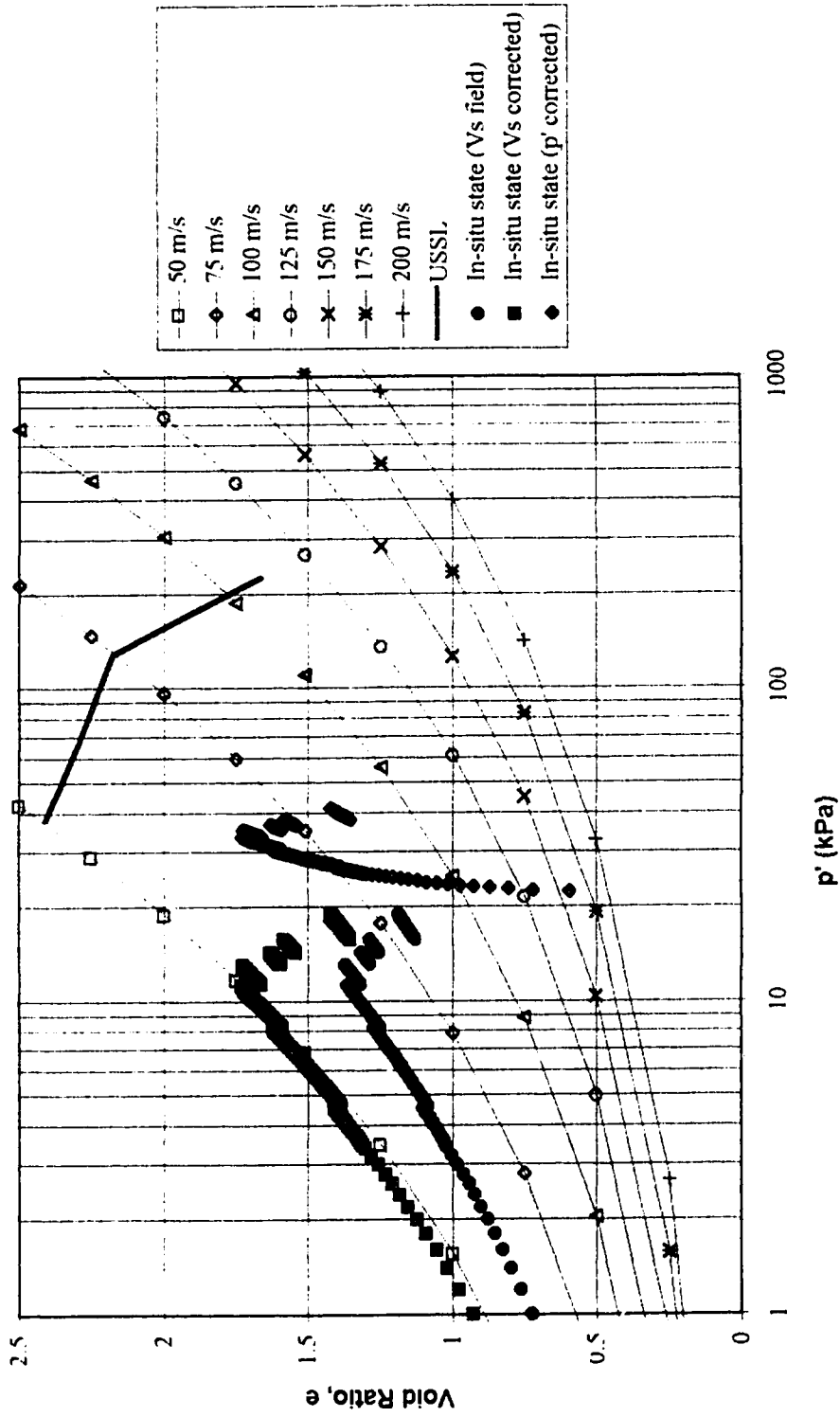


Figure 7.7: Prediction of in-situ state based on estimated in-situ stresses for $K_0 = 0.4$ and field measured shear wave velocities for the assumption of no crust.

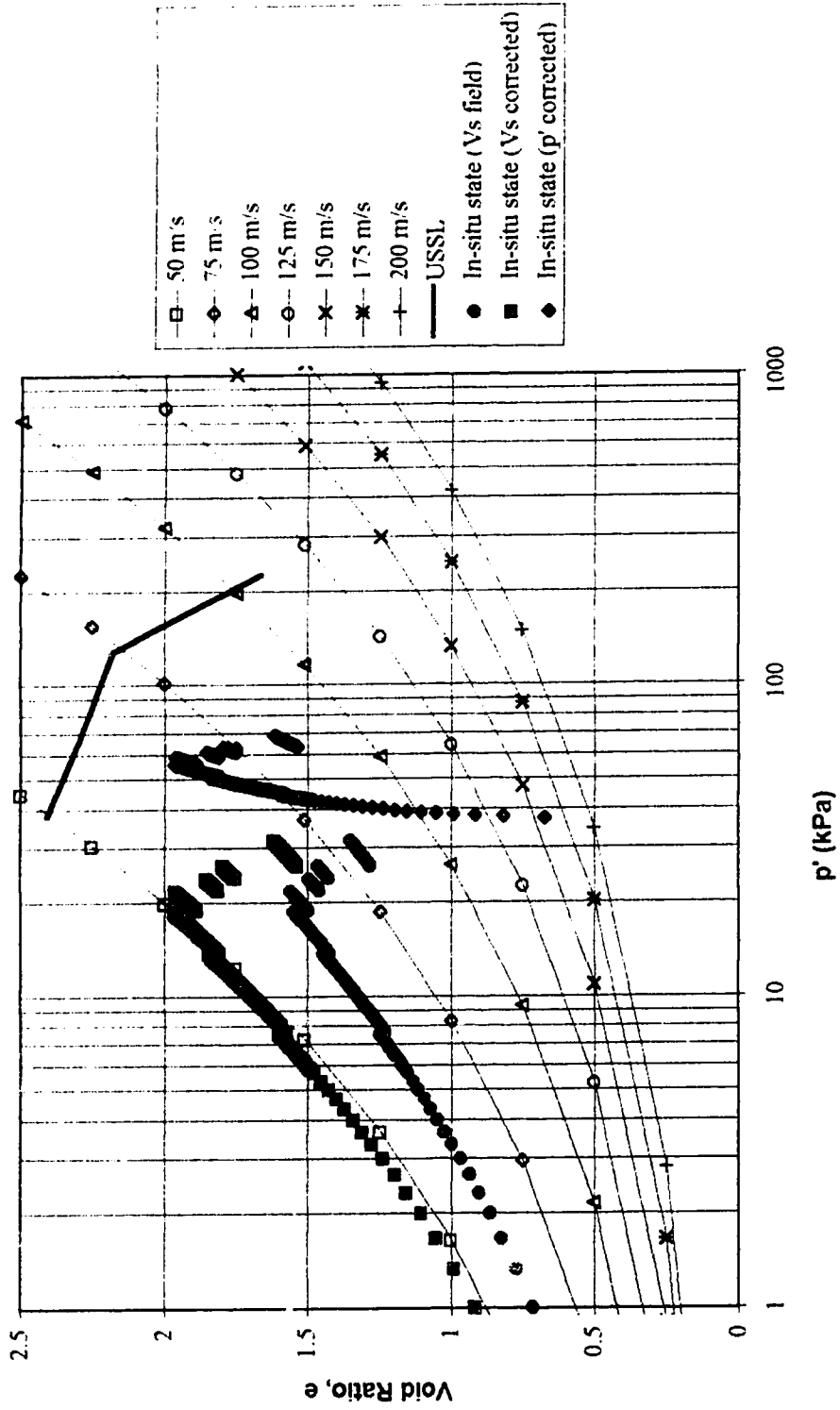


Figure 7.8: Prediction of in-situ state based on estimated in-situ stresses for $K_0 = 1.0$ and field measured shear wave velocities for the assumption of no crust.

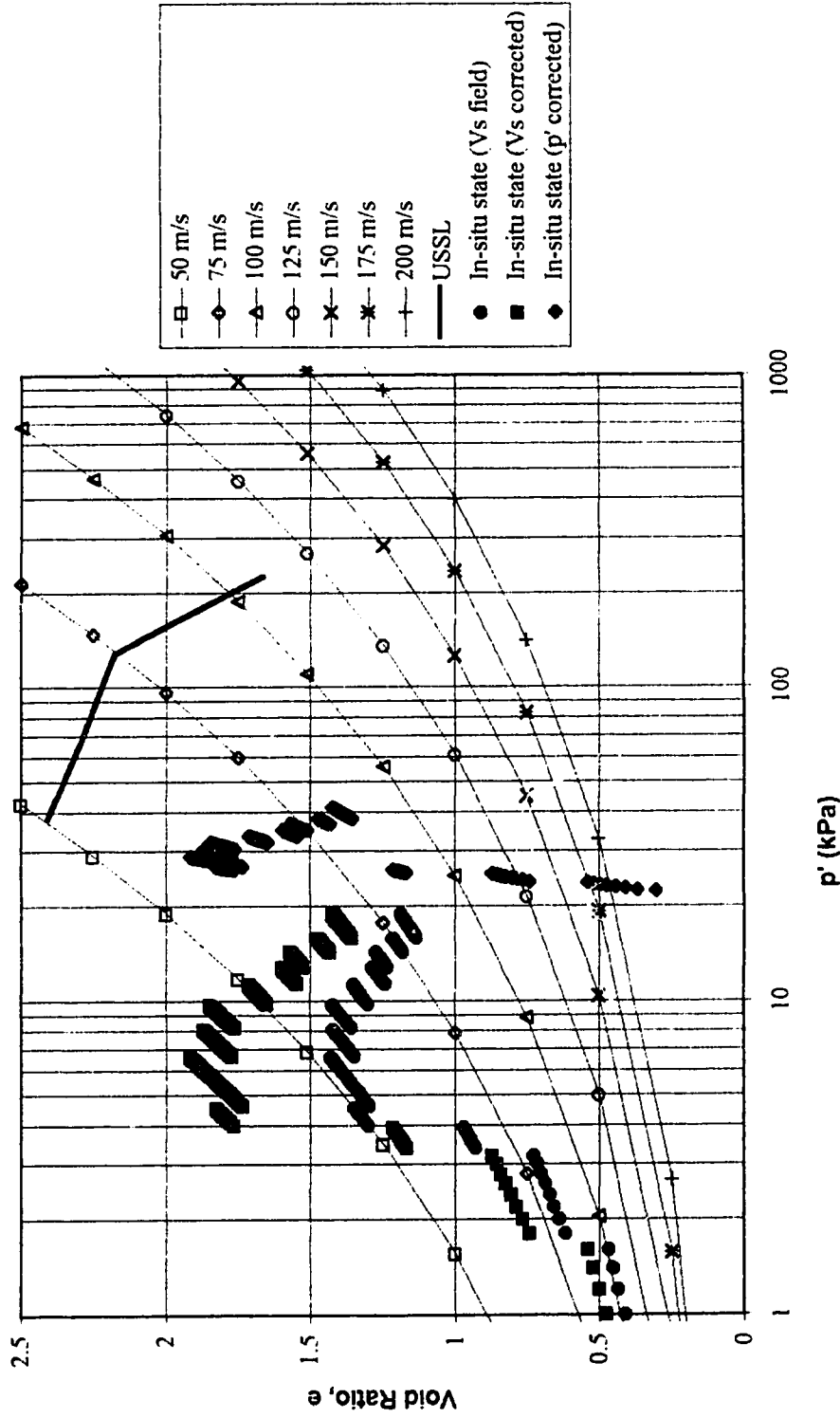


Figure 7.9: Prediction of in-situ state based on estimated in-situ stresses for $K_0 = 0.4$ and field measured shear wave velocities for the assumption of a stiff crust.

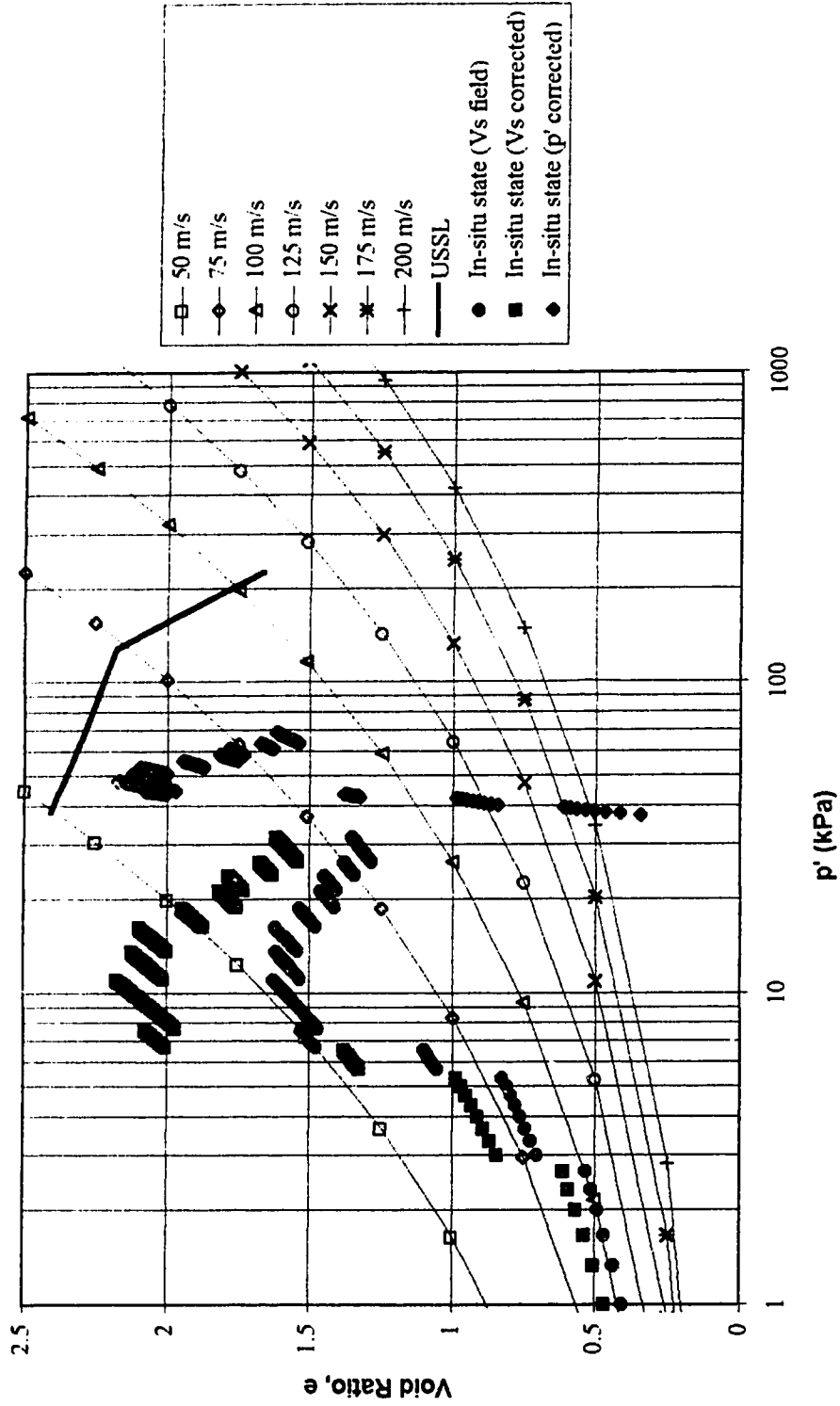


Figure 7.10: Prediction of in-situ state based on estimated in-situ stresses for $K_0 = 1.0$ and field measured shear wave velocities for the assumption of a stiff crust.

8. Summary and Conclusions

A slope failure occurred in cell 3 of the 1977 coal ash lagoon at the Wabamun generating station. Based on eye-witness accounts of the event, it appears that the failure was a liquefaction flow slide. The failure appears to have been triggered by toe erosion of the cell dike which resulted in a sudden loss of strength of the ash material beneath the dike. This research attributed this sudden loss of strength to a liquefaction induced mechanism, and has attempted to explain the event using a liquefaction analysis procedure suggested by Cunning (1994).

Basic in-situ testing was carried out in the ash deposits adjacent to the slide area in an effort to characterize the material. This characterization has indicated that the ash is a very weak granular material with a high compressibility, and that the material may be weakly cemented.

Laboratory testing was carried out on freshly deposited reconstituted samples of the Wabamun ash sand in an effort to define state boundaries and the relationship between shear wave velocity, void ratio and effective confining stress. This laboratory testing has confirmed that the material is highly compressible, and that the material undergoes crushing at confining stresses as low as 80 kPa.

When the results of the laboratory testing are combined with the in-situ test results using the method described by Cunning (1994), the in-situ response of the material is predicted to be strain hardening. This predicted response is not consistent with the mechanism attributed with the failure, and leads to two possible conclusions. Either the prediction of in-situ soil response is incorrect, or the mechanism attributed to the failure is incorrect.

The prediction of in-situ soil response was based primarily on the laboratory test results on freshly deposited reconstituted samples. The CPT results show a response of the material in-situ to be similar to that observed in lightly cemented carbonate sands,

where measured sleeve friction is very low. Other experience given in the literature with lightly cemented carbonate sands indicates that even small degrees of cementation can result in the material becoming very brittle and strain softening. This indicates there is a need for further work to study the possibility of cementation in the Wabamun ash deposits. It further indicates that conventional sampling and testing methods could be responsible for non-conservative error in the estimation of material behavior when applied to a deposit of aged, cemented and structured soil. For deposits such as the Wabamun sand, methods of undisturbed sampling are necessary to preserve structure for testing in the laboratory.

There does exist the possibility that the failure was not initiated by a strain softening flow liquefaction failure. The overtopping of the dike and subsequent toe erosion described by eye-witnesses, combined with a high head of water behind the dike could have resulted in piping beneath the dike leading to eventual failure. However, the post-failure geometry and eyewitness descriptions suggest a sudden and rapid failure resulting in large lateral movement of essentially rigid sections of dike. This evidence strongly supports a strain softening flow liquefaction mechanism.

This research has provided a preliminary insight into the 1994 failure in cell 3 and has identified some important issues regarding the characterization of these materials. Clearly there is a need for continued research in this area.

9. Suggestions for Further Research

It can be concluded that the field and laboratory testing conducted for this research is not sufficient to quantify the complex behavior of the Wabamun sand and accurately predict the liquefaction failure of cell 3. In particular, in-situ density, as well as the effects of aging and cementation on shear wave velocity and material brittleness need to be further investigated.

Estimation of in-situ density is of great importance in the interpretation of data, the preparation of normalized cone bearing against normalized friction ratio and normalized cone bearing against normalized small strain shear modulus, and the estimation of void ratio from the e - p' - V_s relationship. For the analysis conducted here, in-situ density was estimated based on laboratory measured index properties. As these index properties were measured using disturbed samples, they cannot be considered representative of the water deposited, aged and cemented material as it exists in-situ. Given the importance of in-situ density to the data analysis, a program of in-situ undisturbed sampling using a method such as block sampling or ground freezing (Sego et al., 1994) should be undertaken. This would allow for accurate estimation of in-situ density and for the determination of the variation of in-situ density with depth.

To further enhance the accuracy of classifications using plots of normalized cone bearing against normalized friction ratio and normalized cone bearing against normalized small strain shear modulus, and the estimation of void ratio from the e - p' - V_s relationship, the use of seismic CPT (SCPT) is recommended. While SASW techniques require forward modeling of data based on estimated values of bulk density and Poisson's ratio, SCPT gives a direct measure of V_s . This reduces the number of times the estimated value of bulk density enters into calculations, and provides a better coupling between measurements of Q_p , F_r and V_s , since all are measured at the same time.

The presence of even light cementation in-situ could greatly affect the application of the laboratory e - p' - V_s relationships based on laboratory testing of unaged, reconstituted samples to field conditions. Based on experience with pile driving in carbonate sands

(Murff, 1987), the very low sleeve friction observed in the CPT data suggests the Wabamun sand is compressible and cemented. However, classification based on Q_t and G_o/q_t plot the majority of the material as young and uncemented. In order to understand this effect, we need to better understand the role of cementation in the behavior of the material in-situ. A program of laboratory testing on in-situ frozen, undisturbed samples should be undertaken. Oedometer tests should be conducted to determine the degree of overconsolidation (if any) resulting from cementation. Since we know the deposit to be normally consolidated with respect to its stress history, any overconsolidation that is seen could be attributed to cementation. A program of triaxial testing should also be conducted to determine the in-situ USSL and $e-p'-V_s$ relationship. If the material did prove to be cemented in-situ, we could expect to see significant differences between the behavior of intact and reconstituted samples.

In order to further understand the relationship between age, cementation and shear wave velocity, a program of aging tests should be carried out on Wabamun sand and on a non-cementing sand. By measuring shear wave velocity of a laboratory reconstituted sample as it ages, the initial portion of the Robertson et al. (1995) relationship between shear wave velocity and age (figure 3.10) could be determined. By comparing the response of Wabamun sand to that of a silica sand similar to those used in determining the relationship in figure 3.10, the applicability of this relationship to Wabamun sand could be determined. It can be expected that if Wabamun sand is cemented, the relationship between V_s and age for it would be steeper than that for silica sands, and greater corrections would need to be applied to laboratory measured data for tests on unaged samples.

Bibliography

- Addo, K. O. 1991. Shear wave velocity measurements using Rayleigh surface waves. 44th Canadian Geotechnical Conference, Calgary, AB., Sept. 29-Oct. 2, 1991. pp. 11.1-11.10.
- Airey, D. W., Randolph, M. F. and Hyden, A. M. 1988. The strength and stiffness of two calcareous sediments. Proceedings, International Conference on Calcareous Sediments, Perth, Australia, Vol. 2, pp. 807-835
- Campanella, R. G. and Robertson, P. K. 1981. Applied cone research. Symposium on Cone Penetration Testing and Experience, Geotechnical Engineering Division, ASCE, Oct. 1981, pp. 343-362
- Chillarige, A. V. 1995. Liquefaction and seabed instability in the Fraser River delta. Ph.D. thesis, University of Alberta, Edmonton, Alberta.
- Chillarige, A. V., Morgenstern, N. R., Robertson, P. K. and Christian, H. 1995. Characterization of Fraser River delta sand. Ph.D. thesis, University of Alberta, Edmonton, Alberta. Submitted to the Canadian Geotechnical Conference, 1995.
- Coop, M. R. 1990. The mechanics of uncemented carbonate sands. *Geotechnique* **40**(4): 607-626.
- Cunning, J.C. 1994. Shear wave velocity measurement of cohesionless soil for the evaluation of in-situ state. M.Sc. thesis, University of Alberta, Edmonton, Alberta.
- Demars, K. R. 1982. Unique engineering properties and compression behavior of deep-sea calcareous sediments. STP 777, ASTM, pp. 97-112.
- Geotechnical Department of Helsinki. 1983. **The Utilization of Coal Ash in Earth Works: Technical Guidelines**. The Geotechnical Department of Helsinki, Helsinki, Finland. 35pp.
- Gillespie, D. 1988. Ph.D. thesis, University of British Columbia, Vancouver, British Columbia
- Ishihara, K. 1993. Liquefaction and flow failure during earthquakes. *Geotechnique*, **43**(3): 349-415.
- Joshi, R. C., and Rosauer, E. A. 1973. Pozzolanic activity in synthetic ashes. *American Ceramic Society Bulletin* **52**(5): 456-463
- Joshi, R. C. 1981. Engineering aspects of coal ash production, disposal and utilization. Proceedings, Workshop on Coal Ash and Reclamation, Alberta Land

Conservation and Reclamation Council, Edmonton, Alberta, April 29 and 30, 1981

- Joshi, R. C., and Marsh, B. K. 1987. Some physical, chemical and mineralogical properties of some canadian fly ashes. *Materials Research society Proceedings* **86**: 113-126.
- Lee, L. L. and Seed, H. B. 1967. Drained strength characteristics of sands. *ASCE Journal of Soil Mechanics and Foundation Engineering Division*, **93**(SM6): 117-141.
- Leroueil, S. 1992. A framework for the mechanical behavior of structured soils, from soft clays to weak rocks. *Proceedings, U.S. - Brasil NSF Geotechnical Workshop on Applicability of Classical Soil Mechancs Principles to Structured Soils*. 23-25 November, 1992, pp. 107-128.
- Maude, C. W., Kirchner, A. T., Daniel, M. and Montfort, O. 1994. **World Coal-Fired Power Stations. North and South America**. IEA Coal Research. London. 165pp.
- Miura, N., Murate, H. and Yasafuku, N. 1984. stress-strain characteristics of sand in a particle-crushing region. *Soils and Foundations* **24**(1): 77-89.
- Murff, J. D. 1987. Pile capacity in calcareous sands: state-of-the-art. *ASCE Journal of Geotechnical Engineering*, **113**(5): 490-507.
- Pestana, J. M. and Whittle, A. J. 1995. Compression model for cohesionless soils.
- Roberts, J. E. and DeSouza, J. M. 1958. The compressibility of sands. *Proceedings, ASTM*, **58**: 1269-1277.
- Robertson, P.K. 1970. Soil classification using the cone penetration test. *Canadian Geotechnical Journal* **27**: 151-158.
- Robertson, P.K., Woeller, D. J. and Finn, W. D. L. 1992. Seismic cone penetration test for evaluating liquefaction potential under cyclic loading. *Canadian Geotechnical Journal*, **29**: 686-695.
- Robertson, P. K. 1994. Suggested terminology for liquefaction: An internal CANLEX report. University of Alberta, Edmonton, Alberta.
- Robertson, P. K., Fear, C. E., and Woeller, D. J. 1995. Estimation of sand compressibility from seismic cone penetration test. Submitted to the Canadian Geotechnical Conference, 1995.
- Sasitheran, S. 1994. Collapse behavior of a very loose sand. Ph. D. thesis, University of Alberta, Edmonton, Alberta.

- Schmertmann, J. H. 1991. The mechanical aging of soils. *ASCE Journal of Geotechnical Engineering*, **117(9)**: 1288-1330.
- Semple, R. M. 1988. The mechanical properties of carbonate soils. *Proceedings, International Conference on Calcareous Sediments, Perth, Australia, Vol. 2*, pp. 807-835.
- Skirrow, R. 1995. Normalized shear wave velocity vs. void ratio for various sands. Unpublished thesis material. M.Sc. candidate, University of Alberta, Edmonton, Alberta.
- Sladen, J. A. and Oswell, J. M. 1989. The behavior of very loose sand in the triaxial compression test. *Canadian Geotechnical Journal*, **26**: 103-113.
- Stahl, R. P. 1995a. Microsoft Excel spreadsheet. Ph.D. candidate, University of Alberta, Edmonton, Alberta.
- Stahl, R. P. 1995b. Spectral Analysis of surface waves. Unpublished thesis material. Ph.D. candidate, University of Alberta, Edmonton, Alberta.
- Terzaghi, K. and Peck, R. B. 1948. **Soil Mechanics in Engineering Practice**. John Wiley and Sons, Inc., New York. 609pp.
- Tripodi, R. A., and Cheremisinoff, P. N. 1980. **Coal Ash Disposal: Solid Waste Impacts** Technomic Publishing Company, Inc., Westport, CT. 52pp.
- Vaid, Y. P. and Negussey, D. 1984. A critical assessment of membrane penetration in the triaxial test. *Geotechnical Testing Journal*, **7(2)**: 70-76.
- Vesic, A. S. and Clough, G. W. 1968. Behavior of granular materials under high stresses. *ASCE Journal of Soil Mechanics and Foundation Engineering Division*, **94(SM3)**: 661-688.
- Zhu, F., Clark, J. I. and Paulin, M. J. 1995. Factors affecting at-rest lateral stress in artificially cemented sands. *Canadian Geotechnical Journal*, **32**: 195-203

Appendix A

Preparation of Reconstituted Sand Samples

All of the triaxial test samples for this research were prepared in the lab using the technique of moist tamping. This technique allows for the preparation of sand samples that are both uniform in consistency (Sasitharan, 1994 and Pitman, 1993) and in a very loose state.

Preparation of the sample begins with the assemble of the triaxial cell, complete with porous stones, load head and a 127 mm reference sample. This allows for a reference height to be determined using a dial gauge mounted on a ring stand. This reference height is recorded and used later to determine the actual sample height.

The triaxial cell is then disassembled, a porous stone placed on the base using Teflon tape, and the membrane placed on the base using O-rings. A 63.6 mm diameter split mold is then placed around the membrane. The top of the membrane is stretched over the top of the split mold, and vacuum applied to the split mold to hold the membrane open.

To prepare the sand sample, a known mass of dry sand is mixed with a known amount of water to achieve a desired moisture, usually between 2.5% and 10%. While 5% was used in tests on Ottawa and Syncrude sands by Cuning (1994), Sasitharan (1994) and Pitman(1993), the high fines content and high porosity of the Wabamun sand required a moisture content of 10%. This moisture content was sufficient to give the cohesionless soil an apparent cohesion, allowing for the preparation of extremely loose samples.

Once the sand had been thoroughly mixed to the desired water content, it is placed in 4 layers into the membrane. Each layer is compacted with a drop hammer weighing 148 grams falling a distance of 4 mm. Five blows were used for the initial layer, increasing to 14 blows for the last layer. This ensured uniform compactive effort throughout the sample. Cuning (1994) suggested the use of a drop height of up to 21 mm and up to 15 blows on the first layer increasing to 25 blows on the final layer. This

proved to create samples in the Wabamun sand that were too dense and therefore on the dilative side of the USSL.

After the top layer is placed and leveled, the top loading head with the bender element, porous stone and load cell is added. The top of the membrane is then removed from the split mold and fixed to the loading head with O-rings. The vacuum is then switched from the split mold to the top and bottom drainage ports of the sample to create an effective stress in the sample and prevent collapse upon removal of the split mold. Vacuum pressure used in the preparation was 15 kPa.

The split mold is then removed and measurements of the sample diameter taken. Nine diameter measurements, three each at the top, middle and bottom of the sample, were used to determine the average diameter.

Work by Cunning (1994) suggested the use of girth belts and a second membrane in the preparation of the sample. For this work, the ratio of axial strain to volumetric strain was taken as 3:1, as given by a simple elastic solution. This eliminated the need for girth belts. The use of a second membrane was considered. However early tests conducted using a single membrane proved this unnecessary.

The cell body is assembled and the top cap placed on the loading ram, taking care not to strain the sample. The initial sample height was determined using the reference height measured earlier. Sample height is given as the reference sample height of 127 mm plus or minus the changes in reference dial gauge readings. An LVDT is added at this time and zeroed in order to track changes in height. In this way, the zero value on the LVDT corresponds to the initial height of the sample, and all subsequent changes, either due to handling of the cell, saturation or consolidation can be accounted for.

The cell is then transferred into the loading frame, the cell filled with water, and the cell and back pressure lines attached. The cell pressure transducer is zeroed to atmospheric pressure and a cell pressure of 25 kPa applied at the same time the vacuum is removed. The pore pressure transducer in the base and the load cell in the loading head are also connected to the data acquisition system at this time, and the pore pressure transducer zeroed to atmospheric pressure. Also at this time, the volume change measurement device is zeroed. The sample is then prepared and ready for saturation.

Back Pressure Saturation and B-test

Back pressure saturation is used to bring the samples to approximately 100% saturation at a 25 kPa consolidation state. The procedure used to achieve this is as follows.

In order to bring the sample to near saturated conditions, de-aired water is flushed through the sample from the bottom drainage, up through the sample and out the top drainage. After ensuring saturation of the back pressure lines, approximately 5 litres of water are passed through the sample at a low gradient before proceeding with back pressure saturation. Low gradient is defined here as one which is sufficiently small that it does not cause collapse of the sample due to pore pressures created by the flow.

Back pressure saturation consisted of bringing the cell and back pressure from 25 kPa and 0 kPa respectively to 325 kPa and 300 kPa respectively in increments of 100 kPa. Dead weights were applied to the top loading platen at each increment to compensate for the unequal end area effect of the internal load cell arrangement while allowing for free movement of the loading platen. In each increment, the sample is allowed to equilibrate under the new back pressure conditions, as shown by the measurement of no further water entering the sample. The sample is then brought up to a cell pressure of 425 kPa and a back pressure of 400 kPa in increments of 25 kPa with Skempton's B test conducted for each increment. This test is done by monitoring the response in pore pressure under undrained conditions to an increase in cell pressure. The B value is the ratio of pore pressure response to cell pressure change, and should be 1.0 in a fully saturated sample. After measuring the pore pressure response, the stage is completed by equalizing the pore pressure to the back pressure at 25 kPa less than the cell pressure. This procedure consistently resulted in a sample that is saturated. That is, samples would either show a B value of greater than 0.95, or consecutive B values that were equal.

Consolidation and Shear Wave Velocity Measurement

Shear wave velocity measurements were taken at the initial consolidation state, then at increments of consolidation of 25, 50 or 100 kPa up to the desired consolidation stress. Again dead weights were applied as necessary to compensate for pressure changes.

Consolidation usually took about 20 minutes to complete, as shown by the monitoring of volume change in the sample. However, for consistency, each consolidation increment is allowed to run for 30 minutes.

Void Ratio Calculations

The Void ratio for the sample is calculated from the following equation from Cuning (1994):

$$e = \frac{G_s * (V_{init} - \Delta V_{sat} - \Delta V_{consol.} - \Delta V_{mem.corr.}) * \rho_w}{M_s} - 1$$

where:

G_s	=	Specific gravity of the solids
M_s	=	The mass of the solids, g
ρ_w	=	The density of water, 1 g/cm ³
V_{init}	=	The volume after sample preparation, cm ³
ΔV_{sat}	=	The calculated volume change during saturation, cm ³
$\Delta V_{consol.}$	=	The measured volume change during consolidation, cm ³
$\Delta V_{mem.corr.}$	=	The change in volume during membrane penetration, cm ³

The change in volume during membrane penetration is included in the equation for completeness. However, according to Vaid and Negussy (1984), Wabamun sand is sufficiently fine that it does not require this correction.

Shear Loading

At the completion of consolidation, the loading ram is brought into direct contact with the load frame and the sample is sheared either drained or undrained under a constant strain rate of 0.15 mm/minute. The sample is strained to approximately 20% axial strain, with all instruments being monitored by a CEED signal conditioner, and data stored on a Pro-Spec IBM compatible 286 computer every 16 seconds.

The undrained tests were considered complete when the values of axial load and pore pressure reached constant or near constant values, or the sample had reached its USS. This usually occurred by the time the sample had been strained 20%. The drained tests were considered complete when the axial load and volume change reached constant or near constant values, or USS. This took greater axial strains, usually about 25%. The shear wave velocity of the sample is taken at this point and the stress conditions recorded.